

**Search for Time-dependent Fluctuations in
Cosmic Ray Flux with the AMS-01 Detector**

and

Construction of the AMS-02 Detector

THÈSE

présentée à la Faculté des sciences de l'Université de Genève
pour obtenir le grade de Docteur ès sciences, mention physique

par

Mercedes PANICCIA

d'Italie

Thèse N° 3963



**UNIVERSITÉ
DE GENÈVE**

FACULTÉ DES SCIENCES

**Doctorat ès sciences
mention physique**

Thèse de *Madame Mercedes PANICCIA*

intitulée :

**"Search for Time-Dependent Fluctuations in Cosmic Ray Flux
with the AMS-01 Detector
and
Construction of the AMS-02 Detector"**

La Faculté des sciences, sur le préavis de Messieurs M. POHL, professeur ordinaire et directeur de thèse (Département de physique nucléaire et corpusculaire), A. G. CLARK, professeur ordinaire (Département de physique nucléaire et corpusculaire), E. O. FLÜCKIGER, professeur (Universität Bern, Physikalisches Institut, Bern) et de Madame S. GENTILE, professeure (Università degli Studi di Roma « La Sapienza », Dipartimento di fisica, Roma, Italia), autorise l'impression de la présente thèse, sans exprimer d'opinion sur les propositions qui y sont énoncées.

Genève, le 2 avril 2008

Thèse - 3963 -


Le Doyen, Jean-Marc TRISCONE

N.B.- La thèse doit porter la déclaration précédente et remplir les conditions énumérées dans les "Informations relatives aux thèses de doctorat à l'Université de Genève".

Nombre d'exemplaires à livrer par colis séparé à la Faculté : - 7 -

Contents

Résumé	v
Acknowledgments	vii
Introduction	ix
1 Cosmic rays near Earth	1
1.1 Composition and spectra	2
1.2 Sources, acceleration and propagation	6
1.3 Heliospheric and magnetospheric effects	8
1.3.1 Geomagnetic effects	9
1.3.2 Time variation and solar modulation effects	10
2 The Alpha Magnetic Spectrometer Precursor Flight	19
2.1 The AMS-01 detector	19
2.1.1 The Magnet	20
2.1.2 The Silicon Tracker	22
2.1.3 The Time Of Flight hodoscopes	26
2.1.4 The Aerogel Cerenkov Counter	27
2.2 AMS-01 Operations	28
2.2.1 Flight Parameters	28
2.2.2 Trigger and Livetime	30
2.3 Event Reconstruction	32
2.3.1 Velocity Reconstruction	32
2.3.2 Track Reconstruction	32
2.3.3 Charge Reconstruction	33
3 Data analysis	37
3.1 Event selection	37
3.1.1 MonteCarlo samples	37
3.1.2 Selection criteria	38
3.2 Electron, Proton and He nuclei flux measurements	42
3.2.1 Acceptance estimation	43
3.2.2 Background estimation	49

3.2.3	Spectra	52
3.3	Search for rapid cosmic-ray flux variations	73
3.3.1	Mean counting rate measurement	73
3.3.2	Actual counting rate measurement	74
3.3.3	Flux fluctuation occurrences	78
3.3.4	Comparison to the geomagnetic activity of 8-12 June 1998	82
4	Construction of the AMS-02 detector	89
4.1	The AMS-02 Magnet	90
4.2	The AMS-02 Silicon Tracker	93
4.3	The AMS-02 Counter System	102
4.4	The Transition Radiation Detector	104
4.5	The Electromagnetic calorimeter	106
4.6	The Ring Imaging Cerenkov detector	109
5	Conclusions	113
A	Catalog of cosmic-ray flux fluctuation events	115
A.1	Electron flux fluctuation occurrences	115
A.2	Proton flux fluctuation occurrences	116
A.3	He nuclei flux fluctuation occurrences	124
B	AMS Flight Chronology	127
B.0.1	Attitude parameters from June 8 to June 12	129
C	Solar activity in June 1998	133
	Bibliography	145

Résumé

La découverte au début du vingtième siècle de l'existence d'un flux de particules énergétiques provenant de l'espace a engendré un vif intérêt auprès de la communauté scientifique de l'époque, donnant naissance à de nouvelles branches d'étude, dont la physique des particules est l'exemple le plus éclatant.

La formulation d'un modèle pouvant expliquer l'origine et le spectre du rayonnement cosmique et aussi décrire les mécanismes de propagation et d'accélération dans l'espace interstellaire et interplanétaire, a nécessité l'effort conjoint de différents domaines: la physique des particules, la physique des plasmas, l'astrophysique, la physique solaire et la géophysique.

L'analyse de l'énorme quantité de données collectées au sujet de rayons cosmiques au moyen de détecteurs au sol, en ballon et dans l'espace, combinée avec les observations des événements astrophysiques, solaires et géophysiques, a permis d'expliquer la plupart des propriétés des rayons cosmiques observés. Pourtant le modèle n'est pas complet et les études continuent toujours.

Dans ce cadre s'insère l'expérience AMS, un détecteur destiné à la mesure systématique et à long terme de la composition et du flux des rayons cosmiques dans une orbite proche de la Terre. Ces mesures fourniront des informations cruciales à la compréhension de l'origine des rayons cosmiques et des mécanismes qui sont à la base des processus d'emprisonnement dans la galaxie et de propagation dans les milieux interstellaire et interplanétaire.

En Juin 1998 un détecteur prototype, AMS-01, a effectué un vol de dix jours à bord de la Navette Spatiale *Discovery*, au cours de la mission STS-91. Le détecteur AMS-01 a été construit sur la base des techniques de détection développées pour les expériences auprès des accélérateurs. L'expérience de 1998 a permis de valider l'utilisation de ces techniques dans l'environnement spatial. De plus, les données recueillies ont apporté des mesures précises des spectres des rayons cosmiques chargés dans l'intervalle d'énergie allant de 100 MeV per nucleon à 200 GeV per nucleon, et ont permis d'établir la meilleure limite, à l'époque, sur l'existence de l'antimatière.

Le détecteur final, AMS-02, actuellement en phase d'intégration, sera prochainement installé sur la Station Spatiale Internationale pour une prise de données de trois ans. Avec des performances améliorées par rapport au détecteur prototype, AMS-02 fournira des mesures plus précises des spectres des rayons cosmiques chargés et neutres pour des énergies allant jusqu'au TeV.

Le travail de recherche présenté dans la première partie de cette thèse s'adresse à l'étude des variations temporelles du flux des rayons cosmiques en utilisant les données du détecteur AMS-01. Etant donné la courte durée du vol d'AMS-01, l'étude concerne plus spécialement des fluctuations rapides des rayons cosmiques, sur une échelle de temps allant des minutes aux heures. Après avoir identifié une méthode de sélection des variations temporelles systématiques du flux des rayons cosmiques et avoir rédigé un catalogue des fluctuations observées, l'analyse est complétée par l'étude de la corrélation entre la fréquence des fluctuations et le niveau de perturbation du champ magnétique terrestre due à l'activité solaire.

En effet l'éjection de plasma du Soleil peut affecter le flux des particules près de la Terre jusqu'aux énergies de 50 GeV per nucleon dans le cas des événements les plus violents. Dans les dernières décennies, ces phénomènes ont suscité un grand intérêt parce que les augmentations soudaines du flux de particules énergétiques près de la Terre peuvent perturber le fonctionnement des satellites, affectant les communications et provoquant même des perturbations dans la distribution du courant électrique sur Terre.

La deuxième partie de cette thèse décrit le détecteur AMS-02, en faisant le point sur l'état de sa construction. En particulier y sont décrites les activités de production et d'intégration du détecteur de traces au silicium, qui ont eu lieu à l'Université de Genève et qui se sont terminées en Automne 2007 avec le transport du détecteur de traces dans la salle d'assemblage d'AMS-02 au CERN. Une fois l'assemblage et les tests effectués, le détecteur AMS-02 sera transporté aux États-Unis au Centre Spatiale *Kennedy* de la NASA en attente d'être installé sur la Station Spatiale Internationale à l'occasion d'une des dernières missions de la Navette Spatiale, fin 2009 ou début 2010.

Acknowledgments

This writing marks the conclusion of my five-year PhD studentship at the *Département de Physique Nucléaire et Corpusculaire* of *Université de Genève* within the AMS group. I would like to express my gratitude to all those who have been part of this experience.

First of all I would like to warmly thank my advisor, Prof. Martin Pohl, for his valuable guidance in the realization of this thesis and for the confidence he has constantly shown in my work.

I'm extremely grateful to Dr. Vitaly Choutko (MIT), member of the AMS Collaboration, whose help has been crucial for this work.

A special thank goes to Prof. Catherine Leluc for her kind support and for her endless patience in revising my french writings.

I would like to thank the members of my thesis committee, Prof. Simonetta Gentile, Prof. Erwin Flueckiger and Prof. Allan Clark, for having so carefully read my writing and for their comments, which have been so helpful to the refinement of the thesis paper.

Many thanks to the members of the AMS Geneva group I have met in these five years period: Prof. Maurice Bourquin, Prof. Divic Rapin, Dr. Daniel Haas and Prof. Catherine Leluc for their comments in the becoming of this work; Dr. Philipp Azzarello, Dr. Sonia Natale, Manfred Willenbrock and Philippe Bouvier for having introduced me to the delicate art of of silicon detectors handling and for the friendly atmosphere they managed to create in the not-so-comfortable environment of the cleanrooms.

I would like to thank also the engineering and technical staff of the Geneva University, in particular Pierre Bené, Eric Perrin, Florian Masciocchi and Yann Meunier for their kind collaboration and their precious support.

I'm very grateful to Mme Peggy Argentin and Mme Catherine Blanchard for their dedication and kindness in helping with the administrative tasks.

Last but not least, I would like to thank all the colleagues with whom I have shared not only the working and studying hours but also the relaxing breaks: Philipp, Sonia, Bertrand, Olivier, Till, Filipe and Estela for the friendship they have offered to me; and those who have become in these years my dearest friends: Sofia and Joao, whose friendship comes from earlier times, Silvio, with whom I had the pleasure to share the office in the last months of my staying at the DPNC, and Chiara and Mauro, to whom I want to address a special thought for having been so

close to me in the hardest times.

Introduction

Since their discovery at the beginning of the twentieth century, cosmic rays have been of great interest to physicists. The formulation of a model describing their origin, composition and the acceleration and propagation mechanisms in the interstellar and interplanetary media, have implied the joint effort of many disciplines: particle physics, plasma physics, astrophysics, solar physics and geophysics.

The huge amount of cosmic ray data, gathered with ground-based, balloon and space-borne detectors, have been matched with astrophysical, solar and geophysical data, allowing to explain most of the observed cosmic ray properties. Yet the picture is not complete and further observations and studies are still going on.

Indeed one of the physics goals of the AMS experiment is the systematic, long term measurement of cosmic ray composition and flux in a near Earth orbit, which will provide crucial informations on cosmic ray origin, their confinement in the galaxy and their propagation mechanism.

The AMS project has started in the 1990s when a prototype detector, AMS-01, was built on the basis of detection techniques developed for accelerator detectors. The AMS-01 flight on board the Space Shuttle Discovery, during the ten-day STS-91 mission in June 1998, has mainly served to validate the use of those techniques in the space environment. Moreover, the data collected have brought precise measurements of charged cosmic ray spectra and also to set the best limit, at the time, on the existence of antimatter.

The work presented in this thesis addresses the study of cosmic ray flux variations, performed for the first time with the AMS-01 data. Given the short duration of the AMS-01 flight, more specifically the study concerns rapid cosmic ray fluctuations with time scales from minutes to hours.

Cosmic ray variations have been observed in relation to the solar activity level, which can affect particle fluxes up to energies of 50 GeV/n in the most violent phenomena. In particular, short-term fluctuations have risen a great interest in the last decades, because sudden increases of energetic particle fluxes near Earth can disturb spacecraft and satellite operations, affecting communications and even causing disruptions of electric power distribution grids on ground.

The AMS detector is sensitive to the highest energy range of solar particle events (above 100 MeV/n), and with its capability of performing simultaneous measurements of charged particle fluxes, it is able to provide important information on the composition of solar particle events.

The final AMS detector, AMS-02, which is currently in the last phase of construction, will be installed on the International Space Station for a three-year data taking, allowing even more precise measurements of charged and neutral cosmic radiation, and a more complete study of short-term cosmic ray variations, because of the extended exposure time and improved performance with respect to the AMS-01 detector.

Chapter 1

Cosmic rays near Earth

The existence of cosmic radiation continually impinging on the Earth's atmosphere was discovered at the beginning of the twentieth century. Before the advent of the accelerator technology in the 1950s, cosmic rays were the only source of high energy particles available to perform nuclear and particle physics experiments. For instance the positron, the muon and the pions were first observed in cosmic radiation. Afterwards the interest in cosmic rays shifted to the problem of understanding their origin and the propagation and acceleration mechanisms that drive them from their sources to the Earth through the astrophysical environments.

Thus cosmic ray physics involves a wide range of disciplines ranging from particle and nuclear physics to astrophysics and plasma physics. Cosmic ray physics topics presented in this chapter are taken from References [1–4].

Most likely, cosmic rays originate from highly evolved stars. After undergoing acceleration in shock wave fronts, they propagate through the interstellar medium, where secondary particles are produced by spallation of primary cosmic ray particles, and reach the Earth surroundings making their way through the interplanetary magnetized plasma.

The Earth environment is quite complex. The description of solar and geomagnetic phenomena reported in this chapter comes mainly from References [5–7].

The solar wind plasma continuously escaping from the Sun drags out the solar magnetic field lines into the interplanetary space out to the border of the heliosphere. The Earth's strong intrinsic geomagnetic field creates a cavity in the solar wind plasma, the magnetosphere, preventing most of the solar wind particles and the low energy charged cosmic particles from reaching the Earth. However, instabilities in the interplanetary magnetic field, such as those originating from transient explosive phenomena at the Sun, can create the conditions for magnetic reconnection [5] of interplanetary and geomagnetic field lines, opening a route for low energy particles towards Earth.

The Sun's activity influences the intensity of cosmic radiation near Earth in different ways. Long-term time variations in cosmic ray intensity have been observed in anticorrelation with the level of Sun activity, while short-time variations can oc-

cur in relation to Sun transient phenomena. The latter have caused great interest because of the severe impact they can have on space-borne and ground-based technological systems, leading to the development of the space weather discipline [6,7].

The conditions on the Sun, the solar wind and the interplanetary magnetic field are continuously monitored by satellites such as WIND [8], ACE [9], IMP8 [10], GOES [11], etc. Similarly Polar [12], GEOTAIL [13] and IMAGE [14] study and monitor the Earth magnetosphere. International networks of ground-based magnetic observatories [15] and neutron monitors [16] keep records respectively of the geomagnetic field and the cosmic ray intensity at the Earth's surface.

More short-time records of cosmic ray fluxes at the top of the atmosphere, collected by past and present balloon (BESS [17], JACEE [18], CREAM [19], TRACER [20]) and space-mission experiments (AMS-01 [21], PAMELA [22]), can add information on spectra and composition of solar related events. Our current understanding of the Sun-Earth connection is an outcome of comparative analysis of the data collected over the years. Nonetheless there are still open questions both on solar-terrestrial physics and in cosmic ray physics which are under investigations.

1.1 Composition and spectra

The cosmic radiation includes all stable particles and nuclei with lifetimes of order 10^6 years or longer. Cosmic ray particles are mostly protons (87%) and some He nuclei (12%) with diminishing amounts of heavier nuclei. Electrons account for about 1% of the cosmic radiation [2].

The cosmic-ray chemical composition corresponds to the elemental abundances in our solar system (Figure 1.1) with few exceptions: protons and He are under-abundant while two groups of elements (Li, Be, B and Sc, Ti, V, Cr, Mn) are over-abundant.

The relative underabundance of protons and He in the cosmic rays is not fully understood: it could either reflect the primordial composition of the cosmic ray sources or simply be due to the difference in propagation properties of the elements and the fact that the heavier elements are more easily ionised, thereby being more readily accessible for acceleration.

The overabundance of Li, Be and B is known to be due to spallation of C and O. As these elements travel through the interstellar medium, they are fragmented in collisions with the interstellar gas into lighter elements. Similarly Sc, Ti, V, Cr and Mn result from spallation of Fe.

Technically, *primary* cosmic rays are those particles accelerated at astrophysical sources, and *secondaries* are those particles produced in interaction of the primaries with the interstellar gas. Thus electrons, protons and He as well as C, O, Fe and other nuclei synthesized in stars are primaries. Nuclei such as Li, Be and B, which are not abundant end-products of stellar nucleosynthesis, are mostly secondaries.

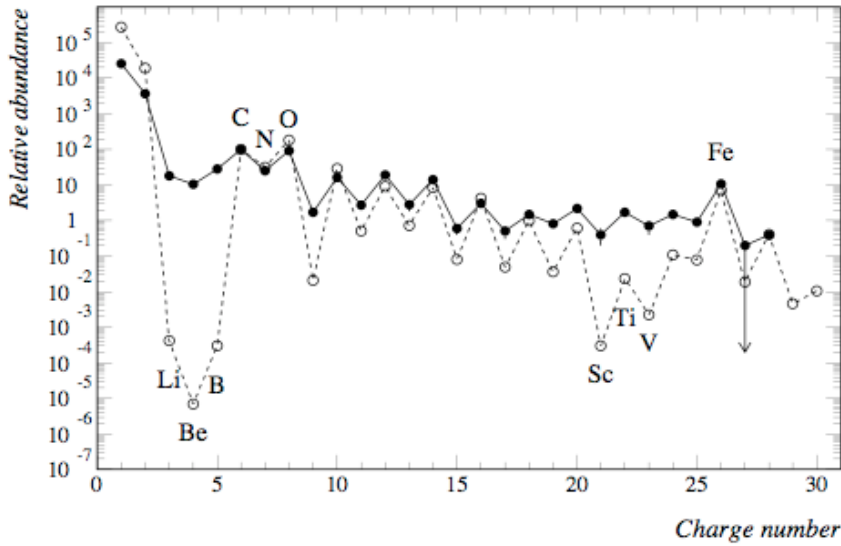


Figure 1.1: The relative abundance of cosmic rays at the top of the atmosphere (filled circles) compared with solar system and local interstellar medium abundance (open circles), all arbitrarily normalized to $C = 100$ (From Ref [23]).

The small amount of electrons and positrons in cosmic rays are thought to be of galactic origin, since energy depletion through Compton scattering with the cosmic microwave background radiation prevents their propagation over intergalactic distances. The positron fraction, $e^+/(e^+ + e^-)$, has only been measured at low energies (below 50 GeV) and found to be just a few per cent [24–28], indicating that electrons are accelerated by primary sources. If their origin had been secondary, i.e. through hadronic decays, there should be comparable fractions of electrons and positrons. Positrons, on the other hand, are likely to be produced in secondary processes, like pair production $\gamma \rightarrow e^+ + e^-$.

The ratio of antiprotons to protons is $2.9_{-0.81}^{+1.01} \times 10^{-4}$ at around 10 GeV [29], and there is clear evidence for the kinematic suppression at lower energy that is the signature of secondary antiprotons [30]. No antihelium or antideuteron has been found in the cosmic radiation. The best current measured upper limit on the ratio $\overline{\text{He}}/\text{He}$ is 6.8×10^{-7} at 95% confidence level [31]. The upper limit on the flux of antideuterons around 1 GeV/n is $1.9 \times 10^{-4} (\text{m}^2 \text{ s sr GeV/n})^{-1}$ at 95% confidence level [32].

The energy spectrum of cosmic ray protons and nuclei incident at the top of the atmosphere spans over many orders of magnitude, and above 10 GeV/n can be described by a segmented power-law formula:

$$\frac{dN}{dE} \propto E^{-\alpha} \quad (1.1)$$

with the following values [2] for the spectral index:

$$\alpha \simeq \begin{cases} 2.7 & E < 10^{16} \text{ eV} \\ 3.0 & 10^{16} \text{ eV} < E < 10^{18} \text{ eV} \end{cases}$$

For the highest energies, above 10^{19} eV, the distribution appears to be flatter.

The spectrum of electrons and positrons incident at the top of the atmosphere is steeper than the spectra of protons and nuclei.

The energy spectra of the major components of the primary cosmic radiation are shown in Figure 1.2 for energies between 2 GeV/n and $\sim 10^5$ GeV/n. Figure 1.3 shows the all-particle spectrum for energies above 10^{13} eV, multiplied by $E^{2.7}$ in order to display the features of the steep spectrum. The two breaks in the spectrum around $10^{15} - 10^{16}$ eV and 10^{19} eV are referred to as the *knee* and the *ankle* respectively.

Balloon and satellite experiments are very well suited for the study of cosmic rays at energies below the *knee* (Figure 1.2) but it is virtually impossible to gather sufficient statistics at higher energies with the relatively small detectors that may be accommodated in flown devices because of the low flux of high energy cosmic rays. However since high energy cosmic rays (HECR) interacting with the Earth's atmosphere produce extensive air-showers [2, 4], indirect measurement of HECR are feasible with arrays of ground-based detectors [33–35].

Assuming that the cosmic ray spectrum below 10^{18} eV is of galactic origin [1, 2, 4], the *knee* could reflect the fact that most cosmic accelerators in the galaxy have reached their maximum energy. Some types of expanding supernova remnants, for example, are estimated not to be able to accelerate protons above energies in the range of 10^{15} eV. Effects of propagation and confinement in the galaxy also need to be considered.

Concerning the *ankle*, one possibility is that it is the result of a higher energy population of particles overtaking a lower-energy population, for example an extragalactic flux beginning to dominate over the galactic flux [2, 4]. Alternatively it could be caused by a change in chemical composition, with lower charged nuclei dying out successively. Another possibility is that the dip structure in the region of the *ankle* is due to energy losses of extragalactic protons on the 2.7 K cosmic microwave background (CMB) radiation [1]. This dip structure has been cited as a robust signature of both the protonic and extragalactic nature of the highest energy cosmic rays [2, 4]. If this interpretation is correct, then the end of the galactic cosmic ray spectrum would be at an energy lower than 10^{18} eV, consistent with the maximum expected range of acceleration by supernova remnants.

Energy-dependence of the composition from the *knee* through the *ankle* holds the key to discriminate between these two viewpoints.

If the cosmic ray flux above the second knee (Figure 1.3) is cosmological in origin, there should be a rapid steepening of the spectrum, called the GZK¹ cut-

¹Greisen-Zatsepin-Kuzmin

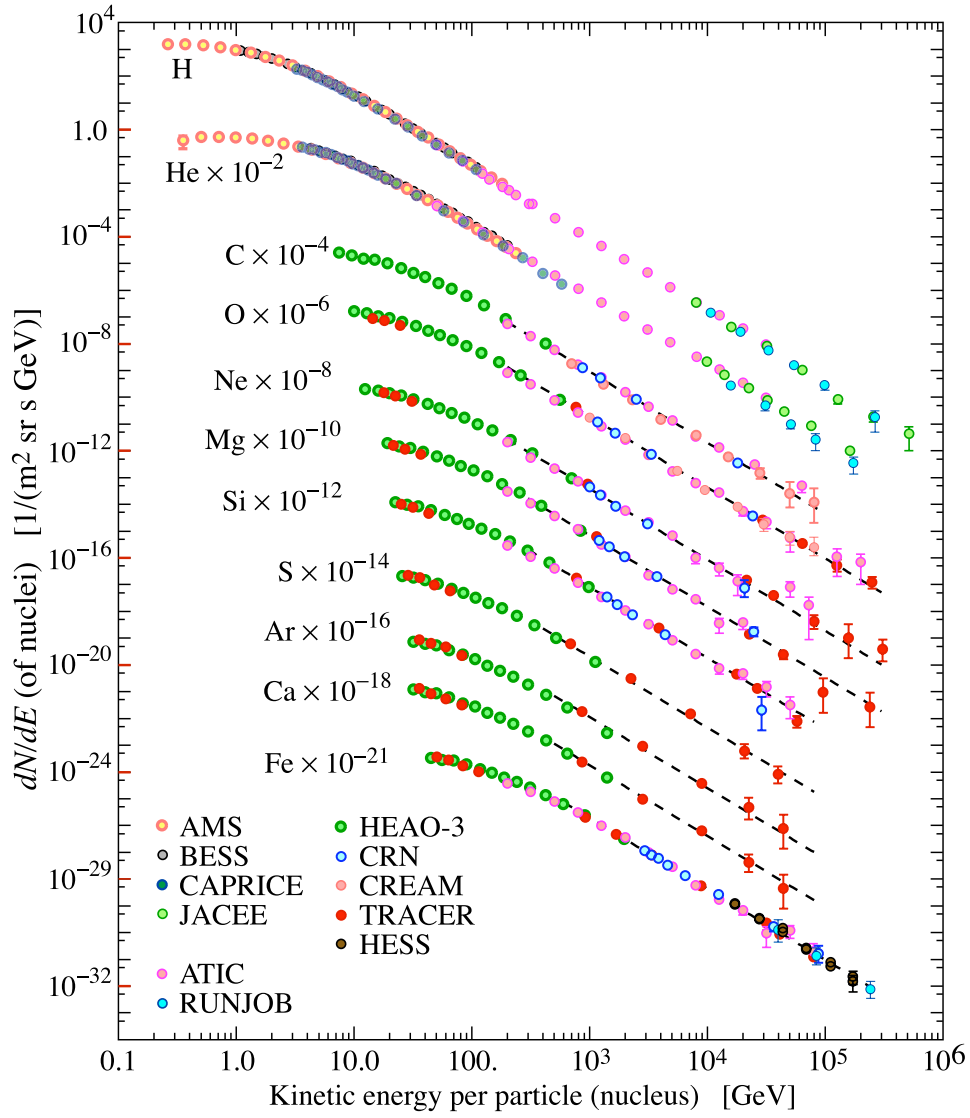


Figure 1.2: Major components of the primary cosmic radiation (From Ref. [4]).

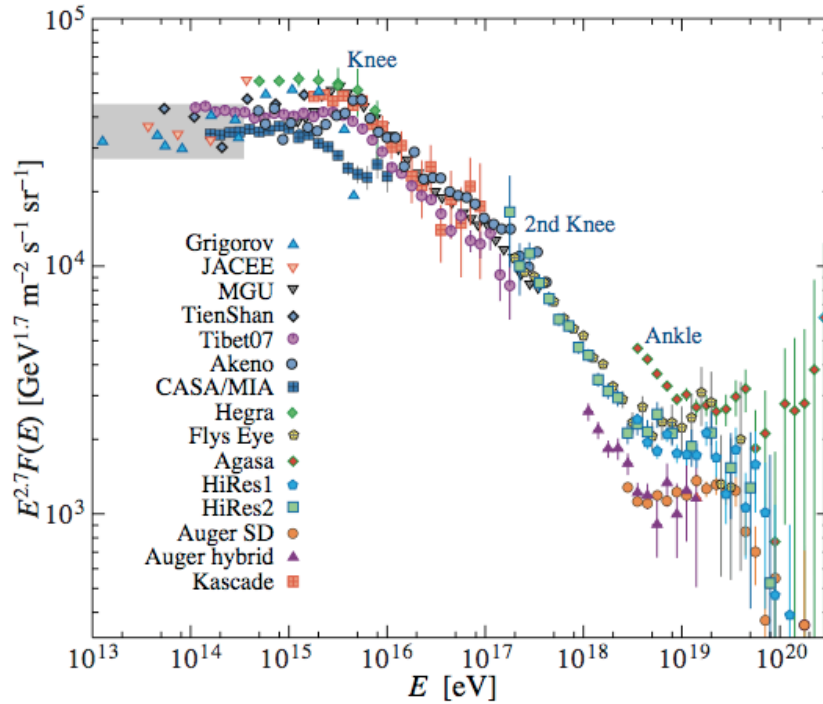


Figure 1.3: The all-particle spectrum from air-shower measurements. The shaded area shows the range of direct cosmic ray spectrum measurements (From Ref. [4])

off [36, 37], around 5×10^{19} eV, resulting from the onset of inelastic interactions of Ultra-High-Energy cosmic rays (UHECR) with the CMB.

Although all UHECR experiments have detected events of energy above 10^{20} eV [38–41], the spectral shape above the *ankle* is still not well determined. The continued power law type of flux beyond the GZK cut-off claimed by the AGASA [33] experiment is not supported by the HiRes [34] and Auger [35] experiment measurements which show a significant steepening of the cosmic ray spectrum above $3 - 5 \times 10^{19}$ eV, consistent with the onset of inelastic interactions with the CMB. Furthermore in November 2007 the Auger collaboration reported a correlation of the arrival directions of the highest energy cosmic rays with a nearby² Active Galactic Nuclei (AGN) [42].

1.2 Sources, acceleration and propagation

A major puzzle ever since the discovery of cosmic rays has been their exact origin. In modelling the origin of cosmic rays, the first conclusion, given their richness

²at distance less than 75 Mpc

in metals, is that they must come from highly evolved stars such as those that undergo supernova explosion. The detection of UHECR shows that there have to exist very powerful sites of acceleration in the Universe. In fact, it is plausible that particles with energies above the *knee* originate from outside the Milky Way, since the galactic magnetic field is not strong enough to confine them, whereas galactic sources most likely have to be found for the lower-energy part.

The most promising mechanism which may explain the existence of galactic cosmic rays up to an energy of 10^{16} eV is first-order Fermi acceleration [1] near shock-fronts caused by supernova explosions. The basic picture is a strong shock³ wave propagating through the interstellar medium which already contains some high energy particles. The medium in front of the shock and that behind the shock differ in density by a factor which depends on the equation of state. In front of the shock the particle distribution is isotropic. Some of the cosmic rays pass through the shock and are then isotropised by scattering due to irregularities behind the shock. In this process the cosmic ray gas acquires kinetic energy from the gas behind the shock. Then some of the particles recross the shock into the stationary gas. This streaming of the cosmic rays upstream is halted by the usual scattering processes so that the cosmic ray gas is again isotropised, but the particles which went through this cycle have acquired a certain amount of energy by first-order Fermi acceleration. The shock then catches up with the particles and the cycle is repeated.

This acceleration continues until energy losses balance the acceleration rate. It has been shown that this acceleration mechanism produce a power-law energy spectrum.

The shock-acceleration mechanism is expected to be active in many different types of shock other than supernova remnants, for instance at the termination shock of the solar wind and the galactic wind, at the accretion shock near a supermassive black hole (as is believed to exist at the center of an AGN) and at intergalactic shock waves.

The propagation of cosmic rays in the galaxy is determined by a diffusive process [1], where the charged particles interact with the irregularities of the galactic magnetic field.

With a galactic magnetic field of 3 to 4 μ Gauss the Larmor radius of a 1 GeV proton is of the order 10^{-6} parsec. Since the galactic disk thickness is of the order of 500 parsec the CR trajectory is connected to the galactic magnetic field.

A complete solution to the transport equation describing the propagation process requires the knowledge of the shape and size of the propagation regions of CR in the galaxy as well as the distribution of sources and of the interstellar gas density. The general approach used is to get the parameters of the theory from the observed secondary abundances and then infer the source composition from the

³By a strong shock it is meant that the disturbance propagates through the interstellar medium at a velocity much greater than the sound speed. This is certainly the case for the material ejected in supernova explosions where the velocities are about 10^4 km/s whereas the sound speed of the interstellar gas is at most 10 km/s.

observed primary abundances. Moreover, it is assumed that lifetimes for nuclear decay and fragmentation cross section are known.

The most common model describing the CR galactic confinement is the Leaky Box Model (LBM) [1], which assumes a constant and uniform distribution for sources and cosmic rays in the galaxy. In the framework of the LBM several results can be derived: the mean amount of material traversed by a typical cosmic ray before escaping the confinement volume can be estimated by the observed (local) abundances of the stable secondary light nuclei produced by spallation primary nuclei, and the confinement time of stable elements may be evaluated from the ratio between the density of radioactive and stable isotopes.

1.3 Heliospheric and magnetospheric effects

The space between the Sun and its planets is filled by a tenuous magnetized plasma, which is a mixture of ions and electrons flowing away from the Sun called the *solar wind*. In fact the Sun's atmosphere is so hot that not even the Sun's enormous gravity can prevent it from continually evaporating. The escaping plasma carries the solar magnetic field along, out to the border of the heliosphere where its dominance finally ends.

In the vicinity of the Earth, the intrinsic quasi-dipolar terrestrial magnetic field produces a cavity in the solar wind: the *magnetosphere*, which is characterized by a dense atmosphere and ionosphere⁴ and by a strong intrinsic geomagnetic field⁵, but no internal plasma sources other than the ionosphere.

The size of the magnetospheric cavity is determined by the magnetic pressure of the internal field on one hand, and on the solar wind dynamic pressure on the other. The magnetospheric boundary, the magnetopause, forms at a location where the solar wind and magnetospheric plasmas and magnetic fields are in pressure balance.

Typical solar wind conditions⁶ give a standoff distance of the magnetopause at about $10 R_E$ ($\simeq 60000$ km) upstream of the Earth, but under strong solar wind the magnetopause can be pushed well inside the geostationary orbit at $6.6 R_E$. In the antisunward direction, the solar wind flow deforms the dipolar magnetic field to a cometary taillike shape, where the magnetopause is on average about $30 R_E$ from the Sun-Earth line, depending on the solar wind pressure. The magnetotail extends far beyond the lunar orbit at least a few hundred R_E in the antisunward direction.

In the inner magnetosphere, particles trapped on closed orbits drifting around the Earth guided by the quasi-dipolar intrinsic geomagnetic field, form the so called

⁴Above 80 km altitude the solar ultraviolet radiation ionizes a small portion of the atmosphere gas creating what is known as the ionosphere. The ionosphere is coupled to the magnetosphere by highly structured and dynamic field aligned currents.

⁵The intrinsic geomagnetic field of the Earth has an intensity of $\sim 50 \mu\text{T}$ in the polar regions and of $\sim 30 \mu\text{T}$ at the equator.

⁶On average, the solar wind at Earth orbit has mean density of about 4 cm^{-3} , mean velocity of about 400 km/s , and mean interplanetary magnetic field (IMF) magnitude of 5 nT .

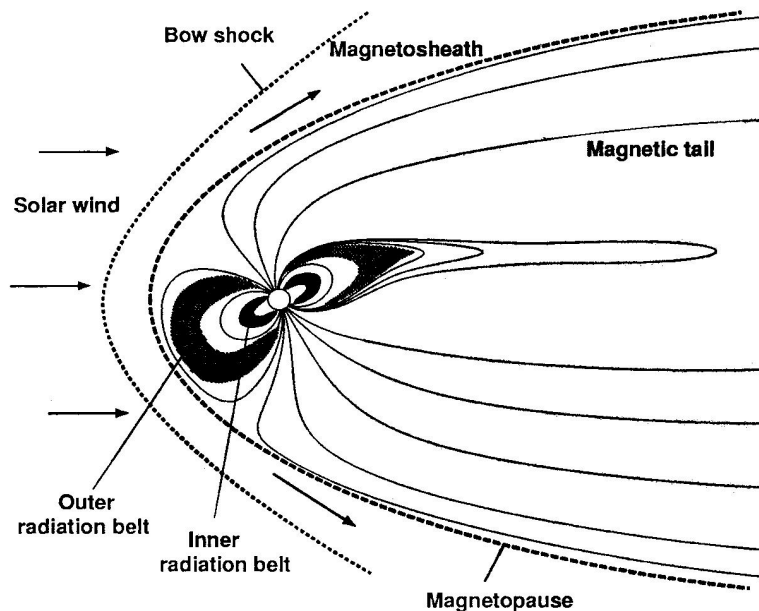


Figure 1.4: The Earth's magnetosphere embedded in the solar wind. Because of the inclination of the Earth's axis of rotation of 23° with respect to a line perpendicular to the ecliptic, and because of the deviation of the Earth's magnetic dipole axis from its axis of rotation of about 11° , the magnetosphere is not symmetric (the figure shows the extreme position). Interaction between the solar wind and the geomagnetic field leads to the bow shock, the magnetosheath and the magnetopause. The geomagnetic field is confined to the space within the magnetopause. Also shown are the Earth's radiation belts (Picture from L. Desorgher).

Earth's radiation belts.

The combined effects of the magnetic fields of the Sun and the Earth, and the solar wind form a highly complex electromagnetic configuration that influences the propagation of the cosmic radiation as it enters the heliosphere and the magnetosphere and approaches the Earth.

1.3.1 Geomagnetic effects

The relatively strong geomagnetic field in the vicinity of the Earth imposes a cut-off for low energy particles that varies as a function of geomagnetic latitude, which is different from the geographic latitude because the Earth's magnetic dipole axis does not coincide with its rotation axis. At the magnetic poles the geomagnetic cutoff is zero whereas at the geomagnetic equator it is $\simeq 15$ GV for vertical inci-

dence.

Aside from this latitude effect there is also a geographic longitude effect which is due to the fact that the geomagnetic dipole axis is inclined with respect to the Earth's axis of rotation and laterally displaced.

Furthermore the geomagnetic field configuration and the positive charge dominance of the primary radiation produce differences in the fluxes and spectra of cosmic ray coming from the eastern and western directions up to rigidities of about 60 GeV (*east-west asymmetry*).

In addition there are magnetic anomalies, the most significant one being the *South Atlantic Anomaly*, off the coast of Brazil (Figure 1.5). The SAA is a dip in the Earth's magnetic field which allows cosmic rays to reach lower into the atmosphere enhancing particle flux. In this region the offset and the tilt of the geomagnetic axis with respect to the Earth's rotation axis brings the lower edge of the inner radiation belts to low altitudes (~ 200 km).

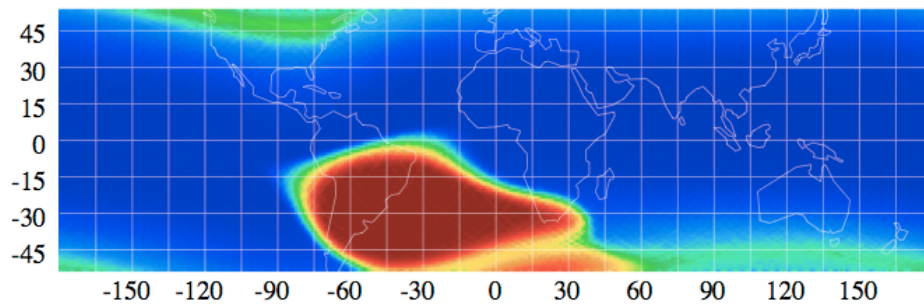


Figure 1.5: SAA image from the South Atlantic Anomaly Detector (SAAD) on board the ROSAT [43] satellite (From Ref. [44]). On the x and y axis are shown the geographic longitude and latitude respectively. ROSAT was launched on June 1, 1990 into an orbit of 53° inclination and 580 km altitude to perform X-ray astronomy observations. The SAAD germanium detector measured the charged particles rate and served as particle background monitor [45]. The mission ended on September 22, 1999.

1.3.2 Time variation and solar modulation effects

The solar activity influences the cosmic ray flux on Earth and the shape of the energy spectrum up to about 50 GeV/n in various ways.

The solar wind is a plasma consisting mainly of highly ionized hydrogen, some helium and other nuclei, and an approximately equal number of electrons, continuously flowing away from the Sun into the interplanetary space with a velocity of about 300 km/s to 800 km/s. It manifests latitude and longitude dependence and time variations coupled with solar activity. Because of the high conductivity of the

interplanetary plasma the solar wind transports the frozen-in magnetic field from the Sun into space.

A bow shock occurs where the inflowing interstellar wind first encounters the heliospheric field. Variation of the solar activity affects the magnetic field in the heliosphere and the spectrum of the cosmic radiation within it.

Generally the solar wind flow is diverted around the Earth by the terrestrial magnetosphere. Solar wind particles cannot enter, unless there occurs a process called *magnetic reconnection* of interplanetary and geomagnetic field lines. Disturbances due to local solar activity cause irregularities in the flow of the solar wind and the associated interplanetary magnetic field (IMF). If the Earth is engulfed in such a disturbance, magnetic reconnection of the interplanetary magnetic field and the geomagnetic field lines can occur. Consequently the magnetospheric magnetic field configuration is perturbed and this can significantly change the cutoff conditions for cosmic rays and solar particles.

Energy transfer is most efficient when the reconnection takes place at the dayside magnetopause, which occurs when the IMF is antiparallel to the intrinsic geomagnetic field. Variability in the north-south orientation of the IMF causes episodic energy loading-dissipation cycles called magnetic substorms.

After the onset of dayside reconnection, energy is loaded into the magnetotail, where reconnection creates a plasmoid which is then ejected tailward into the interplanetary space (Figure 1.6).

Half of the energy loaded into the magnetosphere by dayside reconnection is dissipated through this mechanism, while the rest is processed in the inner magnetosphere and ionosphere.

Magnetospheric substorms require energy transfer periods ranging from 30

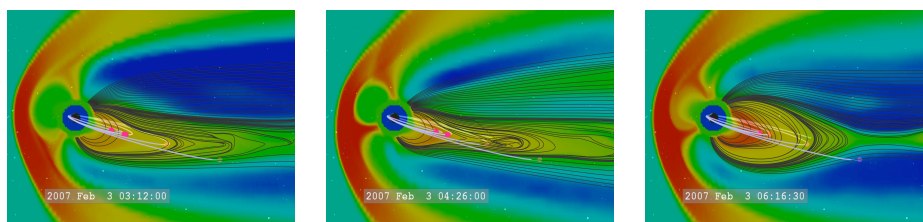


Figure 1.6: Substorm simulation from the NASA/Goddard Space Flight Center Scientific Visualization Studio [46]. The purple dots show the position of the five THEMIS [47] spacecraft, launched on February 17, 2007 to study the physical processes occurring in near-Earth space during substorms. Left: The solar wind pressure (color-coded: red is high, blue is low) stretches the geomagnetic field lines (black curves) antisunward (right). Middle: The substorm event is initiated, a plasmoid starts to grow in the magnetotail. Right: After magnetic reconnection the plasmoid is ejected antisunward back to the interplanetary space and the geomagnetic field lines pull the plasma sunward.

minutes to about one hour. If the energy loading last more than 3 hours a magnetic storm occurs, which is also accompanied by magnetic substorms. Such long periods of enhanced energy transfer are generally originated by coherent solar wind structures.

The solar and magnetospheric processes pose several time scales ranging from solar cycle and longer (long-term solar activity variations) to 27 days (recurrent solar activity), days (magnetic storms), hours (magnetospheric substorms) and even minutes and seconds (particle acceleration events, plasma instability growth times).

Periodical CR variations

By monitoring the cosmic ray flux over many years [48], it has been found that the average flux varies with a period of 11-years equivalent to the solar cycle period and is anticorrelated with the solar activity: during high solar activity the cosmic ray intensity is lower and viceversa during the quiet Sun the cosmic ray intensity is higher (Figure 1.7).

The 11-year variation is due to changing magnetic conditions in the heliosphere that influence the penetration of low energy galactic cosmic rays [51]. Stronger magnetic fields and an enhanced degree of turbulence reduce cosmic ray intensity in the heliosphere or prevent them from entering the inner heliosphere because of

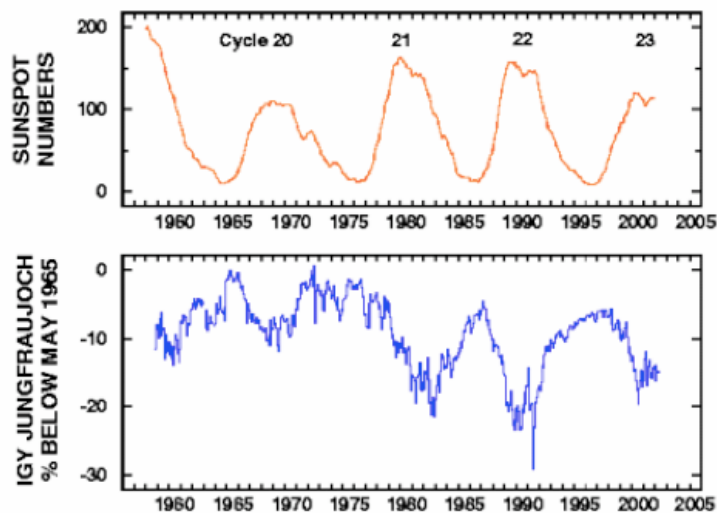


Figure 1.7: Anticorrelation between the sunspot numbers (top panel) and the cosmic ray flux intensity measured by the IGY Jungfraujoch neutron monitor [49] (bottom panel) for the last four solar cycles (From Ref. [49]). During high solar activity periods (solar maxima) higher number of sunspots are observed on the Sun surface with respect to low solar activity periods (solar minima).

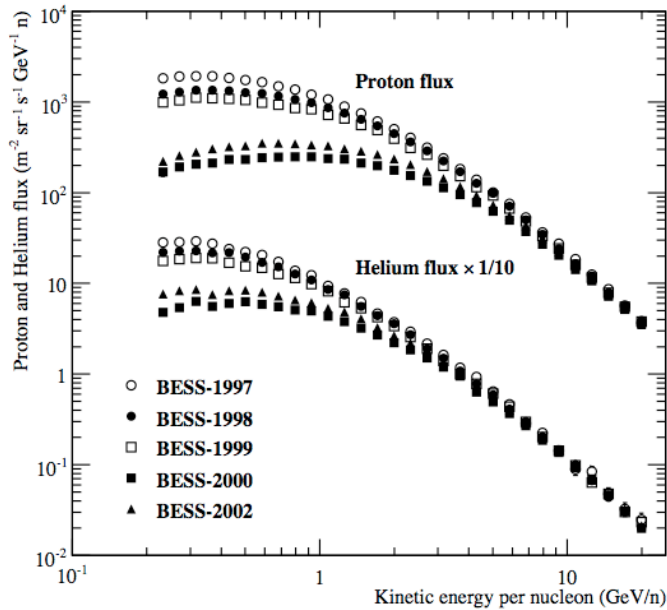


Figure 1.8: Solar modulation effect on the cosmic-ray proton and He fluxes observed at the top of the atmosphere by the BESS balloon experiment [50]. Note the flux decrease during the high solar activity year 2000, with respect to the low activity year 1997.

deflection, thus reducing the local intensity of the cosmic radiation [52].

More subtle additional variations are observed that are probably linked to the polarity reversal of the heliospheric magnetic field which occurs at successive sunspot maxima (~ 11 years apart) and has a periodicity of approximately 22 years [53].

In Figure 1.8 it is shown how the 11-year modulation affects primary proton and helium spectra. The modulation effects cease to influence particles having energies larger than a few GeV/n.

Annual geomagnetic activity variations are also observed due to the changing orientation of the Earth's dipole axis relative to the Sun-Earth line over the course of the year. The activity is larger during the equinoxes when the dipole is tilted along the Earth's orbital track and the projection of the IMF to the geomagnetic field maximizes (Russel-McPherron effect) [54]. Similarly the activity level is at minimum during solstices when the projection of the IMF to the geomagnetic field is on average at minimum.

Further periodical variations in cosmic ray intensity are observed in relation to the 27-day rotational period of the Sun [55].

Forbush decreases

On many occasions, world-wide cosmic ray intensity decreases between a few percent and about 20% have been observed. The decrease occurs suddenly, within a few hours or less, but the subsequent recovery to the previous level takes days or even weeks. Such events are usually associated with geomagnetic storms and are called Forbush decreases [56,57] (Figure 1.9).

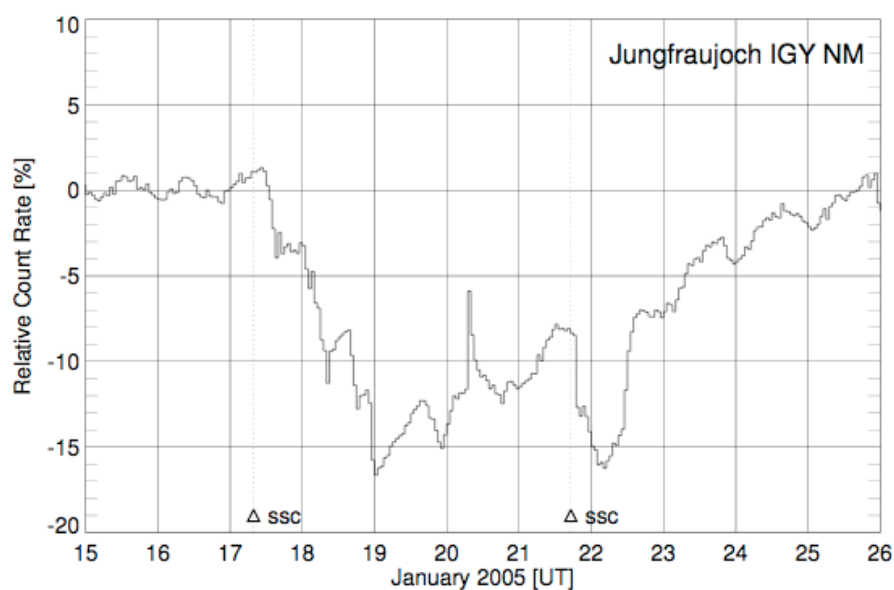


Figure 1.9: Relative counting rate of the IGY neutron monitor at the Jungfraujoch during the Forbush decrease of January 2005 [58].

The general mechanism responsible for Forbush decrease is believed to be a solar wind effect. At the time of occurrence of a solar flare (SF) [5]⁷ accompanied by a coronal mass ejection (CME) [5]⁸ from an active region of the Sun, the ejected plasma cloud with associated magnetic fields may have a higher velocity than the normal plasma stream and may produce a shock wave. A magnetic bottle may be formed with relatively high field strength. If the Earth is within it, the low energy galactic cosmic radiation is prevented from reaching it.

⁷Solar flares are sporadic local eruptions of the chromosphere. They develop suddenly and rapidly, in minutes, and cover a relatively small region of the solar surface. Initially they manifest themselves by a localized sudden brightening. They are accompanied with the emission of a broad spectrum of electromagnetic radiation, including X- and gamma ray emission, and relatively energetic particles, predominantly protons but also electrons, helium and small quantities of heavier nuclei.

⁸Coronal mass ejections are highly energetic transient events on the Sun in the course of which huge amounts of gas are ejected from the Sun into interplanetary space. CMEs cause gigantic plasma clouds to leave the Sun, which then drive large-scale density waves out into space.

Solar energetic particles

In comparison to the universal cosmic ray spectrum that extends to energies well over 10^{10} GeV, particles emitted by the Sun, even in the most violent solar processes, are of very low energy. Their spectrum extends at most up to about 10 GeV, in some cases particles having energies as high as 50 GeV were reported [59]. However, with respect to the bulk of the radiation from the Sun, particles that are associated with energetic solar events, such as solar flares or coronal mass ejections, that may reach energies as high as 10 GeV and more, are of comparatively high energy for the solar regime. Thus the term of solar energetic particles (SEP).

Not all solar flare events produce particle fluxes that are observable on Earth. Since Carrington's discovery of the apparent connection between strong flares and geomagnetic activity in 1859 [60], this connection has been considered a cause and effect relation for many years [61], despite some obvious shortcomings. Only in the 1980s, it became clear that the only type of solar transient that has a unique cause and effect relation to geomagnetic activity lies in CMEs, not in flares [62].

In fact it has been shown that every CME launched with a speed exceeding 400 km/s eventually drives a shock wave [63–65], which then can be observed in situ, provided that the observer is located within the angular span of that CME. If this shock and the frequently following ejecta cloud hits the Earth, geomagnetic effects may occur, provided some conditions on the orientation of the interplanetary magnetic field are also fulfilled. In reverse, every shock wave observed in space (except the ones at corotating interaction regions) can uniquely be associated with an appropriately pointed CME at the Sun.

No similar cause and effect relation can be made for solar flares. Indeed there are many CMEs (with geoeffects) without associated flares, and there are flares without associated CMEs (and without geoeffects). However, for the very big events like the one observed by Carrington, strong X-ray flares and large CMEs usually occur in a close timely context [66]. It is now commonly thought that both flares and CMEs, are just the effects of a common underlying magnetic phenomenon at the Sun [67].

The various highly dynamic processes in the magnetized coronal and interplanetary plasma can cause major acceleration of the charged particle populations. The main locations for electron and ion acceleration are flare sites and shock waves in the corona and in the interplanetary space [5,68]. The energy of SEPs reaches from a few keV to some GeV (Figures 1.11 and 1.10). Sometimes the fastest particles obtain more than half the speed of light, and they arrive at Earth only a few minutes after the light flash.

The acceleration of particles to such high energies on time scales of seconds or minutes as well as their propagation through space is still not well understood and active research is going on [68, 69].

It is now widely agreed that SEPs come from two different sources with different acceleration mechanisms working: the flares themselves release impulsive events while the CME shocks produce gradual events [5, 6, 68]. The SEPs from

flares often have major enhancements in He^3/He^4 and enhanced ion abundances [70], because of resonant wave-particle interactions in the flare-site, and the ions have very high ionization states. However the most intense SEP events, also with the highest energies, are produced by CME driven shocks. These SEPs reflect the abundances and ionization states of the ambient coronal material.

The gradual events are dominated by protons, with a small peak at shock passage [70]. The smooth and extended profile comes from continuous acceleration at the moving CME shock. In the impulsive event the electron fluxes are higher than those of the protons and those of the gradual event, respectively. The comparatively short duration of the impulsive event is determined by scattering of the particles as they traverse interplanetary space.

At the biggest flares, particles are accelerated to energies of several GeV (Figure 1.10). Upon interaction with other atoms they cause nuclear reactions which release gamma rays and relativistic neutrons [72, 73] that can reach the Earth fully unhindered. Even if it is difficult to differentiate solar neutrons from those neutrons generated as byproducts of spallation of atmospheric atoms struck by SEPs, detection of Ground Level Enhancements (GLEs) of neutron flux provides an effective mean of studying the angular distribution and energy spectrum of SEPs.

As an example the measurements performed by PAMELA, GOES and the McMurdo neutron monitor [74] during the SEP event occurred in December 2006 are reported in Figures 1.10 and 1.11, respectively.

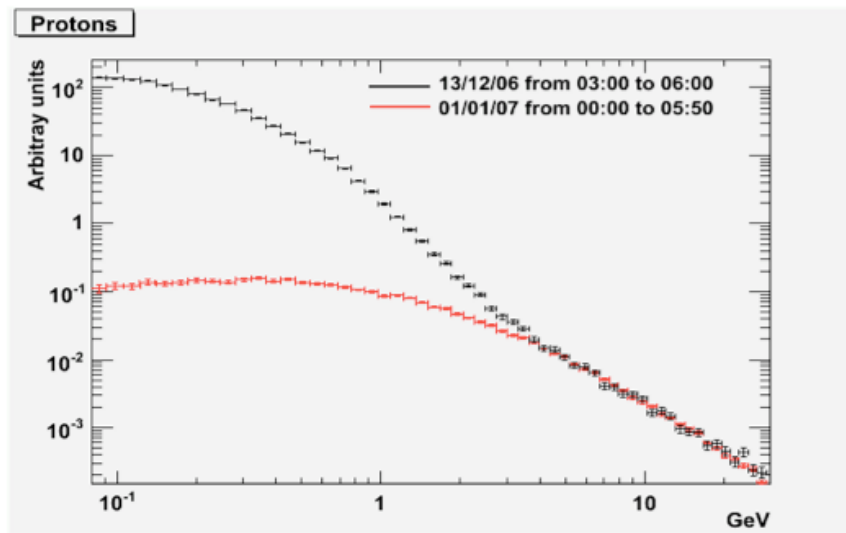


Figure 1.10: The Solar Energetic Particle event of December 2006 as observed by the PAMELA spacecraft. The low-energy (< 5 GeV) proton flux during the SEP event (black line) is highly enhanced with respect to a quiet period (red line) (From Ref. [71]).

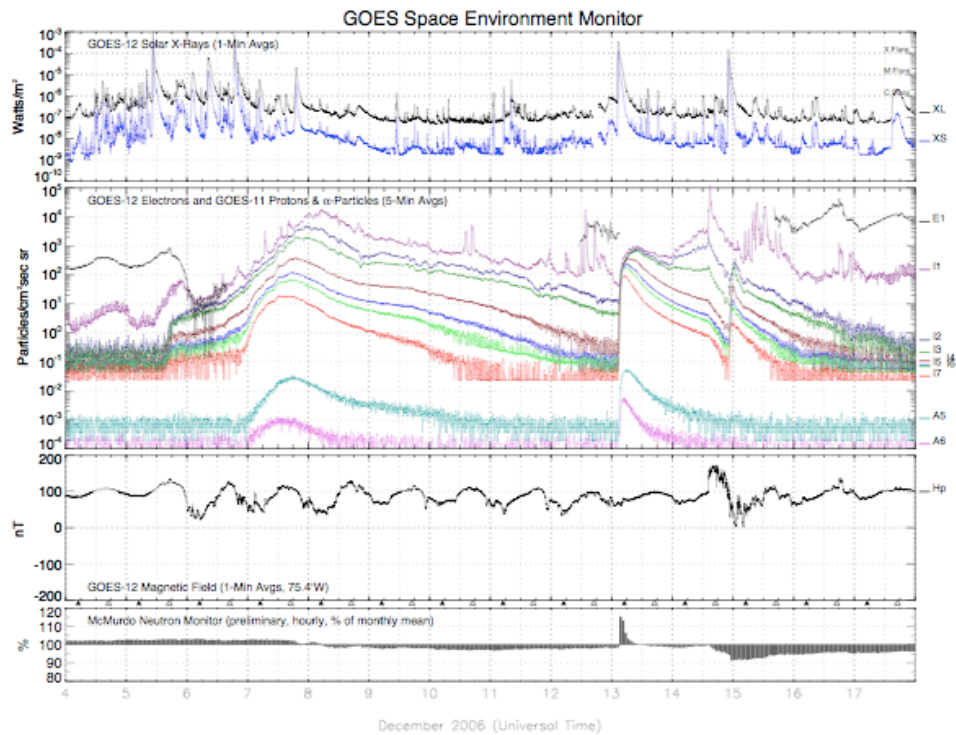


Figure 1.11: The Solar Energetic Particle event of December 2006 as observed by the GOES satellite (from top to bottom) X-ray Sensor (XRS), Energetic Particle Sensor (EPS) and Magnetometer, and the McMurdo neutron monitor (From Ref. [11]). The XRS provides whole-sun X-ray (XL: 1–8 Å, XS: 0.5–3 Å) fluxes, on the left vertical scale is indicated the solar flare classification. The ESP are solid-state discrimination detectors sensitive to > 2 MeV electrons (E1), > 100 MeV protons (I1-I6) and 150 – 500 MeV He nuclei (A5, A6). The Magnetometer measures the Interplanetary Magnetic Field (IMF) vector: the plot shows the component HP perpendicular to the satellite’s orbital plane. Note the Ground Level Enhancement registered by the McMurdo neutron monitor in correspondence to the increased solar particles flux on December 13, and the Forbush decrease which sets on in correspondence to the sudden variation of the IMF at noon of December 14.

Chapter 2

The Alpha Magnetic Spectrometer Precursor Flight

Prior to the main AMS mission a prototype detector, AMS-01 [21], was flown on board the NASA Space Shuttle *Discovery* during the STS-91 Mission in June 1998 in a 51.7° orbit at altitudes between 320 and 390 km. The main purpose of the flight was to test the spectrometer design principles and to gain experience in the operation of the detector under real space flight conditions. During the 10 day mission a vast amount of data on the fluxes of different cosmic particles in near Earth orbit was collected. Analysis of those data led to significant physics results on rates and spectra of charged cosmic rays [25,75–78] in the kinetic energy range from 0.1 GeV/n to ~ 100 GeV/n, and provided the most precise upper limit at the time on the ratio of the flux of antihelium to the flux of helium [79]. This chapter gives a brief description of the main components of the AMS-01 detector, of its performance characteristics, as well as its operation during the flight.

2.1 The AMS-01 detector

A schematic view of the AMS-01 apparatus is shown in Figure 2.1. The core of the detector is a magnetic spectrometer: a permanent magnet, with a field strength along the +X-axis of about 0.15 T at the center, enclosing six silicon microstrip tracker planes (T1-T6). Only 38% of the tracker planes surface was equipped with silicon sensors, resulting in a limited acceptance of ~ 0.3 m²sr for events within 4 tracker planes. A layer of anticoincidence scintillator counters (ACC) covering the inner surface of the magnet served as veto counter, detecting particles traversing the apparatus outside the detector main acceptance and background particles which could be produced by interactions in the detector material. The primary trigger was provided by the Time of Flight (TOF) hodoscopes (S1-S4) placed above and below the magnet. At the very bottom of the detector two layers of a threshold Cerenkov counter completed the apparatus. To minimize the dead time, low energy particle shields (LEPS) were mounted on top of the upper hodoscope planes to absorb

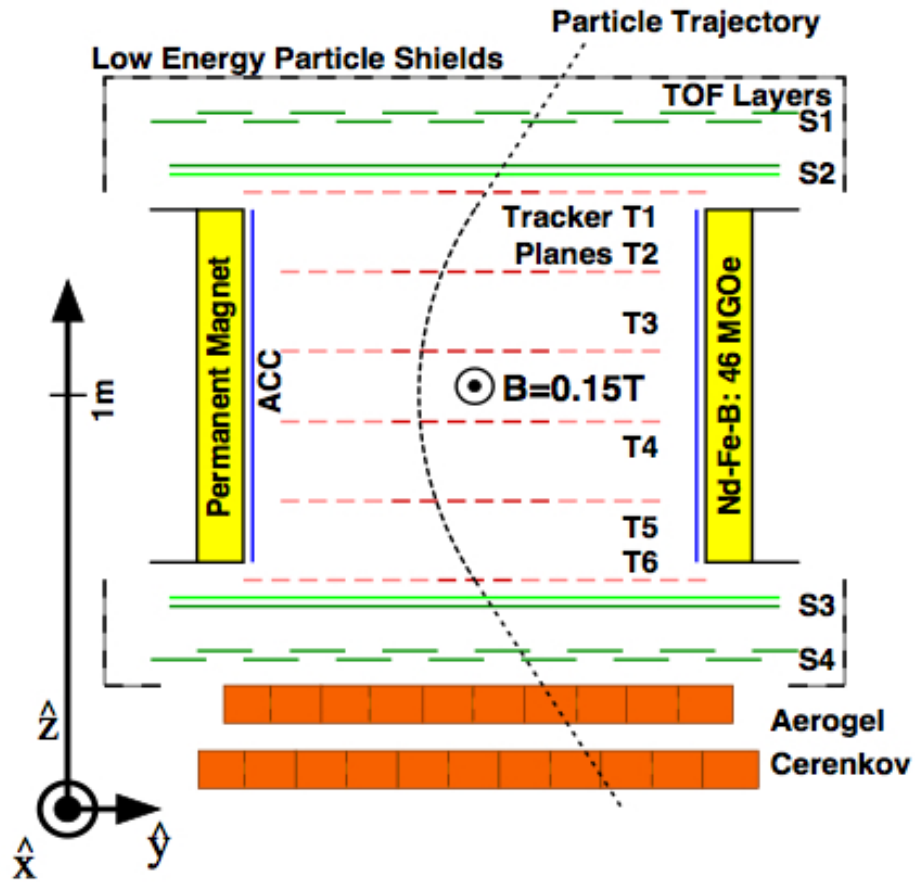


Figure 2.1: Schematic view of the AMS-01 detector.

particles with energy less than 5 MeV.

The Silicon Tracker reconstructed the trajectory of charged particles traversing the spectrometer. The particle rigidity resulted from the sagitta of the reconstructed track, while the sign of the particle charge was deduced from the track curvature. The absolute value of the charge was redundantly determined by the energy losses in the TOF counters and in the tracker planes. The particle velocity and arrival direction were given by the TOF system measurements.

2.1.1 The Magnet

The AMS-01 magnet was designed to achieve the largest possible geometrical acceptance and bending power, minimizing the weight and the flux leakage [80]. Furthermore the total magnetic dipole moment of the system had to be small enough to prevent a torque on the vehicle, that could arise from the interaction with the Earth's magnetic field. With these requirements the geometry of a cylindrical shell with a

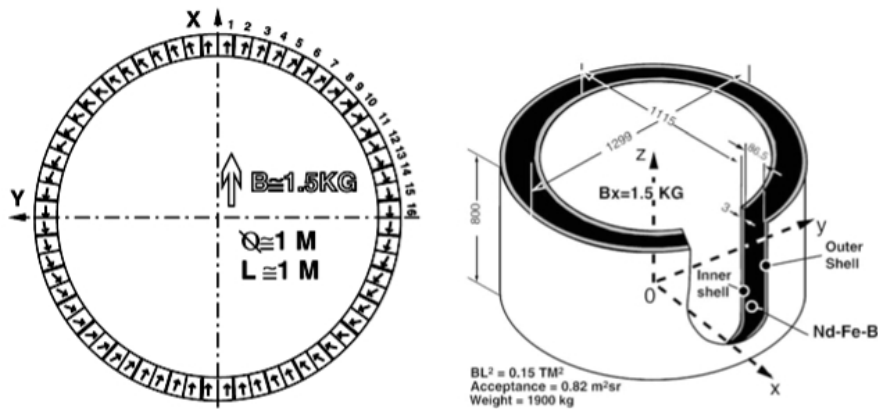


Figure 2.2: Left: Magnetization vector orientation of the AMS-01 magnet sectors. Right: The AMS-01 magnet.

length of 0.800 m, an inner diameter of 1.115 m and an outer diameter of 1.298 m was chosen, resulting in a geometrical acceptance of $0.82 \text{ m}^2\text{sr}$. The magnet was made of 64 sectors. Each sector was composed of 100 high-grade $\text{Nd}_2\text{Fe}_{14}\text{B}$ alloy with an energy level of $(\text{BH})_{\text{max}} = 50 \times 10^6 \text{ GOe}$ ($\approx 4 \text{ J/m}^3$). To achieve an almost homogeneous dipolar field orthogonal to the magnet axis in the whole volume, the direction of the magnetization vector in each sector changed with the polar coordinate, as schematically shown in Fig 2.2. This configuration produced a dipole field of 0.15 T and a negligible dipole moment. The resulting bending power was $BL^2 = 0.15 \text{ Tm}^2$. Before the construction of full scale magnets, many smaller magnets were built to confirm and measure the field inside the magnet, the dipole moment and the flux leakage. Three full scale magnets were built: the first was used in acceleration and vibration tests for space qualification, the second magnet was the flight magnet and the third one was built without glue for NASA safety tests¹. The space qualification tests included stress analysis, eigenstate frequency measurements, high temperature check for irreversible magnetization loss, as well as centrifugal and destructive tests. Finally all requirements were met, the magnet weighting 2.2 tons, including the support structure, the fringe field being below 3 G anywhere at a distance of 2 m from the magnet center² and the maximum torque being less than 0.72 Nm in a 0.5 G magnetic field³, since the single dipole moments cancel pairwise.

¹The glue performance over an extended period in the space environment was not known, so the third magnet was constructed to be tested to destruction to ensure that AMS could be returned on the Shuttle to Earth even if the glue completely failed.

²NASA requires the leakage field to be less than 60 G so as not to interfere with the life support system of the astronauts.

³The Earth's magnetic field is $\sim 0.5 \text{ G}$.

2.1.2 The Silicon Tracker

Silicon detectors, commonly used as tracking devices in ground-based accelerator experiments, were operated in space for the first time in the AMS-01 detector. Double-sided microstrip sensors similar to those used for the ALEPH and L3 microvertex detectors at the Large Electron-Positron collider (LEP) at CERN were used. The AMS-01 Tracker (Figure 2.3) consisted of six layers of silicon

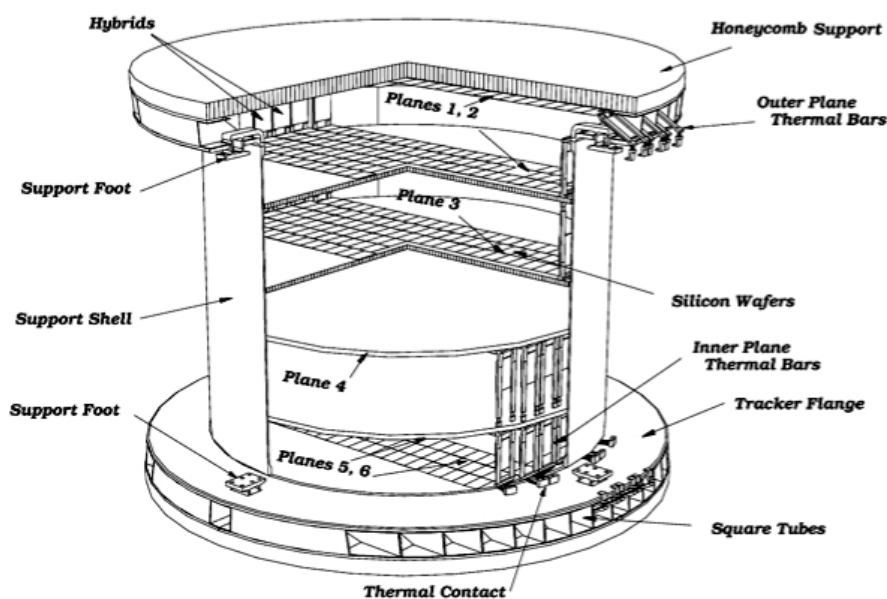


Figure 2.3: The AMS-01 Silicon Tracker. Ladders installed for the STS-91 flight are visible.

sensors mounted on supporting planes made of an ultra-light composite structure (aluminum honeycomb and carbon fiber foils). The average material thickness of an inner plane including ladders was equivalent to $0.65\% X_0$ at normal incidence. In the AMS-01 detector only the central part of each tracker plane was equipped with silicon sensors, oriented with the n-side strips parallel to the magnetic field lines. A carbon fiber cylindrical shell supported the inner planes (2 to 5) and two carbon fiber flanges supported the two outer planes, 1 and 6.

The sensor design made use of capacitive charge coupling with implantation strip pitches of $27.5 \mu\text{m}$ for the p-side and of $26 \mu\text{m}$ for the n-side, where the p-side measured the coordinate in the bending plane and the n-side in the non-bending plane. The corresponding readout pitches were $110 \mu\text{m}$ and $208 \mu\text{m}$ respectively. The silicon sensors were grouped together for readout and biasing in ladders (Figure 2.4) of variable lengths to match the circular geometry of the planes. A metalized kapton foil, glued directly to the silicon sensors, served as routing cable to bring the n-side signals to the n-side front-end hybrid electronics. The p-side front-

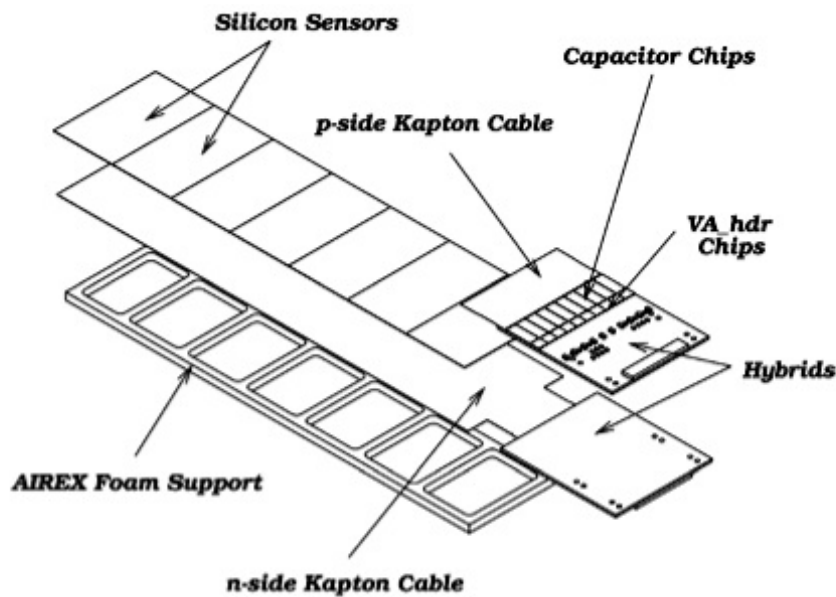


Figure 2.4: A Silicon Tracker ladder viewed from the p-side.

end hybrid was connected to the strips by a short foil. The two hybrids, mounted back to back, were enclosed by an aluminum box. To evacuate the heat generated by the front-end electronics from the tracker inner volume to the exterior, the hybrid boxes were connected to carbon fiber-metal cooling bars located at the plane border near the inner bore of the supporting shell.

The front-end electronics were designed for low-noise, high dynamic range and low power consumption. The readout strips were grouped into logical units of 64 channels. A signal, after passing a decoupling capacitor, was fed into a charge amplifier, the VA_HDR chip. After signal shaping and sampling, the chip was sequentially read out at a rate of 5 MHz by an analog multiplexer. Further amplification and digitization of the signals occurred on the Tracker Data Reduction (TDR) boards, located outside the Magnet in the electronics crate. The TDR boards performed also the calibration of the Tracker, which consisted in the determination of the pedestal values and their widths for each readout channel, and of the VA common noise for each preamplifier chip.

The Silicon Tracker provided a tracking resolution of $10 \mu\text{m}$ in the bending direction and of $30 \mu\text{m}$ in the orthogonal direction. The track reconstruction allowed for the determination of the particle rigidity. The rigidity resolution was limited at low energies (below a few GeV) by multiple scattering, and at high energies by the intrinsic spatial resolution and bending power. The AMS-01 Tracker provided a momentum resolution of 10% in the rigidity range 1 to 10 GV (Figures 2.5 and 2.6).

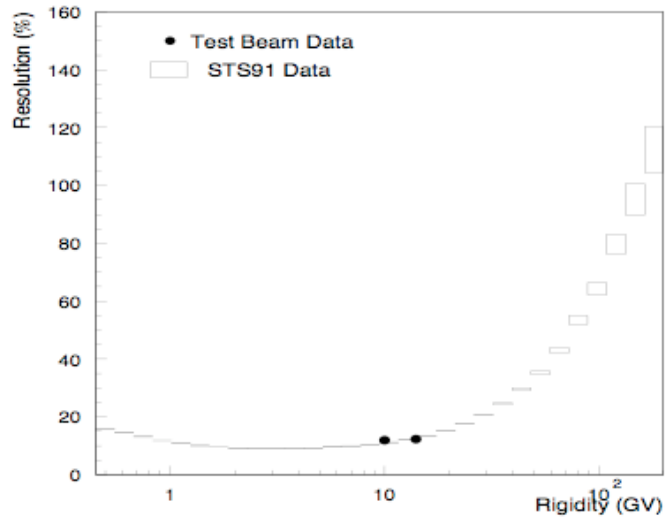


Figure 2.5: Rigidity resolution for $Z = 1$ flight data (histogram) compared with proton test beam data (points) (From Ref. [81]).

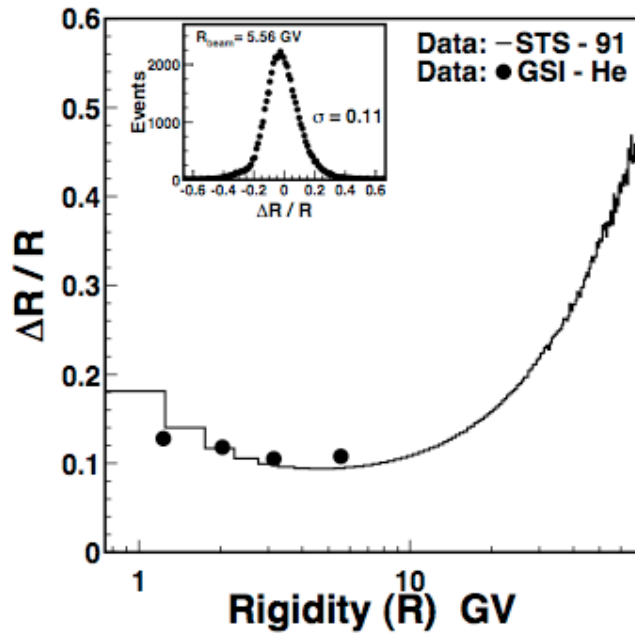


Figure 2.6: Rigidity resolution for $|Z| = 2$ flight data (histogram) compared with the GSI He test beam (points). Inset: Typical rigidity resolution, $\Delta R/R$, from the GSI He data (From Ref. [79]).

Furthermore the specific energy loss in the silicon, $dE/dx \propto Z^2$, provided a measure of the absolute charge of light nuclei [82], while the charge sign was determined by the curvature of the track in the magnetic field.

During the flight the Silicon Tracker worked as designed, unaffected by the launch and operation in space. Calibrations were made automatically every 30 minutes during data taking.

The calibration results showed that the pedestals and the pedestal widths of all channels during the flight were very close to their pre-launch values. The measured noise level, σ_{ped} , was less than 4 ADC on the n-side and less than 3 ADC on the p-side, showing linear correlation with the measured temperature (Figure 2.7). During the whole flight the average common noise widths were stable within ± 0.5 ADC at the level of 7 ADC and 10 ADC channels for the p- and n-side chips respectively.

The energy losses from fired strips yielded the center of gravity of the cluster charge and consequently the coordinate. The online clustering of the TDR used a threshold of $3\sigma_{ped}$ to define a seed strip, neighboring strips were included if their signals exceeded $1\sigma_{ped}$.

The ratio between the total cluster charge and the root-mean-square of the pedestal widths of the member strips defined the cluster signal-to-noise: $\sum_i s_i / (\sum_i \sigma_i^2)^{\frac{1}{2}}$, where s_i and σ_i are the strip signal and pedestal width.

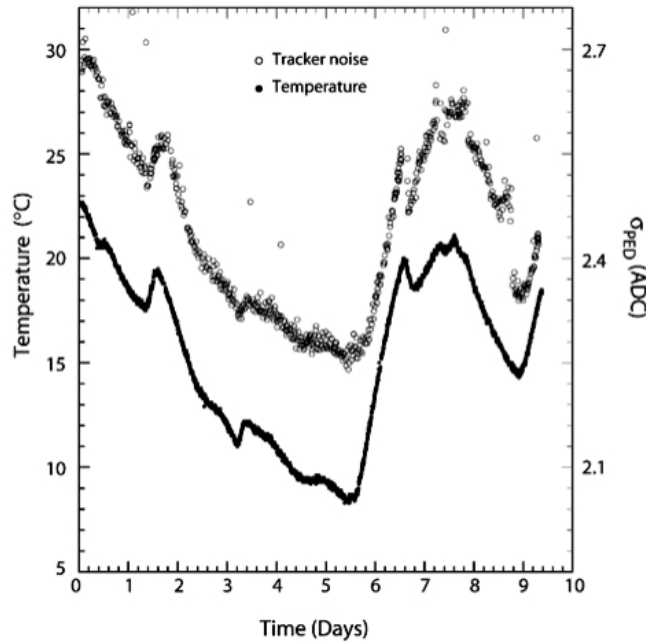


Figure 2.7: Tracker noise and temperature during the flight.

The cluster charges were normalized to correspond to the 300 μm path-length in the silicon and corrected to $\beta \geq 0.95$, i.e. for β smaller than 0.95 the cluster charge was multiplied by a factor $(\beta/0.95)^{\frac{1}{2}}$. The cluster signal-to-noise during the flight varied in a manner that reflected the noise behavior described above.

The signal-to-noise ratio was stable throughout the whole period of tracker assembly, preflight tests and flight at the level of about 7.5 : 1 and 4 : 1 for the p- and n-side respectively. Because of the lower signal-to-noise performance of the n-side, the fraction of proton tracks with 4, 5 and 6 planes which were reconstructed without n-side information is 50%, 58% and 67% respectively. For the $|Z| > 2$ nuclei the fraction of reconstructed tracks without n-side information is less than 10%.

2.1.3 The Time Of Flight hodoscopes

The scintillator hodoscopes consisted of two identical double planes of coincidence counters situated at the top and the bottom of the magnet. Each plane consists of paddles (Figure 2.8) of scintillator of different length. To avoid inefficiency in particle detection the adjacent paddles had a 5 mm overlap.

The paddles of a double plane were orthogonal to each other to allow the measurement of the x and y coordinates of the particle impact point. Each scintillator paddle was connected on both ends to three photomultipliers (PMs) via light guides. To avoid performance degradation, the PMs and the electronic circuits were shielded from the residual magnetic field (~ 200 G) by a 0.5 mm thick shielding case made of permalloy.

To extend the dynamic range of the TOF system, the signals from the three PMs on each side were summed to provide one signal from the anodes and one from the 2nd to the last dynodes and then transferred to the readout electronics. The anode signals were discriminated to reproduce a logical signal sent to the AMS-01 trigger electronics defining the fast trigger signal. The analog signals from both anodes and dynodes were addressed to the readout electronics, based on Time to Digital Converter devices, which provided the time information.

The absolute transit time t in the TOF for a particle was obtained from the average value of the measurements on the two sides of a counter, t_1 and t_2 , as:

$$t = \frac{t_1 + t_2}{2}. \quad (2.1)$$

The position along the X – or Y – axis was derived by the difference between the two time measurements:

$$x = v_{eff} \frac{t_1 - t_2}{2}, \quad (2.2)$$

where $v_{eff} (\sim 15.5 \text{ cm/ns})$ is the effective velocity of light in the scintillator paddle. The spatial resolution was better than 2 cm. The time measurement provided by the TOF had a resolution of about 125 ps. The minimum time of flight of relativistic particles traversing the TOF system⁴ was 5 ns. The arrival direction of a

⁴The upper and lower TOF planes were 150 cm apart.

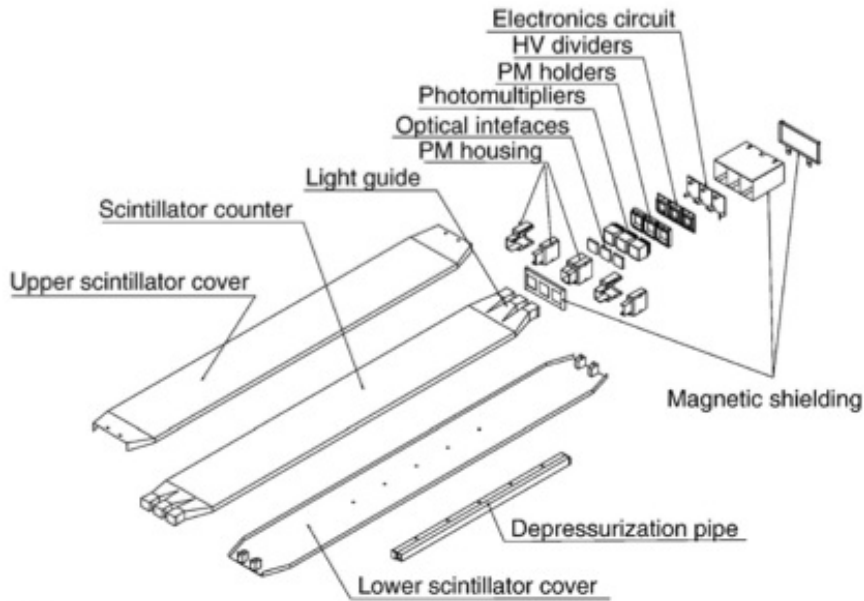


Figure 2.8: Exploded view of one TOF scintillator paddle.

particle traversing the detector could therefore be determined with very high reliability. The particle velocity β was derived from the time of flight measurement with relative resolution of about 0.025. Furthermore the measurement of the particle energy loss in the scintillator counters provided a redundant determination of the absolute charge. The anode dynamic range allowed the measurement of the particle charge up to $|Z| = 2$ to 3. The dynode signal extended the measurement range by a factor of about 5.

The accuracy in the time of flight measurement obtained using the flight data was in agreement with the test measurements made before the flight. The performance of the TOF system proved to be stable throughout the Shuttle mission.

2.1.4 The Aerogel Cerenkov Counter

The Aerogel Threshold Cerenkov (ATC) counters were located at the bottom of the detector below the lower TOF plane. The elementary component was the aerogel cell, composed by eight aerogel blocks with refractive index $n = 1.035$ wrapped in Teflon and connected to a photomultiplier through a light guide. To reduce Cerenkov photon losses due to Rayleigh scattering and to absorption, both decreasing with increasing photon wavelength, a wavelength shifter is placed in the middle of each cell. The shifter transformed the 300 nm Cerenkov photons to 420 nm photons. The wavelength of the shifted photons matched the maximum efficiency of the photomultiplier. The use of the shifter resulted in a 40% increase of the number of

photoelectrons. The 168 cells were arranged in two layers, shifted one with respect to the other to minimize the loss of track passing in between the cells.

A charged particle traversing the aerogel with velocity β greater than the velocity of light in that medium emitted electromagnetic radiation. The emission angle θ_c is related to the particle velocity β and to the refractive index of the traversed medium n as follows:

$$\cos(\theta_c) = \frac{1}{\beta n}. \quad (2.3)$$

This defines the threshold emission velocity $\beta_t = 1/n$, which can be translated into a threshold momentum

$$p_t = \frac{mc}{\sqrt{n^2 - 1}} \quad (2.4)$$

for a given mass m , allowing separation between leptons and hadrons. The number of photoelectrons, which is proportional to the squared charge of the particle, Z^2 , and to $\sin^2 \theta_c$, gives a redundant measurement of the absolute charge and the velocity of above threshold particles. The choice of the aerogel was a compromise between velocity threshold and photoelectrons yield. The ATC used the same readout electronics as the TOF counter, but optimized to accept much lower input signals of few photoelectrons. The ATC performance test and calibration were done using test beam at CERN and cosmic ray particles collected prior and during the flight. The response to $\beta = 1$ particles (above the electronics threshold) was measured to be 3.51 ± 0.02 photoelectrons for the upper plane and 4.02 ± 0.02 for the lower plane.

The ATC information is essential for antiproton and positrons detection, allowing \bar{p}/e^- and e^+/p discrimination. In the analysis presented in this work the information of the ATC counter is not used, because the study concerns the dominant proton, electron and He nuclei fluxes only.

2.2 AMS-01 Operations

In 1998 the AMS-01 detector was flown on the NASA Space Shuttle *Discovery* during the STS-91 mission. The main purpose of the mission was to deliver logistics and supplies to the Russian Space Station Mir completing the first phase of the cooperative program between Russia and USA in space exploration, before starting the construction of the International Space Station. *Discovery* was launched on June 2nd from Kennedy Space Center Launch Complex and returned to Earth on June 12th after almost ten days in space.

2.2.1 Flight Parameters

The AMS-01 detector was located in the Shuttle cargo bay (Figure 2.9) during the entire mission. The Shuttle orbit had an inclination of 51.7° orbit and the altitude varied between 320 and 390 km. On June 4th, after about 40 hours flight, *Discovery* met the Mir station and stayed docked to it until June 8th. On June 12th

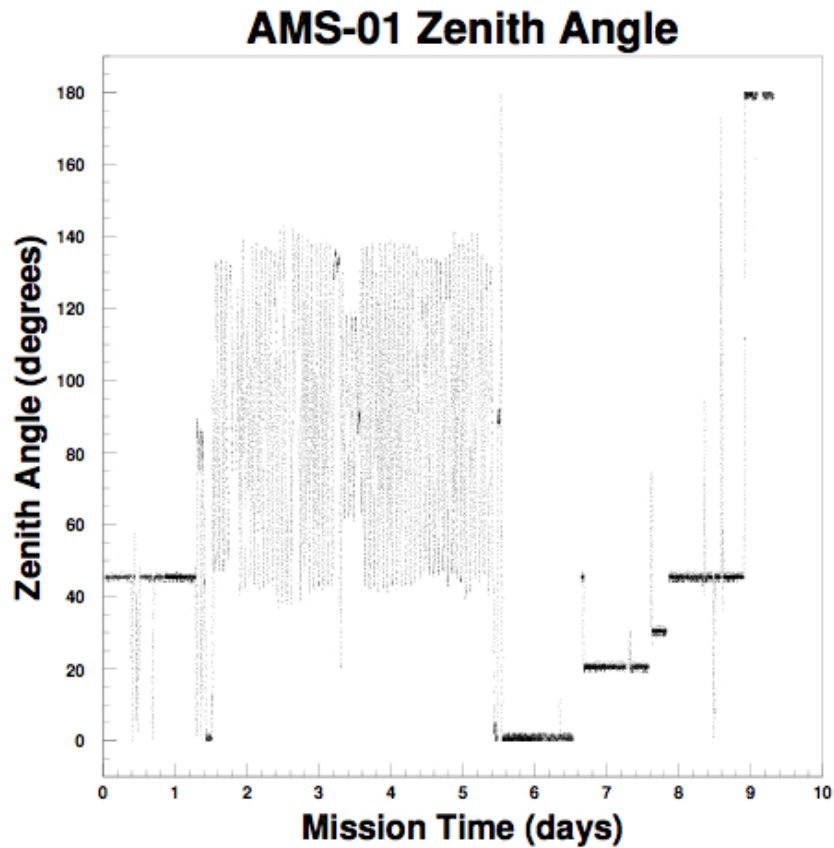


Figure 2.10: Angle of the AMS-01 Z-axis relative to Zenith versus Mission Elapsed Time. Note the MIR docking period characterized by large scatter in Zenith angles.

2.2.2 Trigger and Livetime

The task of the trigger was to provide a fast and efficient selection of cosmic ray particles traversing the detector such that they could be well measured. The primary AMS trigger [83] was a four-fold coincidence of at least one counter in each hodoscope. Next, combinations of the paddles incompatible with the Silicon Tracker geometry or triggers with signals in the veto counters were excluded.

More precisely the trigger proceeded in three subsequent stages called: Fast, Level-1 and Level-3 triggers. The Fast trigger required at least one signal from one PM on each of the four TOF planes, implementing an AND logic of the four signals resulting from the OR logic of the two ends of each paddles in each plane. The Fast trigger logic signal was fed into the detector electronics to start the data acquisition.

Events passing the Fast trigger were processed by the Level-1 trigger which

consisted in two requirements: no signal in the AntiCoincidence counters (Anti trigger) and compatibility with the Silicon Tracker sensitive area (Matrix trigger). This allowed to reject cosmic ray particles traversing the detector outside the Silicon Tracker acceptance and particles produced in interactions with the detector material.

Good events were processed by the Level-3 trigger which consisted in more refined selections of the TOF (TOF Level-3) and of the Silicon Tracker (Tracker Level-3) signals.

The TOF Level-3 trigger required a signal on both ends of one or two adjacent scintillators on the upmost (plane 1) and on the downmost (plane 4) hodoscopes⁶. A straight fiducial road, 6 cm wide, connecting the hits in planes 1 and 4 is then considered in the bending direction. If hits were present also in planes 2 and 3 the same procedure was applied to the orthogonal direction.

The Tracker Level-3 trigger selected tracker clusters inside the TOF fiducial road for which the strip with the highest signal had a signal-to-noise ratio greater than 4. The event was retained if at least three clusters on three different Tracker planes met the above condition. Before the Mir rendez-vous period a pattern recognition algorithm was applied to reject low momentum $+1 \leq Z < +3$ particles. Due to lower than expected trigger rates this additional condition was removed when the Shuttle docked to the space station.

The overall acceptance with the trigger constraints was $0.42 \text{ m}^2\text{sr}$. The trigger rate varied between 100 Hz and 700 Hz [84] depending on the position of the Shut-

⁶During the flight this additional condition was not applied to plane 4 since it delivered unreliable information.

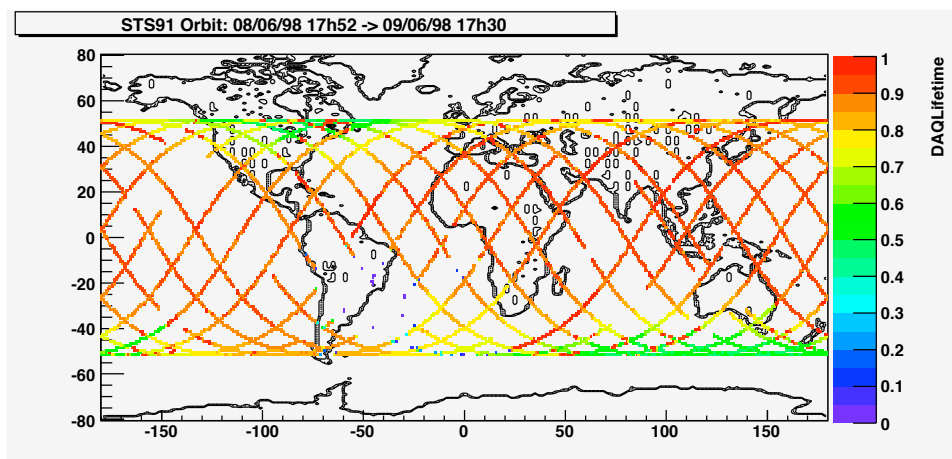


Figure 2.11: AMS-01 DAQ lifetime during the Zenith pointing period after the Shuttle had undocked from Mir (June 8th 17:53 UT to June 9th 17:42 UT). Note the loss of data taking capability in the South Atlantic Anomaly region.

tle with respect to the Earth magnetic poles. During the whole mission about 100 million triggers were recorded and written locally to disk. An online down-link had been foreseen, but only 10% of the data were actually transmitted to ground due to a failure in the high rate data link transmission. Nevertheless this small percentage of data allowed the online monitoring of the detector performance.

The Data Acquisition (DAQ) system consisted of several steps, including the collection of the digitized signals from each subdetector, event building, data buffering, disk storage and down-link. The total readout dead time was about $85 \mu\text{s}$ resulting in roughly 13% losses at the highest counting rates. In the South Atlantic Anomaly (SAA) region the rate precluded effective data taking.

2.3 Event Reconstruction

The purpose of the AMS-01 experiment was to identify cosmic ray particles and to measure their momentum. A particle can be identified when its mass and signed charge are known. In the AMS-01 detector these quantities are determined by the measured velocity, rigidity and energy deposit in the detector material.

2.3.1 Velocity Reconstruction

Each TOF cluster provided an absolute time of transit measurement t^i as defined in equation (2.1)⁷. The difference between the time measurements on the two sides of a counter, t_1 and t_2 , were used to find the particle impact point coordinate along the paddle. Time measurements were corrected on a per paddle basis for time slewing due to variations in pulse heights from the PMs, variations in cable lengths and incident angle. A linear χ^2 fit was then performed to the corrected absolute time of transit values, t^i , to find the particle inverse velocity β^{-1} according to the following relation:

$$t^i = \beta^{-1} \frac{d^i}{c} + K, \quad (2.5)$$

where K is the time slewing correction and d^i is the particle track length at its crossing point with the paddle derived from both the TOF and the Silicon Tracker information.

2.3.2 Track Reconstruction

Tracker clusters, resulting from the TDR online clustering, were used to generate three-dimensional hits by combining the center-of-gravities of all possible p-side and n-side clusters. The n-side had a 6 to 8 fold position degeneracy due to the readout scheme. This degeneracy was resolved by comparing clusters in the outer and inner tracker planes that had relative offsets between the silicon sensors and by using the rough track determined from the TOF data. Resolving the degeneracy

⁷The index i runs on the number of TOF clusters.

is not crucial for rigidity determination, since it is in the non-bending plane. In fact, good p-side clusters could even lack one or more n-side clusters due to the high noise level on the n-side. If this was the case, the reconstruction software attempted to generate missing n-side clusters using the information coming from the other tracker planes and from the TOF.

A straight line fit⁸ through all possible combinations of tracker hits on different tracker layers was performed. Hits to be used in the subsequent helical fit were selected according to the χ^2 value of the fit⁹. The helical fit assumed a spatially constant magnetic field equal to the average field. If the χ^2 from the helical fit was acceptable, the track hits were passed to the more sophisticated and computationally consuming track fitting algorithms.

Since the reliable determination of particle charge sign and rigidity is crucial, two different track reconstruction algorithms were used: a Fast Fit algorithm based on a 5×5 matrix inversion and the CERN GEANE [85] tracking algorithm.

The Fast Fit algorithm iteratively minimized a χ^2 between actual hits and hits reconstructed from a particle numerically propagated in the inhomogeneous magnetic field of the detector starting from a set of initial conditions $(x_0, y_0, \theta_0, \phi_0, 1/R)$, where x_0 and y_0 are the hit coordinates in the first tracker plane, θ_0 and ϕ_0 are the incident angles relative to the first tracker plane and $1/R$ is the inverse rigidity which is kept constant. The fit was performed twice, with and without including in the error estimation multiple scattering occurring in the tracker material. Disagreement between the two fits could indicate events which suffered large angle scattering.

The CERN GEANE tracking algorithm was used to calculate the particle trajectory, the transport matrix and the error covariance matrix. The tracks were propagated in the inhomogeneous magnetic field of the detector with the GEANT3 [86] detector simulator that included relevant physical processes. The track quality was evaluated with a Kalman Filter [87].

The GEANE Fit provided a better estimate of the actual particle trajectory, while the Fast Fit algorithm was faster and had the best performance for high momentum particles. The rigidity resulting from the Fast Fit was used together with the velocity to determine the particle mass.

2.3.3 Charge Reconstruction

The particle absolute charge, $|Z|$, was determined by a likelihood method based on the truncated mean of the energy deposited by the particle. Only the TOF clusters and the n- and p-side tracker clusters previously used for the velocity and for the

⁸A charged particle in a homogeneous magnetic field has a helical trajectory, where the radius of the helix is proportional to the momentum of the particle. The largest sagitta for particle trajectories in the AMS-01 spectrometer was on the order of a few centimeters, hence the track could be roughly approximated as a straight line.

⁹A maximum predetermined threshold is required for the χ^2 value, and then the fit with the lowest χ^2 is chosen.

track reconstruction, respectively, entered the calculation. The truncated mean was defined as the average energy deposit per cluster, excluding the contribution from the cluster with the highest energy deposit in order to reduce the effect of Landau fluctuations. The charge likelihood method took into account also the particle measured velocity. The resulting truncated mean value was corrected for particle pathlength through the detector material. The dependence of energy deposit on Z and the effects of changing pathlengths through the detector material were studied post-flight using data collected at an ion testbeam at GSI (Darmstadt) in September and October 1998.

Figures 2.14, 2.13 and 2.12 show the AMS-01 cosmic ray flux measurements in comparison with results obtained from other detectors.

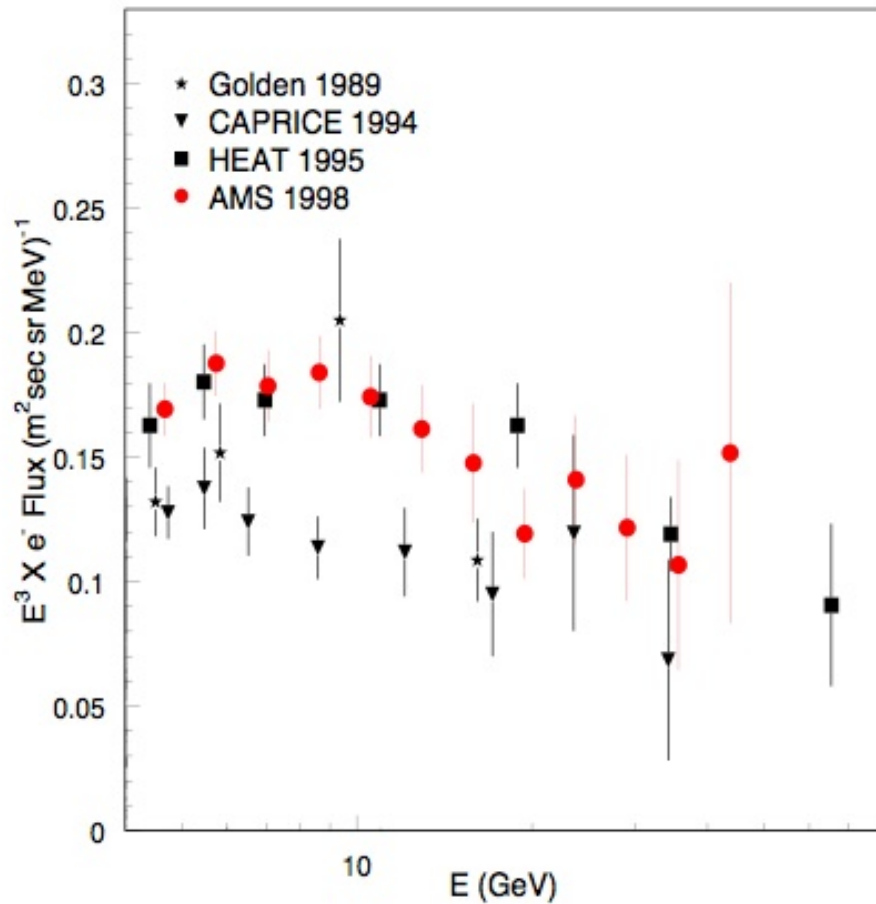


Figure 2.12: AMS-01 measurement of the kinetic energy electron flux compared to results from other detectors. From Ref [88].

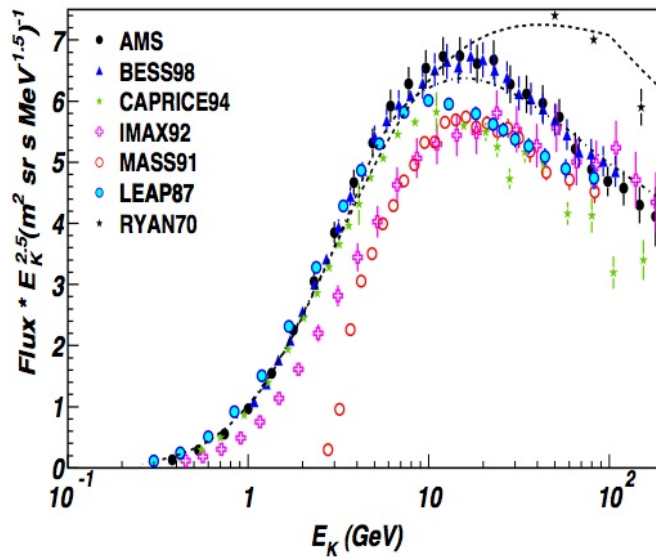


Figure 2.13: AMS-01 measurement of the kinetic energy proton flux compared to results from other detectors. From Ref [89].

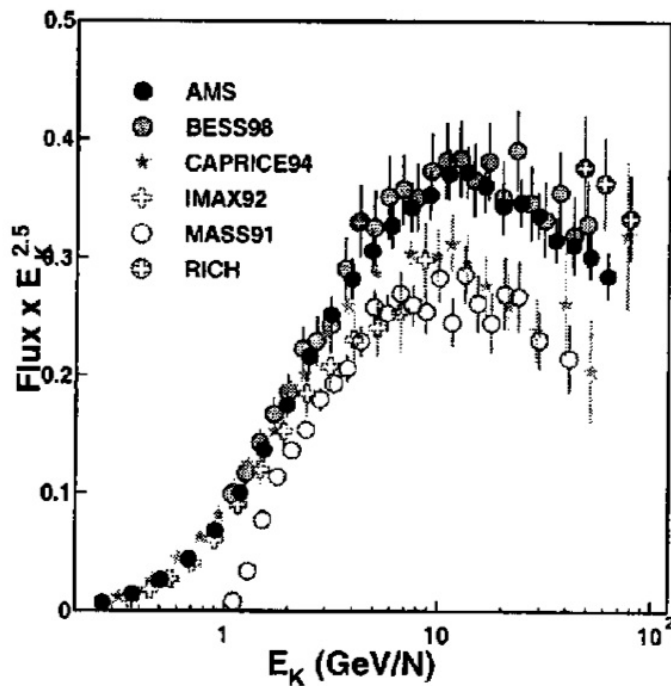


Figure 2.14: Helium nuclei kinetic energy flux in $(\text{m}^2 \text{sr s MeV/n})^{-1}$ units as measured by the AMS-01 detector. Also shown are the measurements obtained from other detectors. From Ref [89].

Chapter 3

Data analysis

To establish systematic variations in cosmic ray flux, the nominal flux has to be measured first. This has been done in two steps. First the global flux for electrons, protons and He nuclei has been measured and compared to previous AMS-01 measurements, in order to validate the measurement method. And then the average flux and spectrum as a function of geomagnetic coordinates has been measured. This average is used as a nominal flux at each geomagnetic location. Then the actual flux in short time intervals has been compared to the nominal flux to search for systematic fluctuations that are unlikely to be of statistical origin. Finally systematic fluctuation frequencies for both flux increases and decreases have been compared to the geomagnetic activity conditions at that time.

3.1 Event selection

The sets of selection criteria for electron, proton and He nuclei have been chosen to maximize the acceptance in the entire rigidity range accessible to the detector, i.e. between 0.1 and $\mathcal{O}(100)$ GV, minimizing background contaminations, which arise from particle misidentifications. The choice has also been based on previous analysis of the AMS-01 data measuring the spectra of electrons, protons and He nuclei [21, 25, 77, 78].

3.1.1 MonteCarlo samples

The response of the detector has been simulated using the AMS-01 detector simulation program, based on the GEANT3 [86] package. The effect of energy loss, multiple scattering, interactions, decays and the measured detector efficiency and resolution were included. Although a simulated AMS-01 trigger chain was included, additional geometrical constraints have to be applied when processing the MonteCarlo event samples. Corrections for additional trigger inefficiencies have to be made to the estimated detector performance from the data.

MonteCarlo (MC) particles were generated with a momentum distribution uniform in $\log_{10} p$, as single particles originating from a 3.9^2 m^2 plane placed on top of the detector¹. A summary of MC samples analysed for this work is presented in Table (3.1). MonteCarlo events, after passing pre-trigger requirements consisting in geometrical cuts embedded in the simulation software, are registered on disk and ready for user-defined selections.

Particle	Momentum range [GeV]	Generated Events	Pre-triggered Events
e^-	$0.1 \leq p < 1$	5×10^6	35×10^3
	$1 \leq p < 60$	90×10^6	4000×10^3
p	$0.450 \leq p < 6$	200×10^6	1500×10^3
	$6 \leq p < 150$	800×10^6	6000×10^3
He^3	$1 \leq p < 200$	100×10^6	600×10^3
He^4	$1 \leq p < 200$	500×10^6	3000×10^3

Table 3.1: Electron, proton and He nuclei MonteCarlo samples. The two MC samples for electrons and protons at different momentum range are due to the fact that the AMS-01 MonteCarlo samples available at the start of the present study did not include the lower energy particles, which then had to be simulated separately.

3.1.2 Selection criteria

MonteCarlo reconstructed events have been submitted to a first preselection, which takes into account the geometric acceptance of the detector and the trigger efficiency, and to minimal selection requirements assuring a good quality of the reconstructed event:

Preselection criteria:

- Trigger requirements² passed:

¹For the present work only downward going particles are of interest.

²see Section 2.2.2 and Ref. [83]

- LVL1:
 - * Anti trigger: no trigger signal from the veto counter,
 - * Fast Trigger: TOF correlations between planes 1 and 4;
- LVL3TOF;
- LVL3Tracker;
- No reconstructed clusters in the Anticoincidence counter;
- At least one reconstructed track in the Silicon Tracker;
- At least one reconstructed track in the Time Of Flight;
- Particle incoming direction within 40° with respect to the AMS Z-axis.

Selection criteria:

- Equality between charge measurements in the Tracker and in the TOF;
- At least 3 hit TOF planes;
- Rigidity measured better than 40%;
- Consistency among the measured momentum, velocity and charge³:

$$\left| \frac{R^2}{m^2} \left(\frac{1}{\beta^2} - 1 \right) - \left(\frac{1}{Ze} \right)^2 \right| < 3\sigma. \quad (3.1)$$

Then a set of selection criteria has been defined for each particle type as follows:

Electron selection:

- Negative rigidity;
- Charge equal to -1 ;
- Isolated track;
- Ultrarelativistic β .

Backgrounds in the electron sample arise from protons with wrongly measured momentum and secondary pions produced in the detector material incorrectly identified as electrons. These background particles are removed requiring ultrarelativistic particles with an isolated track, reducing the electron sample contamination to a level of 10^{-4} [25].

Proton selection:

- Positive rigidity;
- Charge equal to $+1$;
- Reconstructed mass within 3.5σ from the proton mass.

³Note that the relation $p = m\gamma\beta$ can be expressed as $\frac{1}{\beta^2} = 1 + \left(\frac{m}{Ze}\right)^2 \frac{1}{R^2}$.

As protons and He nuclei are the dominant components in cosmic rays, after selecting $Z = +1$ particles the proton sample has only minor backgrounds which consists of charged pions produced in the detector material and deuterons. The estimated fraction of secondary pions produced in the top of the AMS-01 detector is 1% below 0.5 GeV. The deuteron abundance in cosmic rays above the geomagnetic cutoff is 2%. The main sources of background to the proton sample are then low energy deuterons and pions wrongly reconstructed as protons, which are removed by the mass selection criterion. As seen in previous studies [77] this reduced the background contamination to negligible levels over all energies.

He nuclei selection:

- Positive rigidity;
- Charge equal to +2;
- $\beta^4 \cdot \chi_{MS_{off}}^2 < 200$.

The last selection criterion⁴ rejects events with poor track quality. The main potential source of background to the He sample is protons with wrongly measured charge. Comparing the two independent charge measurements from the Silicon Tracker and the TOF, this contamination can be reduced to 10^{-4} over all energies [78]. By adding the last selection criterion, protons which suffered large angle scatter in the Silicon Tracker such that they are misidentified as a He nucleus are further rejected [90].

The same preselection and selection criteria are applied to the data in addition to the following requirements:

- Single particle event;
- Downward going particle;
- DAQ lifetime greater than 0.25.

In addition events collected inside the South Atlantic Anomaly (SAA) are excluded. The SAA exclusion region is defined by the following geographic coordinates:

$$\begin{cases} 85^\circ \text{ W} < \text{Longitude} < 25^\circ \text{ E} \\ 0^\circ < \text{Latitude} < 55^\circ \text{ S} \end{cases}$$

where 0° longitude corresponds to the Greenwich meridian (Figure 3.18). Also events taken when the Earth was inside the field of view of the detector are excluded. This last requirement cut away all events collected when the AMS Z-axis was pointing toward the Nadir.

The action of selection criteria on MonteCarlo and data samples is summarized in Table (3.2). The data sample considered in the following belongs to events taken with the AMS Z-axis pointing to the Zenith.

⁴ $\chi_{MS_{off}}^2$ is the chi square resulting from the Fast fit algorithm without including multiple scattering effects in the tracker material.

	MonteCarlo Electrons		DATA
	(0.1; 1) GeV	(1; 60) GeV	Z=-1
$Z_{\text{Tracker}} = Z_{\text{TOF}}$	100.0%	99.9%	68.2%
At least 3 hit TOF planes	98.9%	99.8%	75.4%
$\sigma(1/R) < 0.4$	99.5%	99.9%	69.5%
p/ β Z compatibility	99.7%	99.7%	68.1%
Ultrarelativistic β	99.8%	99.6%	70.7%
Isolated track	85.3%	84.6%	80.8%
$N_{\text{selected}}/N_{\text{preselected}}$	82.3%	83.2%	67.9%

	MonteCarlo Protons		DATA
	(0.450; 6) GeV	(6; 150) GeV	Z=+1
$Z_{\text{Tracker}} = Z_{\text{TOF}}$	100.0%	99.9%	87.3%
At least 3 hit TOF planes	98.9%	99.6%	93.8%
$\sigma(1/R) < 0.4$	99.5%	100.0%	87.3%
p/ β Z compatibility	99.9%	99.6%	87.3%
Mass cut	96.5%	98.5%	92.1%
$N_{\text{selected}}/N_{\text{preselected}}$	91.6%	97.5%	87.2%

	MonteCarlo		DATA Z=+2	
	He ³	He ⁴	below cutoff	above cutoff
$Z_{\text{Tracker}} = Z_{\text{TOF}}$	98.6%	98.5%	92.5%	95.7%
At least 3 hit TOF planes	99.6%	99.3%	94.1%	97.7%
$\sigma(1/R) < 0.4$	99.9%	99.9%	91.3%	94.4%
p/ β Z compatibility	99.9%	99.9%	91.5%	94.6%
$\beta^4 \cdot \chi_{MSoff}^2 < 200$	95.1%	95.4%	94.5%	94.9%
$N_{\text{selected}}/N_{\text{preselected}}$	91.9%	91.4%	91.3%	94.4%

Table 3.2: Top panel: Electron selection. Middle panel: Proton selection. Bottom panel: He nuclei selection. For each selection criterion the percentage of events preselected respectively as $Z = -1$, $Z = +1$ and $Z = +2$ accepted by the ensemble of selection criteria except the quoted one is reported. The last line of each panel reports the percentage of events selected when applying all the cuts. The overall percentage of MonteCarlo particles passing all the selection criteria is 83.1% for the electron sample and 94.9% for the proton sample. From previous AMS-01 results on He nuclei [78], below the rigidity cutoff, $Z = +2$ particle spectrum composition is $(90\% \pm 5\%)He^3 + (10\% \pm 5\%)He^4$, while above cutoff, the sample consists of $(15\% \pm 5\%)He^3 + (85\% \pm 5\%)He^4$. Then results reported in the first and second column of the bottom panel should be compared respectively to those in the third and fourth column. The rigidity cutoff has been calculated as the maximal cutoff in a dipolar field approximation for the Shuttle trajectory with 1 second time sampling [91].

The percentage of data events preselected as $Z = -1$, $Z = +1$ and $Z = +2$ particles are found to be 2%, 85% and 12% respectively.

3.2 Electron, Proton and He nuclei flux measurements

In the present analysis the rigidity range accessible to the AMS-01 detector has been divided into seven large bins corresponding to the following kinetic energy ranges:

$$\begin{aligned}
0.1 < E_1 &\leq 0.3 \text{ GeV/n} \\
0.3 < E_2 &\leq 1 \text{ GeV/n} \\
1 < E_3 &\leq 3 \text{ GeV/n} \\
3 < E_4 &\leq 10 \text{ GeV/n} \\
10 < E_5 &\leq 30 \text{ GeV/n} \\
30 < E_6 &\leq 100 \text{ GeV/n} \\
100 < E_7 &\leq 200 \text{ GeV/n}
\end{aligned}$$

where n stands for the number of nucleons. The average incoming flux of particles of type $i = e^-, p, \text{He}^3, \text{He}^4$, in the kinetic energy bin E_k can be derived as follows⁵:

$$\bar{\Phi}_{(i)}^0(E_k)|_{\theta_{max}} = \frac{1}{2\pi(1 - \cos \theta_{max})} \sum_{\cos \theta=1}^{\cos \theta_{max}} \sum_{\phi=0}^{2\pi} \frac{N_{(i)}(E_k, \cos \theta, \phi)}{A_{(i)}(E_k, \cos \theta, \phi) \cdot T}, \quad (3.2)$$

where $N_{(i)}(E_k, \cos \theta, \phi)$ is the number of detected particles of type i , impinging on the detector with kinetic energy E_k and with incoming direction polar and azimuthal angles θ and ϕ . T is the measurement time interval, $A_{(i)}(E_k, \cos \theta, \phi)$ is the detector acceptance in surface units and θ_{max} is the maximum polar angle of the particle direction accepted.

Since in the present work the number of detected particles is integrated in direction angles over the region $\Delta\Omega = 2\pi(1 - \cos \theta_{max})$, equation (3.2) can be reexpressed as:

$$\begin{aligned}
\bar{\Phi}_{(i)}^0(E_k)|_{\theta_{max}} &= \frac{1}{2\pi(1 - \cos \theta_{max})} \cdot \frac{\mathbf{N}_{(i)}(E_k, \cos \theta_{max})}{A_{(i)}(E_k, \cos \theta_{max}) \cdot T} \\
&= \frac{\mathbf{N}_{(i)}(E_k, \cos \theta_{max})}{\mathbf{A}_{(i)}(E_k, \cos \theta_{max}) \cdot T}, \quad (3.3)
\end{aligned}$$

where $\mathbf{A}_{(i)}(E_k, \cos \theta_{max}) = 2\pi(1 - \cos \theta_{max}) \cdot A_{(i)}(E_k, \cos \theta_{max})$ is the acceptance in m^2sr and $\mathbf{N}_{(i)}(E_k, \cos \theta_{max})$ is the number of particles i detected in the kinetic energy bin E_k , integrated in $\cos \theta$ and ϕ over $\Delta\Omega$.

⁵For the sake of precision it should be reported that the number of particles and the acceptances were first derived as function of the rigidity, which is the quantity directly measured by the AMS-01 detector, and then the rigidity was translated into kinetic energy according to the relation: $E_K = (Z \cdot R \cdot \beta)/(1 + \sqrt{1 - \beta^2})$.

3.2.1 Acceptance estimation

The detector acceptance $\mathbf{A}_{(i)}(E_k, \cos \theta_{max})$ can be derived from the MonteCarlo samples as follows:

$$\mathbf{A}_{(i)}(E_k, \cos \theta_{max}) = S \cdot \Omega \cdot \frac{N_{ii}^{MC}(E_k, \cos \theta_{max})}{\mathcal{N}_i^{MC}(E_k)}, \quad (3.4)$$

where $N_{ii}^{MC}(E_k, \cos \theta_{max})$ is the number of MC particles reconstructed as type i from the generated particle sample of type i , $\mathcal{N}_i^{MC}(E_k)$, in the kinetic energy bin E_k with maximum incoming direction polar angle θ_{max} , and

$$S \cdot \Omega = 3.9^2 \cdot 2\pi \text{ m}^2\text{sr} \quad (3.5)$$

is the total generating phase space.

The acceptance has to be corrected for the smearing due to the finite rigidity resolution of the detector. The rigidity smearing matrices for electrons, protons and He nuclei have been evaluated using the MonteCarlo samples (Figures 3.1, 3.2 and 3.3). The migration matrices are symmetric for proton and helium nuclei and off-diagonal elements are not very large due to the fact that the bin width is large compared to the momentum resolution. For electrons, the migration matrix has a tail due to effects of bremsstrahlung.

A Bayesian unfolding method [92], AMSUnfold [93], has been applied to the MC reconstructed rigidity distributions in order to get the number of detected particles corrected for smearing. The input to the unfolding algorithm are the reconstructed distribution, $N_{obs}(E_k)$, the migration matrix, $M(E_k, E_h)$, and the background distribution, $N_{backg}(E_k)$, which consists of reconstructed events whose counterpart has been generated outside the detector acceptance. The smearing corrected distribution, $N_{corr}(E_h)$, is obtained through an iterative procedure. At the n -th step:

$$N_{corr}^n(E_h) = \sum_k (N_{obs}(E_k) - N_{backg}(E_k)) \cdot \frac{P(E_k|E_h)}{\epsilon(E_h)} \quad (3.6)$$

where $\epsilon(E_h)$ is the detection efficiency in bin E_h and $P(E_k|E_h)$ is the probability that an event originally generated in the bin E_h is reconstructed in the bin E_k . The latter quantity is evaluated from the migration matrix as:

$$P(E_k|E_h) = \frac{m(E_k, E_h)}{\sum_l m(E_k, E_l) \cdot \hat{N}_{corr}^{n-1}(E_l)} \cdot \hat{N}_{corr}^{n-1}(E_h) \quad (3.7)$$

where $m(E_k, E_h)$ and $\hat{N}_{corr}^{n-1}(E_h)$ are the migration matrix and smearing corrected distribution at the step $(n - 1)$ respectively, both normalized to unity. At the first step of the iteration procedure a flat distribution is taken for $\hat{N}_{corr}^0(E_h)$.

The detection inefficiency, $(1 - \epsilon(E_h))$, is estimated from the MonteCarlo as the fraction of generated events that, though inside the detector acceptance and satisfying single particle and trigger cuts, have not been reconstructed. These events are filled in the migration matrix under(over)flow, as prescribed by the algorithm.

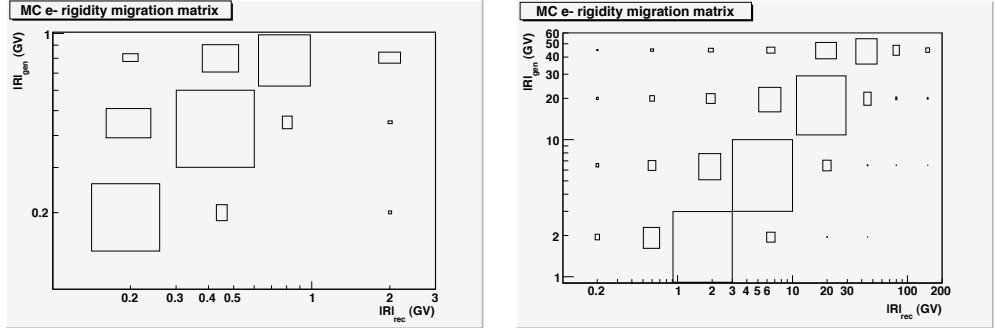


Figure 3.1: Electron smearing matrices.

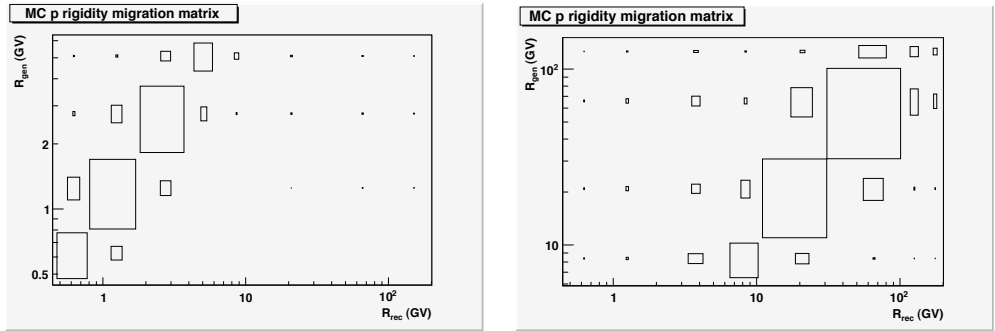


Figure 3.2: Proton smearing matrices.

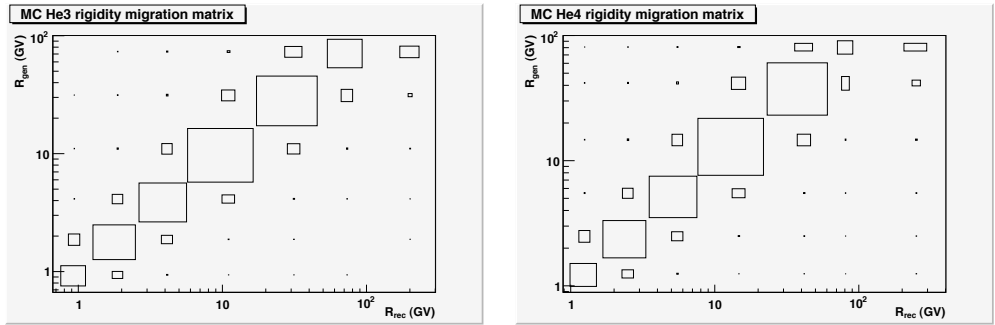


Figure 3.3: He nuclei smearing matrices.

At each step of the iteration the corrected distribution obtained is compared to a test distribution:

$$N_{test}(E_h) = \sum_k m(E_k, E_h) \cdot \sum_k (N_{obs}(E_k) - N_{backg}(E_k)). \quad (3.8)$$

The iterative procedure stops when the resulting χ^2 , defined as:

$$\chi^2 = \sum_h \frac{(N_{test}(E_h) - N_{corr}^n(E_h))^2}{\sigma_{N_{corr}^n(E_h)}^2} \quad (3.9)$$

is below a fixed value. The uncertainties on the smearing corrected distribution are calculated from the observed distribution and the unfolding matrix, thus taking into account the bin-to-bin correlation produced by the smearing effect.

Since the unfolding algorithm only reproduces the shape of the generated distribution, the output unfolded distribution has then to be normalized such that its integral is equal to the integral of the reconstructed distribution after background subtraction.

The normalized unfolded kinetic energy distributions for electrons, protons and He nuclei are shown in Figures 3.4, 3.5 and 3.6, superposed to the respective generated and reconstructed kinetic energy distributions. Since the kinetic energy bins chosen are rather wide smearing effects are barely appreciable.

Further overall corrections to the acceptance have to be done to take into account that the MonteCarlo generally overestimates the efficiencies of the various subdetectors and of the triggers introducing systematic errors to the flux measurements. Table (3.3) gives a list of the above mentioned corrections and of the related systematic errors. Trigger, fitting and particle interaction⁶ corrections have been evaluated from unbiased trigger flight data in previous AMS-01 analysis [25, 77, 78, 94, 95]. The selection corrections are estimated comparing data and MonteCarlo selected event percentages reported in Table (3.2).

The smearing corrected number of detected particles are used for the bin per bin acceptance evaluation according to equation (3.4), then the corrections quoted in Table 3.3 are applied to the obtained values.

When estimating the acceptance for the MonteCarlo low energy electron sample, the generated absolute rigidity range has been divided into three bins with edges:

$$|R_h| = 0.1; 0.3; 0.6; 1 \text{ GV} \quad h = 1, \dots, 4.$$

Afterwards the acceptance value in the bin 0.3; 1 GV has been obtained as the weighted mean of the second and third bin values:

$$\mathbf{A}_{(e)}(R_2; R_4) = \frac{\mathbf{A}_{(e)}(R_2; R_3) \cdot \log_{10}(R_3/R_2) + \mathbf{A}_{(e)}(R_3; R_4) \cdot \log_{10}(R_4/R_3)}{\log_{10}(R_4/R_2)}$$

where the weight takes into account the logarithmic shape of the rigidity distribution. The same method has been applied to the MonteCarlo proton samples to combine the acceptance results in the last bin of the low rigidity sample, $3 \leq R < 6$ GV, and the first bin of the high rigidity sample, $6 \leq R < 10$ GV, into an acceptance value in the rigidity range $3 \leq R < 10$ GV.

⁶This is a correction to the MonteCarlo simulated particle interactions in the detector material.

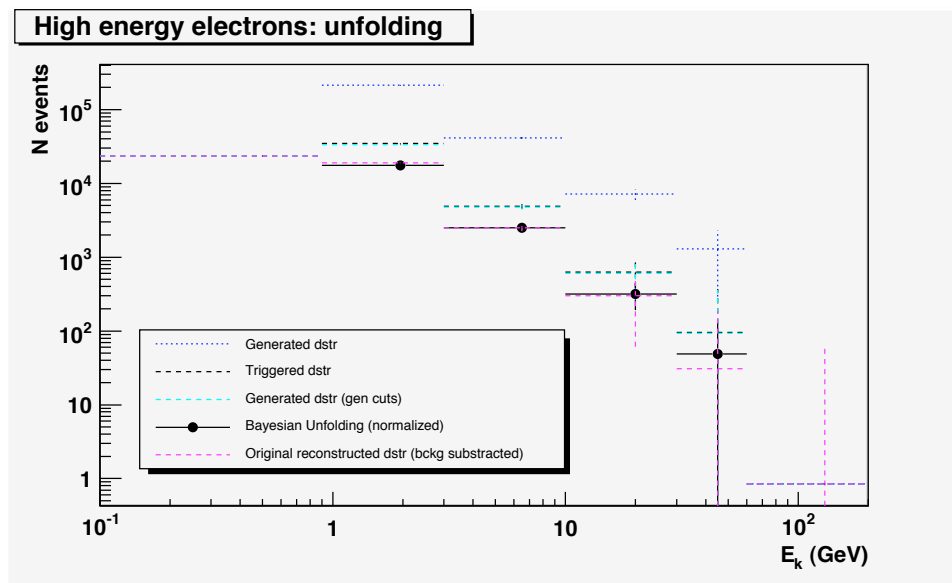
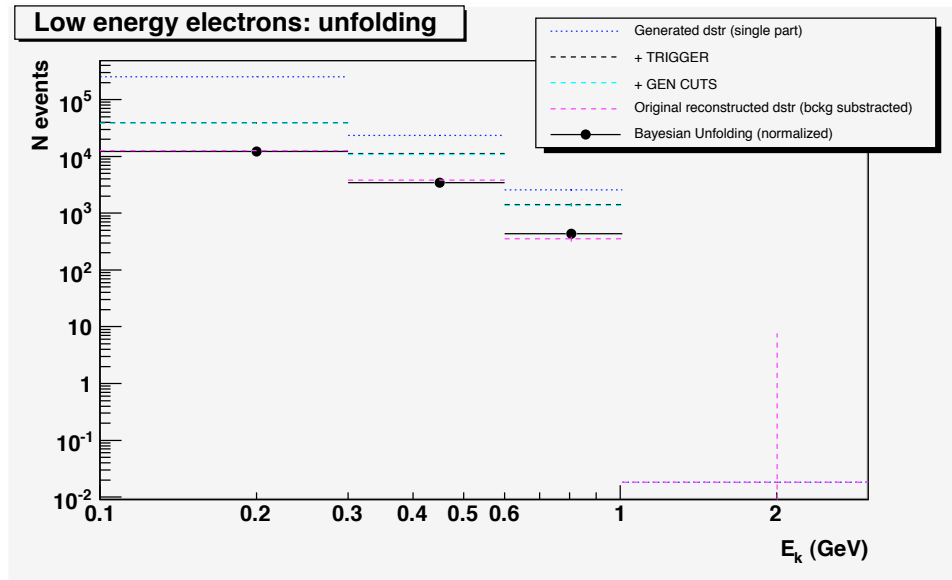


Figure 3.4: Unfolded kinetic energy distribution for the low (top panel) and high (bottom panel) energy electron MonteCarlo samples, superposed to the generated and reconstructed distributions. The latter has been corrected for background. Also the generated distributions after applying trigger (triggered dstr), single particle and geometrical cuts (generated dstr (gen cuts)) are shown.

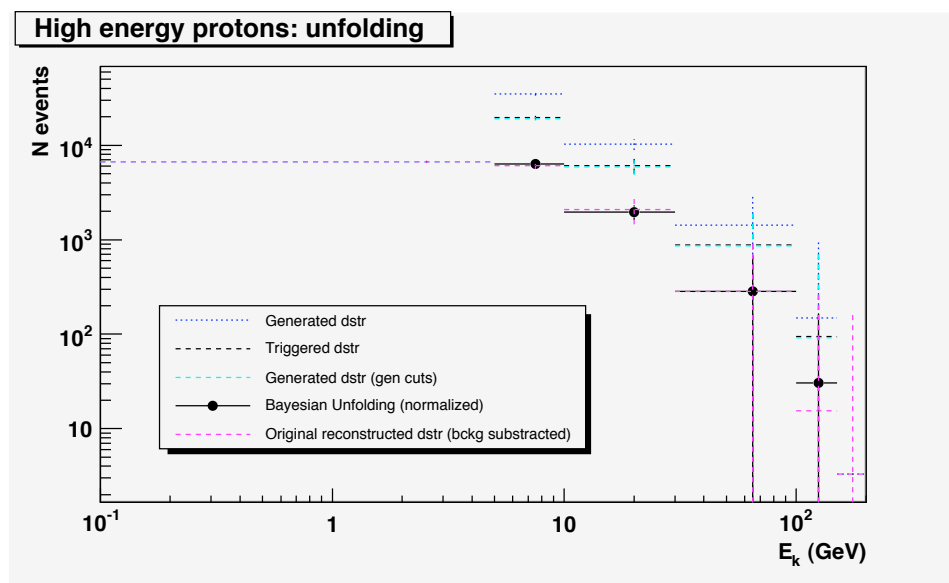
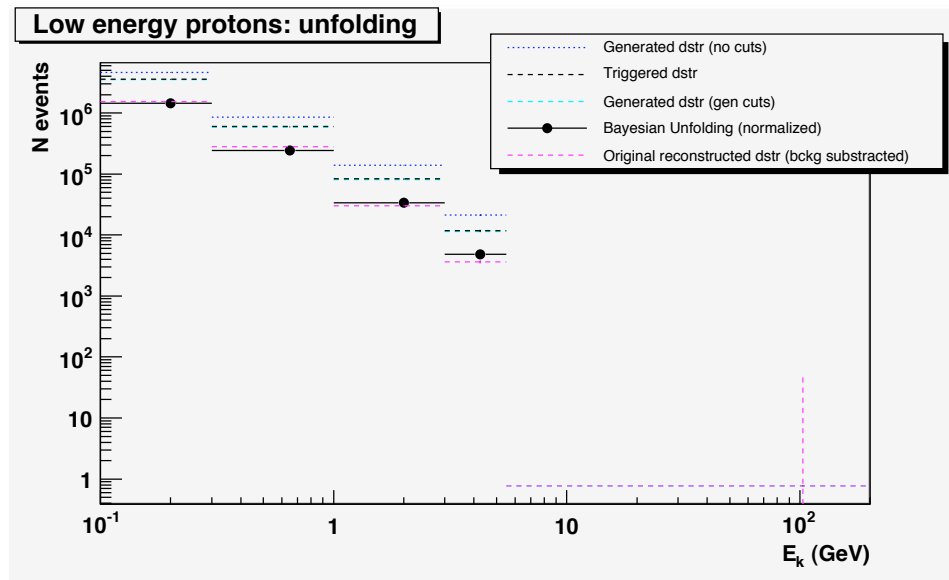


Figure 3.5: Unfolded kinetic energy distribution for the low (top panel) and high (bottom panel) energy proton MonteCarlo samples, superposed to the generated and reconstructed distributions. The latter has been corrected for background. Also the generated distributions after applying trigger (triggered dstr), single particle and geometrical cuts (generated dstr (gen cuts)) are shown.

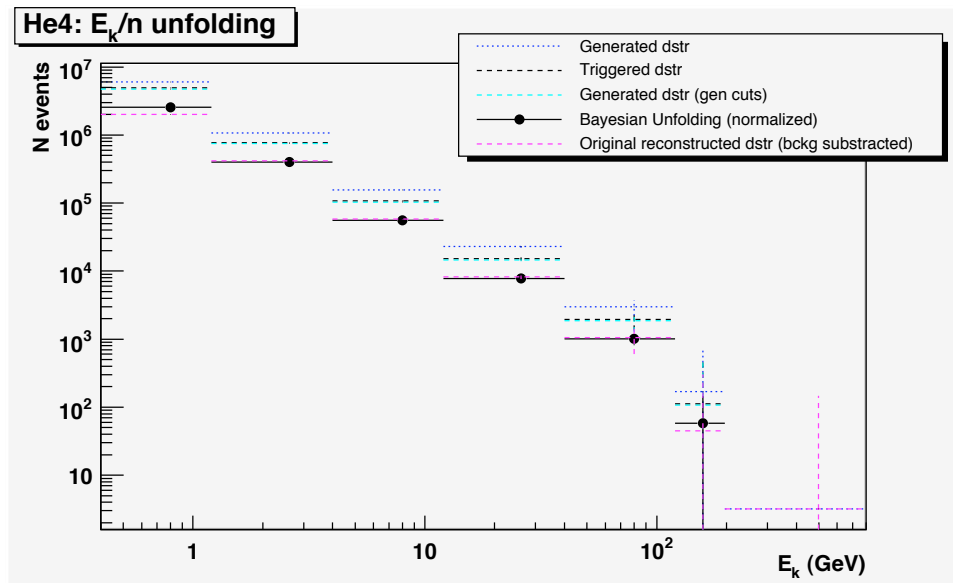
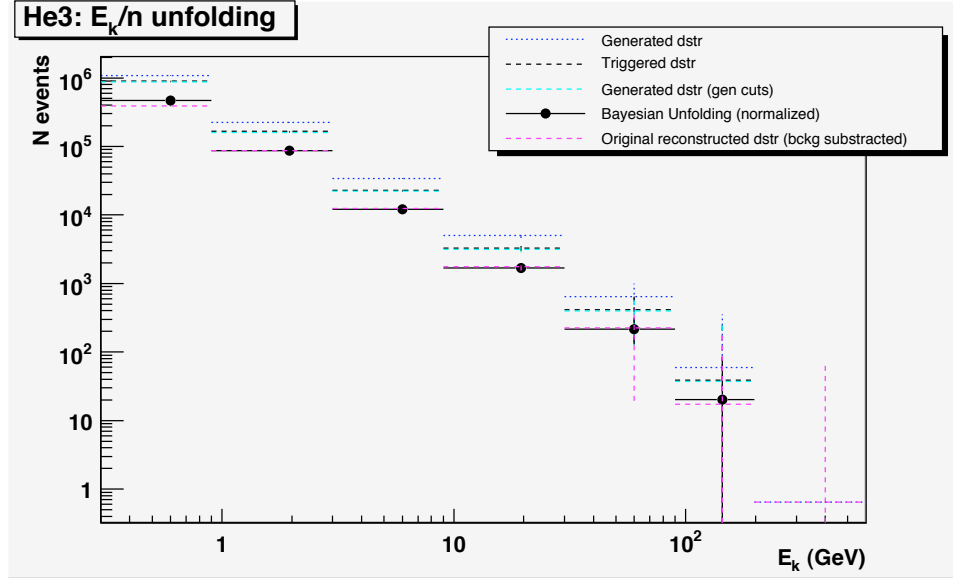


Figure 3.6: Unfolded kinetic energy distribution for the He^3 (top panel) and He^4 (bottom panel) MonteCarlo samples, superposed to the generated and reconstructed distributions. The latter has been corrected for background. Also the generated distributions after applying trigger (triggered dstr), single particle and geometrical cuts (generated dstr (gen cuts)) are shown.

Acceptance Correction	Value (%)				Error (%)
	electrons	protons	He ³	He ⁴	
Fast Trigger	-3	-3	-3	-3	1.5
Anti Trigger	0	0	0	0	1
Level3 TOF	-4	-4	0	0	2
Level3 Tracker	-2	-2	-2	-2	1
Track fit	-2	-2	-2	-2	1
β fit	-3	-3	-3	-3	1
Particle interactions	+1	+1	+1	+1	1.5
MC statistics	0	0	0	0	2
Acceptance θ, ϕ	0	0	0	0	2
Electron selection	-15	–	–	–	1
Proton selection	–	-8	–	–	2 (3) high (low) p
He ³ selection	–	–	-1	–	1
He ⁴ selection	–	–	–	+3	1
Total correction	-28	-21	-10	-6	5 (6 for low p protons)

Table 3.3: Overall corrections and related systematic errors for electron, proton and He nuclei acceptances.

The corrected acceptance estimations for electrons, protons and He nuclei as a function of rigidity and kinetic energy are shown in Figures 3.7 and 3.8 respectively. Note that for ultrarelativistic electrons, as those considered in this work, the two graphs are specular. The results reproduce the acceptance values reported in previous AMS-01 studies [81, 90, 96].

3.2.2 Background estimation

If background contaminations are present the flux of equation (3.3) has to be corrected by subtracting the background flux $\bar{\Phi}_{(i)}^{bckg}(E_k)$, as follows:

$$\bar{\Phi}_{(i)}(E_k) = \bar{\Phi}_{(i)}^0(E_k) - \bar{\Phi}_{(i)}^{bckg}(E_k) \quad (3.10)$$

the index i runs as usual on particle type: e^- , p, He for what concerns this work. Since the background consists of misidentified particles we can express its flux as:

$$\bar{\Phi}_{(i)}^{bckg}(E_k) = \sum_{\substack{j=\text{He,D,p},\pi,e^- \\ j \neq i}} \sum_h b_i^j(E_k, E_h) \cdot \bar{\Phi}_{(j)}^0(E_h) \quad (3.11)$$

where $b_i^j(E_k, E_h)$ represents the contamination of type j particles to the flux of type i particles and can be evaluated from the MonteCarlo as:

$$b_i^j(E_k, E_h) = \frac{N_{ij}^{MC}(E_k, E_h)}{\mathcal{N}_j^{MC}(E_h)} \quad , \quad (3.12)$$

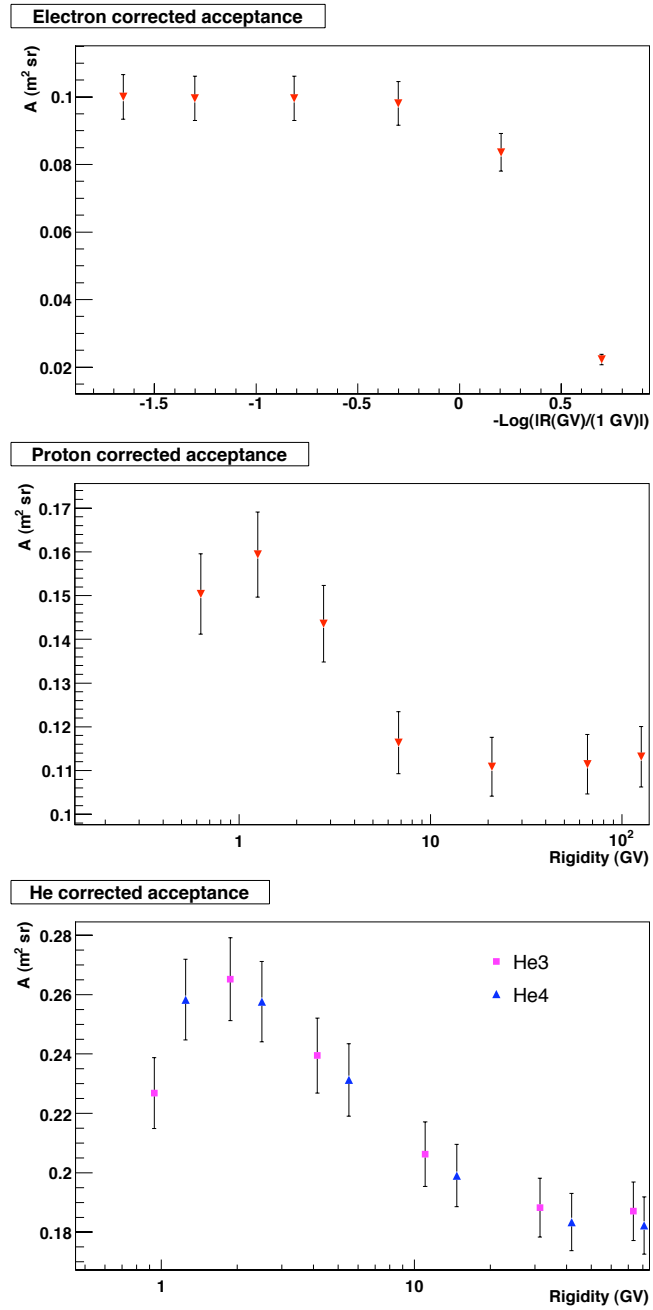


Figure 3.7: Electron, proton and He nuclei acceptances as a function of rigidity.

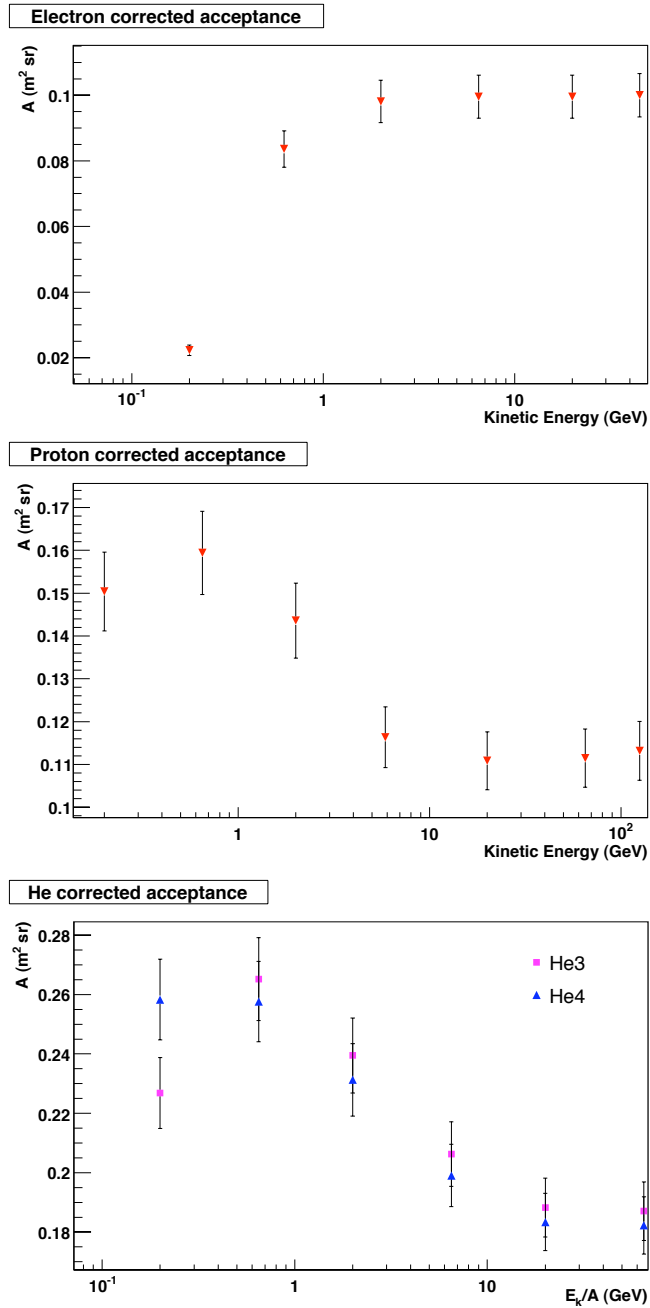


Figure 3.8: Acceptances as a function of kinetic energy for electrons and protons, and kinetic energy per nucleon for He³ and He⁴ nuclei.

where $N_{ij}^{MC}(E_k, E_h)$ is the number of particles reconstructed as type i with kinetic energy E_k originally generated as type j with kinetic energy E_h , and $N_j^{MC}(E_h)$ is the total number of type j particles generated in the kinetic energy bin E_h .

Assuming that background from pions and deuterons is already suppressed by the selection cuts, we can restrict the study to the mutual contaminations of electrons, protons and He only.

The background coefficients, $b_i^j(E_k, E_h)$, are obtained imposing the selection criteria for particles of type i to the MonteCarlo sample of type j particles.

Applying electron selection to the MonteCarlo proton and He nuclei samples the background coefficients for electrons have been computed; results are reported in Tables 3.4, 3.5 and 3.6. Proton and He nuclei contaminations to the electron sample are below 10^{-5} and 10^{-7} respectively over all energies.

Similarly proton selection has been applied to the MonteCarlo electron and He nuclei samples to estimate contaminations to proton. Background coefficients for protons are reported in Tables 3.7, 3.8 and 3.9. Electron and He nuclei contaminations to the proton sample are of the order of 10^{-6} over all energies.

Finally He selection criteria have been applied to MonteCarlo electron and proton samples. All background coefficients from misidentified protons have been found to be zero, while the only non zero coefficients from misidentified electrons are the following:

$$b_{\text{He}}^e(4 \leq E_k < 9 \text{ GeV}, 30 \leq E_h < 60 \text{ GeV}) = 0.047 \times 10^{-6}$$

$$b_{\text{He}}^e(40 \leq E_k < 90 \text{ GeV}, 10 \leq E_h < 30 \text{ GeV}) = 0.010 \times 10^{-6}$$

The contaminations to the He spectrum due to proton or electron misidentification are less than 10^{-7} over the entire energy range accessible to the AMS-01 detector.

3.2.3 Spectra

Data taken during the Zenith pointing period have been analysed to evaluate the differential spectra as a function of the incident kinetic energy for electrons, protons and as a function of the kinetic energy per nucleon for He nuclei, according to equation (3.3) in several geomagnetic latitude regions (Figure 3.18).

The differential spectra for downward going electrons as a function of the kinetic energy, for ten distinct geomagnetic latitude regions are shown in Figures 3.9, 3.10 and 3.11. Electron flux values are also reported in Tables 3.10 and 3.11. The results agree well with previous analyses of the AMS-01 data [21, 25].

Proton differential spectra obtained with the present work, $\bar{\Phi}_{(p)}^{40^\circ}(E_k)$, are shown together with previous AMS-01 proton flux measurements, $\bar{\Phi}_{(p)}^{32^\circ}(E_k)$ in Figures (3.12), (3.13) and (3.14). The two analysis differ for the set of selection criteria, in particular the polar angle is 40° for the present work and 32° for the one quoted [21, 77]. Furthermore the previous analysis makes use of a much finer energy binning with respect to the present one, explaining the discrepancy between

E_h (GeV)	E_k (GeV)						
	0.1; 0.3	0.3; 1	1; 3	3; 10	10; 30	30; 100	100; 200
0.1; 0.3	0	0	0	0	0	0	0
0.3; 1	0	0	0	0	0	0	0
1; 3	0	0.311	0.565	0.141	0.064	0.085	0.049
3; 10	0.003	0.753	1.278	0.452	0.305	0.085	0.121
10; 30	0.036	0.919	1.585	1.146	0.623	0.258	0.195
30; 100	0.051	1.115	1.912	1.347	1.037	0.558	3.180
100; 200	0.077	1.240	1.864	1.372	1.355	3.073	12.441

Table 3.4: Proton contamination coefficients to electrons: $b_e^p(E_k, E_h) \times 10^6$.

E_h (GeV)	E_k (GeV)						
	0.1; 0.3	0.3; 1	1; 3	3; 10	10; 30	30; 100	100; 200
0.3; 0.9	0	0	0	0	0	0	0
0.9; 3	0	0	0	0	0	0	0
3; 9	0	0.085	0.057	0	0	0	0
9; 30	0.044	0.022	0.066	0.022	0	0.022	0
30; 90	0.044	0.066	0.044	0.022	0	0	0
90; 198	0	0.030	0.030	0.030	0.060	0	0.030

Table 3.5: He³ contamination coefficients to electrons: $b_e^{\text{He}^3}(E_k, E_h) \times 10^6$.

E_h (GeV)	E_k (GeV)						
	0.1; 0.3	0.3; 1	1; 3	3; 10	10; 30	30; 100	100; 200
0.4; 1.2	0	0	0	0	0	0	0
1.2; 4	0	0.007	0	0	0	0	0
4; 12	0.018	0.053	0.018	0.012	0	0.006	0
12; 40	0.018	0.138	0.097	0.009	0.014	0.005	0
40; 120	0.005	0.060	0.056	0.023	0	0.009	0.014
120; 196	0.010	0.040	0.050	0.040	0.010	0.020	0.020

Table 3.6: He⁴ contamination coefficients to electrons: $b_e^{\text{He}^4}(E_k, E_h) \times 10^6$.

E_h (GeV)	E_k (GeV)						
	0.1; 0.3	0.3; 1	1; 3	3; 10	10; 30	30; 100	100; 200
0.1; 0.3	0	0	0	0	0	0	0
0.3; 1	0	0	0	0	0	0	0
1; 3	0.009	0.172	0.289	0.063	0	0	0
3; 10	0.036	1.056	2.004	0.569	0.596	0.163	0.036
10; 30	0.119	1.306	4.096	2.998	1.900	0.791	0.257
30; 60	0.125	1.411	5.786	4.500	3.701	3.669	1.788

Table 3.7: Electron contamination coefficients to protons: $b_p^e(E_k, E_h) \times 10^6$.

E_h (GeV)	E_k (GeV)						
	0.1; 0.3	0.3; 1	1; 3	3; 10	10; 30	30; 100	100; 200
0.3; 0.9	4.351	0.616	0	0	0	0	0
0.9; 3	1.830	4.623	0.372	0.310	0	0	0
3; 9	0.848	1.386	3.168	1.131	0	0.028	0.028
9; 30	0.352	0.198	0.505	2.702	0.945	0.022	0.022
30; 90	0.199	0.199	0.529	0.640	1.632	0.662	0.022
90; 198	0.030	0.209	0.358	0.238	0.507	1.609	0.238

Table 3.8: He³ contamination coefficients to protons: $b_p^{\text{He}^3}(E_k, E_h) \times 10^6$.

E_h (GeV)	E_k (GeV)						
	0.1; 0.3	0.3; 1	1; 3	3; 10	10; 30	30; 100	100; 200
0.4; 1.2	3.804	0.614	0	0	0	0	0
1.2; 4	2.348	4.098	0.299	0.007	0	0	0
4; 12	0.789	1.305	0.222	0.842	0.077	0	0
12; 40	0.359	0.240	0.599	1.451	0.949	0.106	0.014
40; 120	0.143	0.231	0.292	0.287	0.926	0.685	0.088
120; 196	0.121	0.131	0.211	0.251	0.231	0.863	0.201

Table 3.9: He⁴ contamination coefficients to protons: $b_p^{\text{He}^4}(E_k, E_h) \times 10^6$.

the two measurements in correspondence to the geomagnetic cutoff, where the spectra have a dip. Everywhere else the two analysis are in excellent agreement. The flux values obtained with the present analysis are reported in Tables 3.12 and 3.13.

The He nuclei spectrum has been derived combining the He³ and He⁴ spectra. First the $Z = +2$ particle spectra above and below the geomagnetic rigidity cutoff have been measured. Then, using previous AMS-01 results on the $Z = +2$ spectral composition [21, 78], the He³ and He⁴ counting number have been obtained as:

$$N_{(\text{He}^3)}(E_k) = 90\%N_{(Z=+2)}^{\text{below cutoff}}(E_k) + 15\%N_{(Z=+2)}^{\text{above cutoff}}(E_k) \quad (3.13)$$

$$N_{(\text{He}^4)}(E_k) = 10\%N_{(Z=+2)}^{\text{below cutoff}}(E_k) + 85\%N_{(Z=+2)}^{\text{above cutoff}}(E_k) \quad (3.14)$$

from which He³ and He⁴ spectra as function of the kinetic energy have been evaluated according to equation (3.3). The overall He nuclei spectrum as a function of kinetic energy per nucleon has been obtained as the sum of the He³ and He⁴ spectra:

$$\bar{\Phi}_{(\text{He})}(E_k/A) = \bar{\Phi}_{(\text{He}^3)}(E_k/A) + \bar{\Phi}_{(\text{He}^4)}(E_k/A). \quad (3.15)$$

The He nuclei differential spectra obtained in the distinct geomagnetic latitude regions are shown in Figures 3.15, 3.16 and 3.17, corresponding values are reported in Tables 3.14 and 3.15. Again the results are in excellent agreement with other analysis of the AMS-01 data [21, 78, 90].

Given the order of magnitude of electron, proton and He nuclei fluxes and of their mutual contamination coefficients the background corrections (3.10) are negligible.

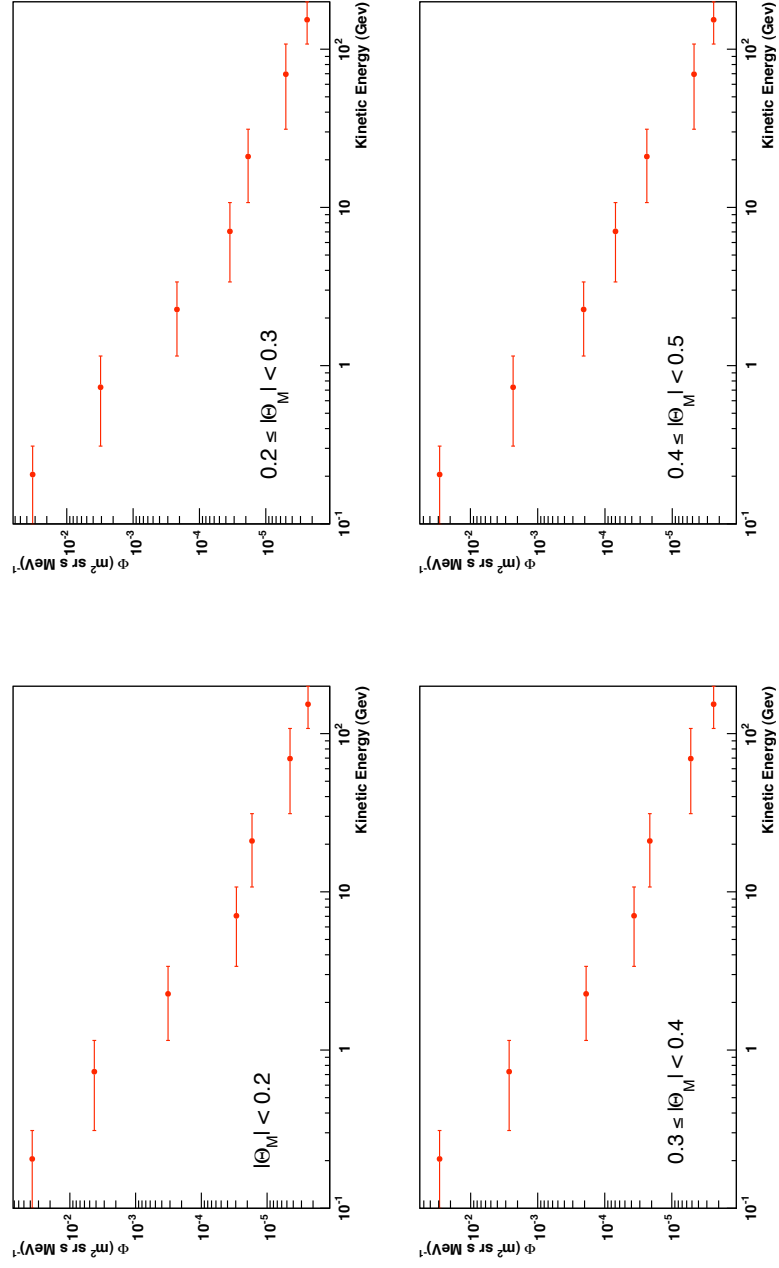


Figure 3.9: Electron differential spectra as a function of the incident kinetic energy for the geomagnetic latitude regions $|\Theta_M| < 0.2$ (top left), $0.2 \leq |\Theta_M| < 0.3$ (top right), $0.3 \leq |\Theta_M| < 0.4$ (bottom left) and $0.4 \leq |\Theta_M| < 0.5$ (bottom right).

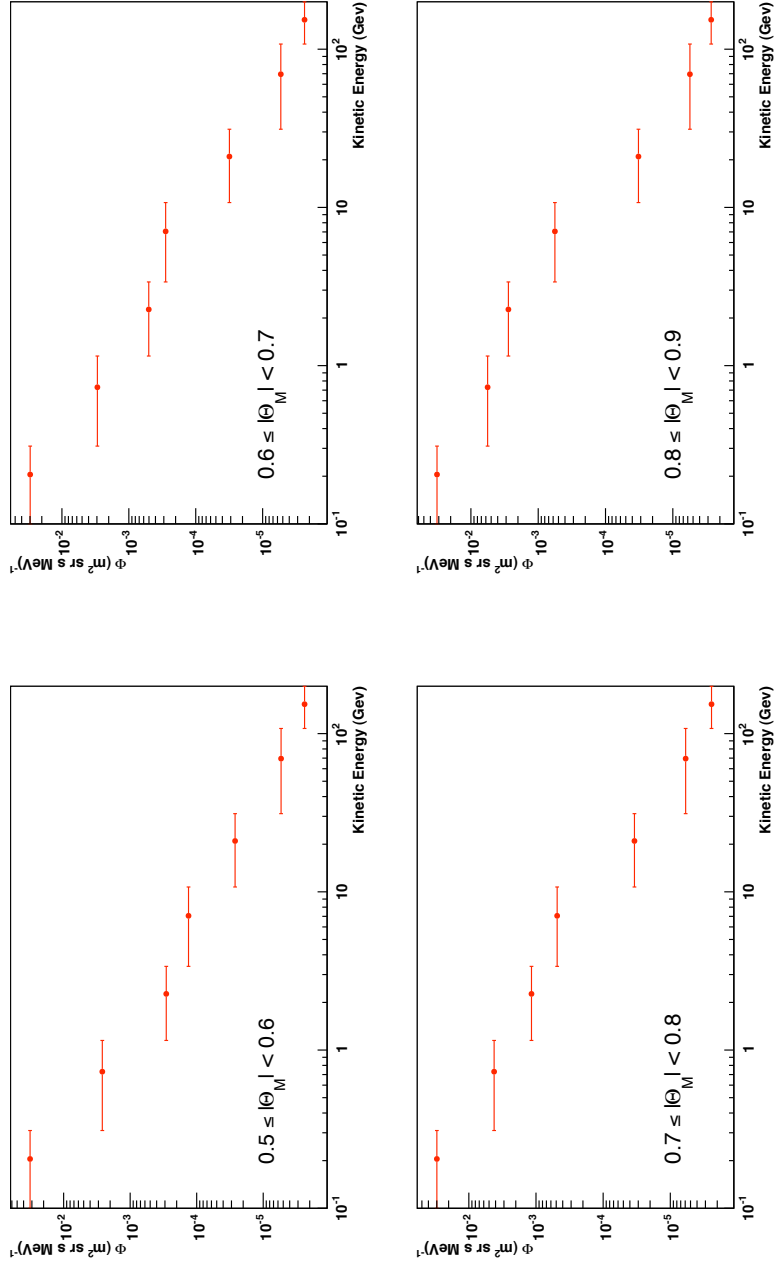


Figure 3.10: Electron differential spectra as a function of the incident kinetic energy for the geomagnetic latitude regions $0.5 \leq |\Theta_M| < 0.6$ (top left), $0.6 \leq |\Theta_M| < 0.7$ (top right), $0.7 \leq |\Theta_M| < 0.8$ (bottom left) and $0.8 \leq |\Theta_M| < 0.9$ (bottom right).

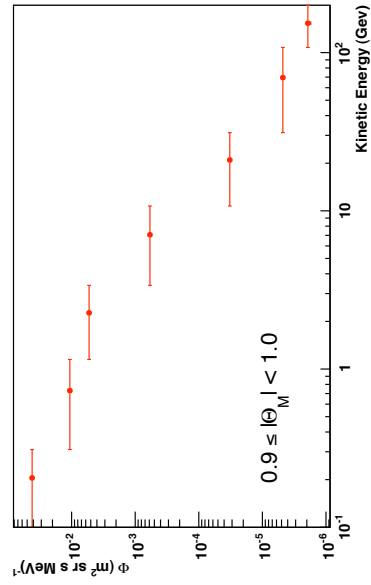
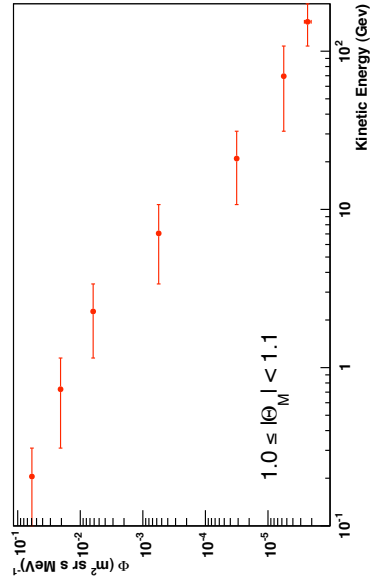


Figure 3.11: Electron differential spectra as a function of the incident kinetic energy for the geomagnetic latitude regions $0.9 \leq |\Theta_M| < 1.0$ (left) and $1.0 \leq |\Theta_M| < 1.1$ (right).

Table 3.10: Downward electron differential flux $\bar{\Phi}_{(e^-)}^{40^\circ}(E_k)$ ($\text{m}^2 \text{ sr s MeV}^{-1}$):

Kinetic Energy (GeV)	Geomagnetic Latitude (rad)					
	$ \Theta_M < 0.2$	$0.2 \leq \Theta_M < 0.3$	$0.3 \leq \Theta_M < 0.4$	$0.4 \leq \Theta_M < 0.5$	$0.5 \leq \Theta_M < 0.6$	
0.1; 0.3	$(3.7 \pm 0.1) \times 10^{-2}$	$(3.3 \pm 0.1) \times 10^{-2}$	$(2.9 \pm 0.1) \times 10^{-2}$	$(2.9 \pm 0.1) \times 10^{-2}$	$(3.2 \pm 0.1) \times 10^{-2}$	
0.3; 1	$(4.25 \pm 0.08) \times 10^{-3}$	$(3.09 \pm 0.09) \times 10^{-3}$	$(2.67 \pm 0.08) \times 10^{-3}$	$(2.32 \pm 0.07) \times 10^{-3}$	$(2.62 \pm 0.08) \times 10^{-3}$	
1; 3	$(3.2 \pm 0.1) \times 10^{-4}$	$(2.2 \pm 0.1) \times 10^{-4}$	$(1.9 \pm 0.1) \times 10^{-4}$	$(2.1 \pm 0.1) \times 10^{-4}$	$(2.9 \pm 0.1) \times 10^{-4}$	
3; 10	$(2.9 \pm 0.2) \times 10^{-5}$	$(3.5 \pm 0.3) \times 10^{-5}$	$(3.7 \pm 0.3) \times 10^{-5}$	$(7.0 \pm 0.4) \times 10^{-5}$	$(13.3 \pm 0.5) \times 10^{-5}$	
10; 30	$(1.70 \pm 0.08) \times 10^{-5}$	$(1.8 \pm 0.1) \times 10^{-5}$	$(2.1 \pm 0.1) \times 10^{-5}$	$(2.4 \pm 0.1) \times 10^{-5}$	$(2.6 \pm 0.1) \times 10^{-5}$	
30; 100	$(4.5 \pm 0.2) \times 10^{-6}$	$(5.0 \pm 0.3) \times 10^{-6}$	$(5.2 \pm 0.3) \times 10^{-6}$	$(4.7 \pm 0.3) \times 10^{-6}$	$(5.4 \pm 0.3) \times 10^{-6}$	
100; 200	$(2.4 \pm 0.1) \times 10^{-6}$	$(2.4 \pm 0.2) \times 10^{-6}$				

Table 3.11: Downward electron differential flux $\bar{\Phi}_{(e^-)}^{40^\circ}(E_k)$ ($\text{m}^2 \text{ sr s MeV}^{-1}$):

Kinetic Energy (GeV)	Geomagnetic Latitude (rad)			
	$0.6 \leq \Theta_M < 0.7$	$0.7 \leq \Theta_M < 0.8$	$0.8 \leq \Theta_M < 0.9$	$0.9 \leq \Theta_M < 1.0$
0.1; 0.3	$(3.0 \pm 0.1) \times 10^{-2}$	$(3.0 \pm 0.1) \times 10^{-2}$	$(3.2 \pm 0.1) \times 10^{-2}$	$(4.2 \pm 0.1) \times 10^{-2}$
0.3; 1	$(2.95 \pm 0.08) \times 10^{-3}$	$(4.20 \pm 0.09) \times 10^{-3}$	$(4.20 \pm 0.09) \times 10^{-3}$	$(10.7 \pm 0.2) \times 10^{-3}$
1; 3	$(5.0 \pm 0.2) \times 10^{-4}$	$(11.7 \pm 0.2) \times 10^{-4}$	$(27.7 \pm 0.4) \times 10^{-4}$	$(53.1 \pm 0.7) \times 10^{-4}$
3; 10	$(28.2 \pm 0.7) \times 10^{-5}$	$(48.4 \pm 0.8) \times 10^{-5}$	$(5.6 \pm 0.1) \times 10^{-4}$	$(5.9 \pm 0.1) \times 10^{-4}$
10; 30	$(3.1 \pm 0.1) \times 10^{-5}$	$(3.4 \pm 0.1) \times 10^{-5}$	$(3.2 \pm 0.2) \times 10^{-5}$	$(3.3 \pm 0.2) \times 10^{-5}$
30; 100	$(5.4 \pm 0.3) \times 10^{-6}$	$(5.9 \pm 0.2) \times 10^{-6}$	$(5.6 \pm 0.3) \times 10^{-6}$	$(4.8 \pm 0.3) \times 10^{-6}$
100; 200	$(2.4 \pm 0.2) \times 10^{-6}$	$(2.4 \pm 0.2) \times 10^{-6}$	$(2.7 \pm 0.2) \times 10^{-6}$	$(1.9 \pm 0.2) \times 10^{-6}$

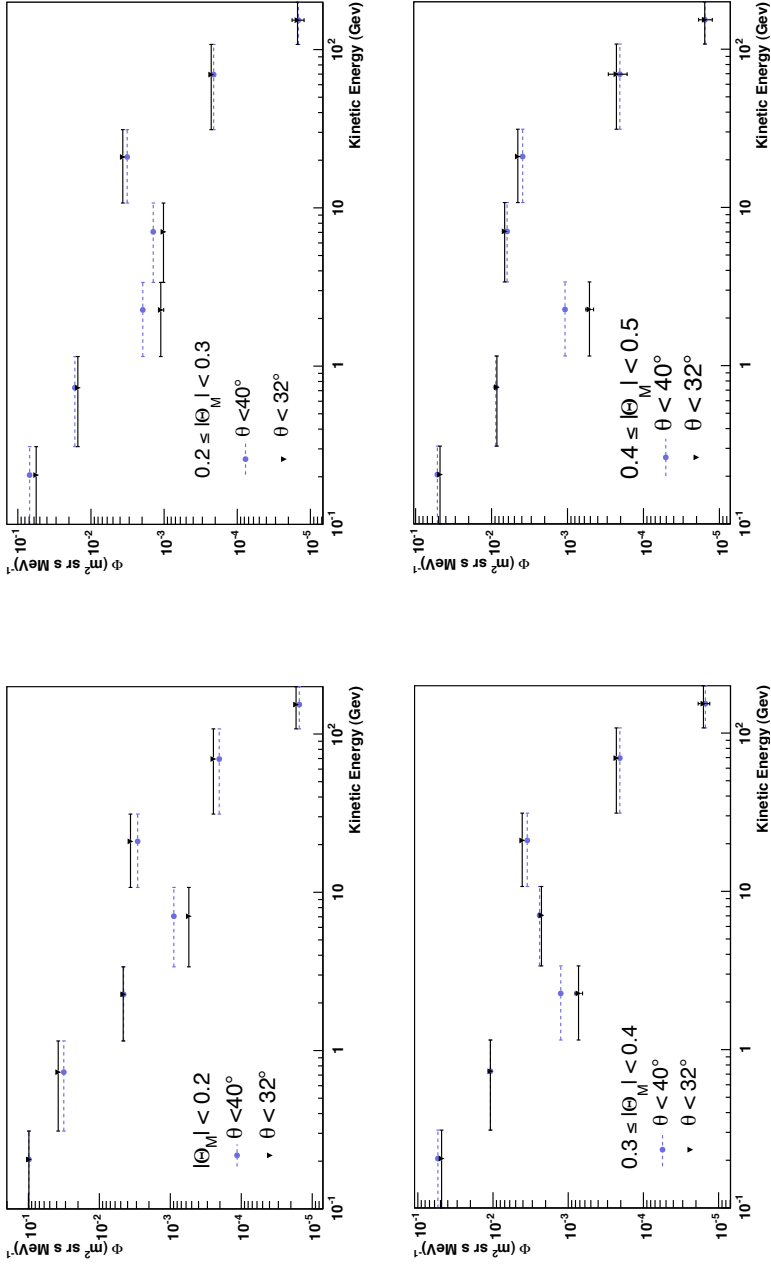


Figure 3.12: Proton differential spectra as a function of the incident kinetic energy for the geomagnetic latitude regions $|\Theta_M| < 0.2$ (top left), $0.2 \leq |\Theta_M| < 0.3$ (top right), $0.3 \leq |\Theta_M| < 0.4$ (bottom left) and $0.4 \leq |\Theta_M| < 0.5$ (bottom right). The blue dots on dashed lines represent the flux resulting from the present analysis, $\bar{\Phi}_{(p)}^{40^\circ}(E_k)$, while the black triangles on continuous lines represent the flux measured in previous analysis of the AMS-01 data [21, 77], $\bar{\Phi}_{(p)}^{40^\circ}(E_k)$ and $\bar{\Phi}_{(p)}^{32^\circ}(E_k)$ in correspondence to the energy range including the geomagnetic cutoff value is due to the less fine energy binning used in the present work.

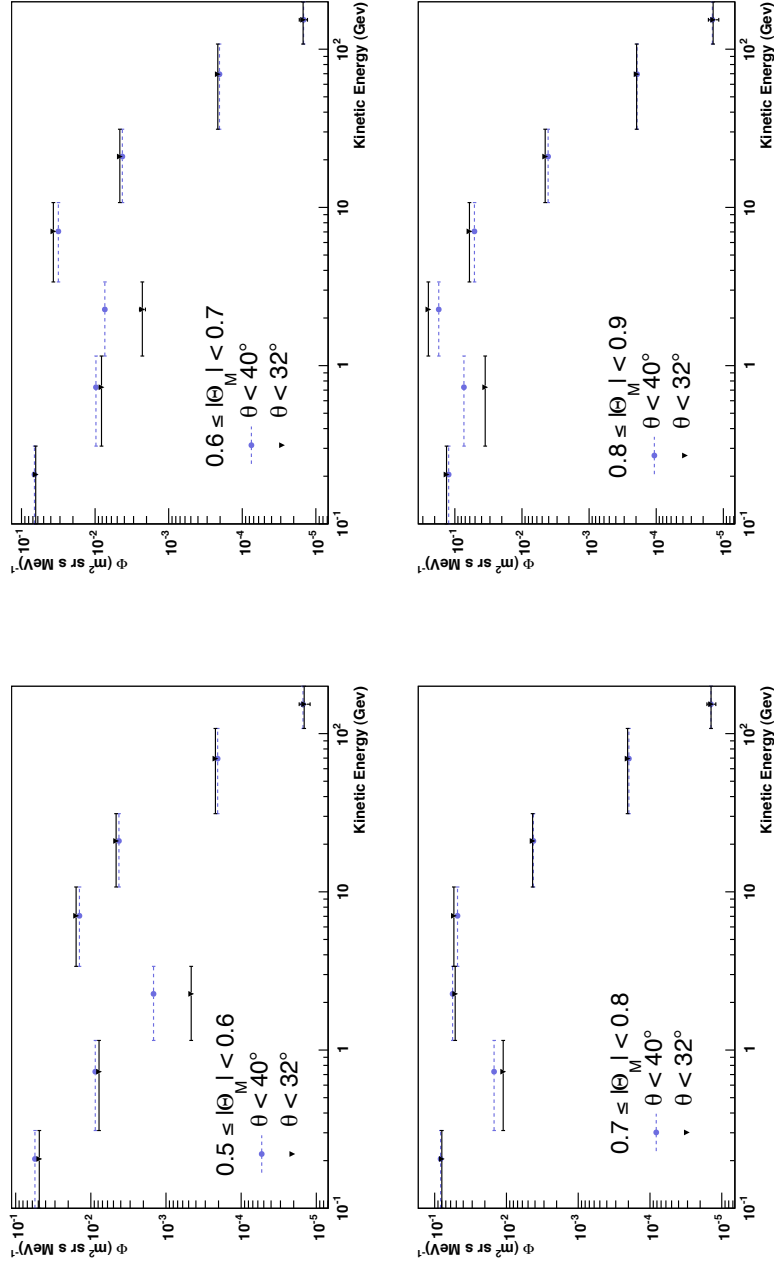


Figure 3.13: Proton differential spectra as a function of the incident kinetic energy for the geomagnetic latitude regions $0.5 \leq |\Theta_M| < 0.6$ (top left), $0.6 \leq |\Theta_M| < 0.7$ (top right), $0.7 \leq |\Theta_M| < 0.8$ (bottom left) and $0.8 \leq |\Theta_M| < 0.9$ (bottom right). The blue dots on dashed lines represent the flux resulting from the present analysis, $\bar{\Phi}_{(p)}^{40^\circ}(E_k)$, while the black triangles on continuous lines represent the flux measured in previous analysis of the AMS-01 data [21, 77], $\bar{\Phi}_{(p)}^{32^\circ}(E_k)$. The discrepancy between $\bar{\Phi}_{(p)}^{40^\circ}(E_k)$ and $\bar{\Phi}_{(p)}^{32^\circ}(E_k)$ in correspondence to the energy range including the geomagnetic cutoff value is due to the less fine energy binning used in the present work.

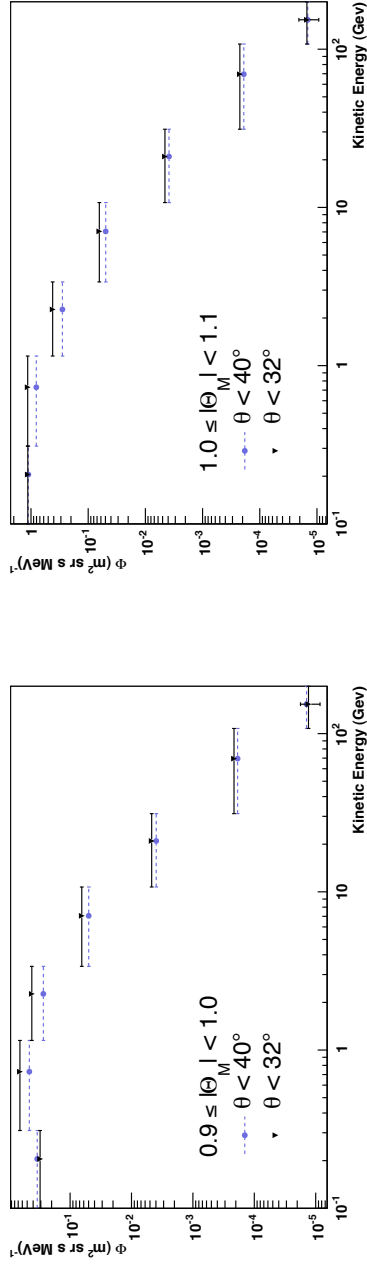


Figure 3.14: Proton differential spectra as a function of the incident kinetic energy for the geomagnetic latitude regions $0.9 \leq |\Theta_M| < 1.0$ (left) and $1.0 \leq |\Theta_M| < 1.1$ (right). The blue dots on dashed lines represent the flux resulting from the present analysis, $\bar{\Phi}_{(p)}^{40^\circ}(E_k)$, while the black triangles on continuous lines represent the flux measured in previous analysis of the AMS-01 data [21, 77], $\bar{\Phi}_{(p)}^{32^\circ}(E_k)$. The discrepancy between $\bar{\Phi}_{(p)}^{40^\circ}(E_k)$ and $\bar{\Phi}_{(p)}^{32^\circ}(E_k)$ in correspondence to the energy range including the geomagnetic cutoff value is due to the less fine energy binning used in the present work.

Table 3.12: Downward proton differential flux $\bar{\Phi}_{(p)}^{40^\circ}(E_k)$ ($\text{m}^2 \text{ sr s MeV}^{-1}$):

Kinetic Energy (GeV)	Geomagnetic Latitude (rad)				
	$ \Theta_M < 0.2$	$0.2 \leq \Theta_M < 0.3$	$0.3 \leq \Theta_M < 0.4$	$0.4 \leq \Theta_M < 0.5$	$0.5 \leq \Theta_M < 0.6$
0.1; 0.3	$(9.8 \pm 0.8) \times 10^{-2}$	$(6.9 \pm 0.5) \times 10^{-2}$	$(5.4 \pm 0.4) \times 10^{-2}$	$(5.2 \pm 0.4) \times 10^{-2}$	$(5.5 \pm 0.4) \times 10^{-2}$
0.3; 1	$(3.2 \pm 0.2) \times 10^{-2}$	$(1.7 \pm 0.1) \times 10^{-2}$	$(1.08 \pm 0.07) \times 10^{-2}$	$(8.8 \pm 0.6) \times 10^{-3}$	$(8.7 \pm 0.6) \times 10^{-3}$
1; 3	$(4.6 \pm 0.3) \times 10^{-3}$	$(2.0 \pm 0.1) \times 10^{-3}$	$(1.26 \pm 0.08) \times 10^{-3}$	$(1.08 \pm 0.07) \times 10^{-3}$	$(1.5 \pm 0.1) \times 10^{-3}$
3; 10	$(8.9 \pm 0.6) \times 10^{-4}$	$(1.41 \pm 0.09) \times 10^{-3}$	$(2.4 \pm 0.1) \times 10^{-3}$	$(6.2 \pm 0.2) \times 10^{-3}$	$(1.42 \pm 0.09) \times 10^{-2}$
10; 30	$(2.9 \pm 0.2) \times 10^{-3}$	$(3.2 \pm 0.2) \times 10^{-3}$	$(3.5 \pm 0.2) \times 10^{-3}$	$(3.9 \pm 0.2) \times 10^{-3}$	$(4.2 \pm 0.3) \times 10^{-3}$
30; 100	$(2.0 \pm 0.1) \times 10^{-4}$	$(2.1 \pm 0.1) \times 10^{-4}$	$(2.1 \pm 0.1) \times 10^{-4}$	$(2.1 \pm 0.1) \times 10^{-4}$	$(2.1 \pm 0.1) \times 10^{-4}$
100; 200	$(1.5 \pm 0.1) \times 10^{-5}$	$(1.5 \pm 0.1) \times 10^{-5}$	$(1.5 \pm 0.1) \times 10^{-5}$	$(1.5 \pm 0.1) \times 10^{-5}$	$(1.5 \pm 0.1) \times 10^{-5}$

Table 3.13: Downward proton differential flux $\bar{\Phi}_{(p)}^{40^\circ}(E_k)$ ($\text{m}^2 \text{sr s MeV}^{-1}$):

Kinetic Energy (GeV)	Geomagnetic Latitude (rad)				
	$0.6 \leq \Theta_M < 0.7$	$0.7 \leq \Theta_M < 0.8$	$0.8 \leq \Theta_M < 0.9$	$0.9 \leq \Theta_M < 1.0$	$1.0 \leq \Theta_M < 1.1$
0.1; 0.3	$(6.7 \pm 0.5) \times 10^{-2}$	$(8.3 \pm 0.6) \times 10^{-2}$	$(1.2 \pm 0.1) \times 10^{-1}$	$(3.4 \pm 0.2) \times 10^{-1}$	$(11.1 \pm 0.9) \times 10^{-1}$
0.3; 1	$(9.7 \pm 0.6) \times 10^{-3}$	$(1.5 \pm 0.1) \times 10^{-2}$	$(7.3 \pm 0.5) \times 10^{-2}$	$(4.6 \pm 0.3) \times 10^{-1}$	$(8.1 \pm 0.5) \times 10^{-1}$
1; 3	$(7.4 \pm 0.5) \times 10^{-3}$	$(5.6 \pm 0.4) \times 10^{-3}$	$(1.7 \pm 0.1) \times 10^{-1}$	$(2.7 \pm 0.2) \times 10^{-1}$	$(2.8 \pm 0.2) \times 10^{-1}$
3; 10	$(3.2 \pm 0.2) \times 10^{-2}$	$(4.8 \pm 0.3) \times 10^{-2}$	$(5.1 \pm 0.3) \times 10^{-2}$	$(5.0 \pm 0.3) \times 10^{-2}$	$(4.9 \pm 0.3) \times 10^{-2}$
10; 30	$(4.3 \pm 0.3) \times 10^{-3}$	$(4.2 \pm 0.3) \times 10^{-3}$	$(4.1 \pm 0.3) \times 10^{-3}$	$(4.0 \pm 0.2) \times 10^{-3}$	$(3.9 \pm 0.2) \times 10^{-3}$
30; 100	$(2.0 \pm 0.1) \times 10^{-4}$	$(2.0 \pm 0.1) \times 10^{-4}$	$(1.9 \pm 0.1) \times 10^{-4}$	$(1.9 \pm 0.1) \times 10^{-4}$	$(1.9 \pm 0.1) \times 10^{-4}$
100; 200	$(1.5 \pm 0.1) \times 10^{-5}$	$(1.4 \pm 0.1) \times 10^{-5}$	$(1.5 \pm 0.1) \times 10^{-5}$	$(1.4 \pm 0.1) \times 10^{-5}$	$(1.4 \pm 0.1) \times 10^{-5}$

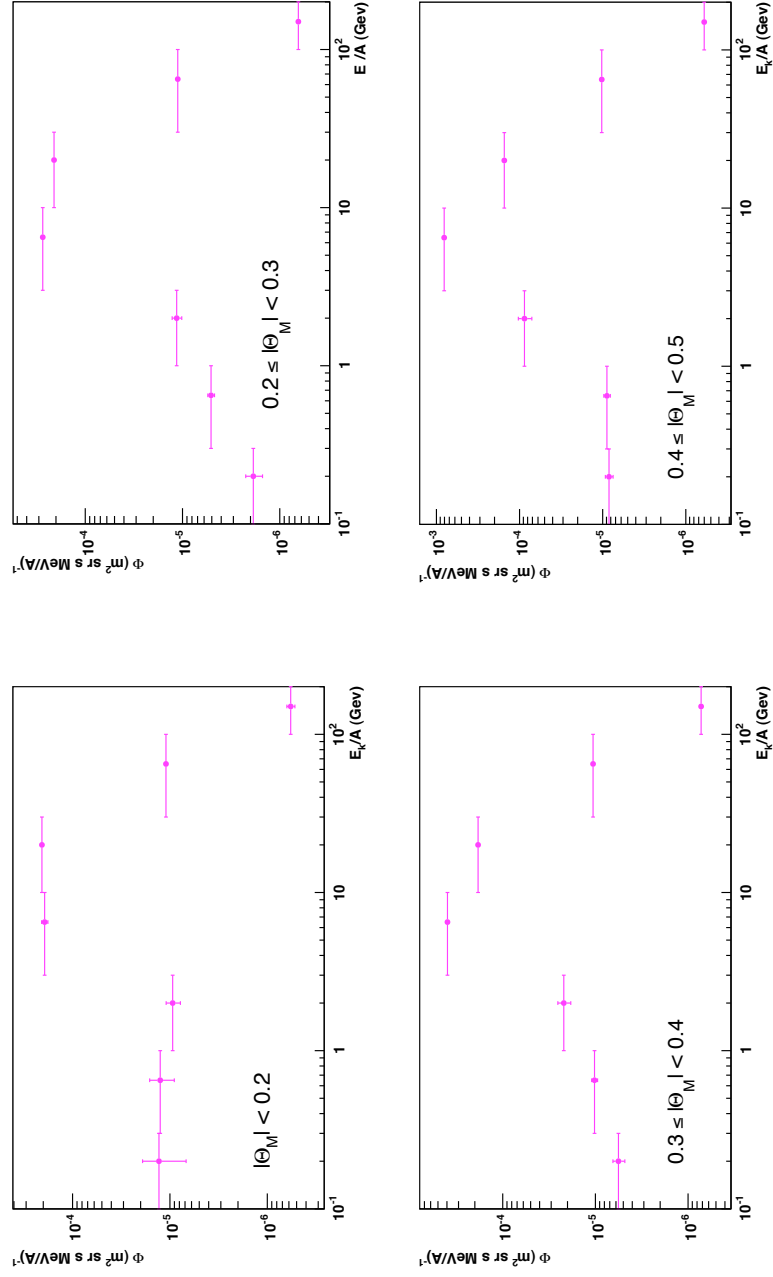


Figure 3.15: He nuclei differential spectra as a function of the incident kinetic energy for the geomagnetic latitude regions $|\Theta_M| < 0.2$ (top left), $0.2 \leq |\Theta_M| < 0.3$ (top right), $0.3 \leq |\Theta_M| < 0.4$ (bottom left) and $0.4 \leq |\Theta_M| < 0.5$ (bottom right).

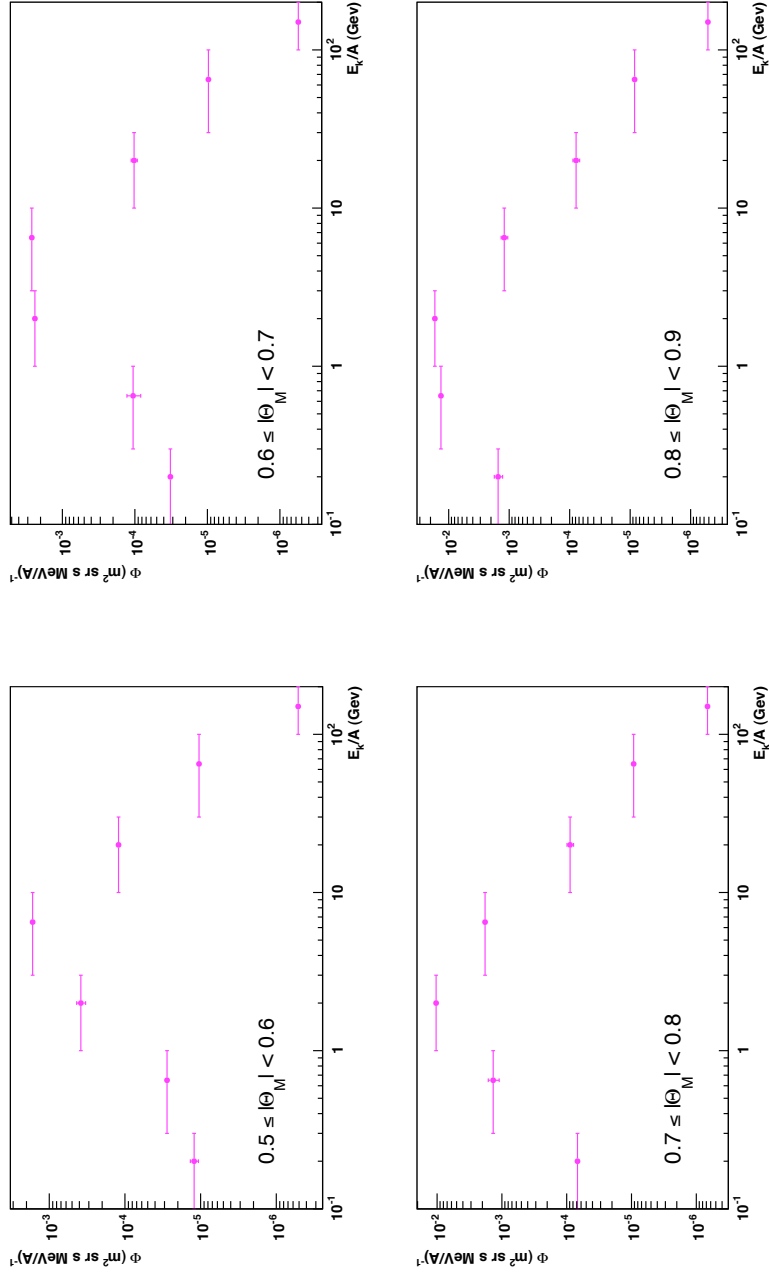


Figure 3.16: He nuclei differential spectra as a function of the incident kinetic energy for the geomagnetic latitude regions $0.5 \leq |\Theta_M| < 0.6$ (top left), $0.6 \leq |\Theta_M| < 0.7$ (top right), $0.7 \leq |\Theta_M| < 0.8$ (bottom left) and $0.8 \leq |\Theta_M| < 0.9$ (bottom right).

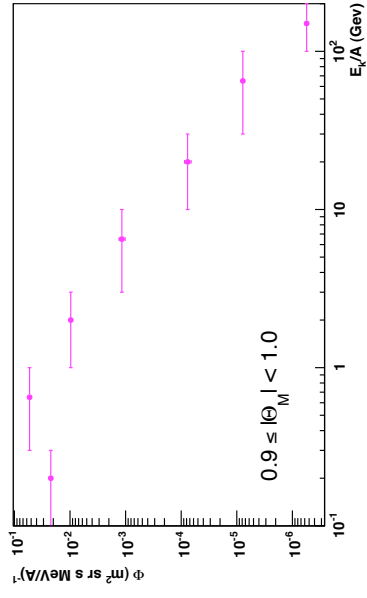
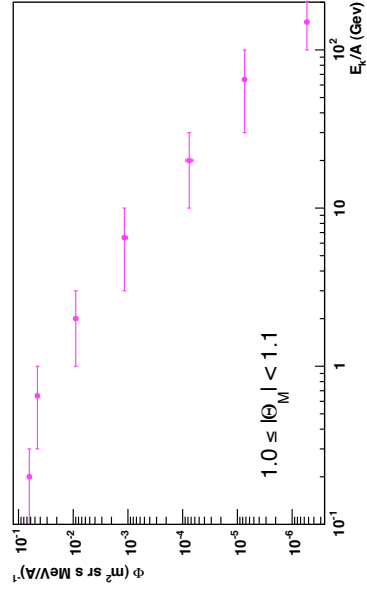


Figure 3.17: He nuclei differential spectra as a function of the incident kinetic energy for the geomagnetic latitude regions $0.9 \leq |\Theta_M| < 1.0$ (left) and $1.0 \leq |\Theta_M| < 1.1$ (right).

Table 3.14: Downward He nuclei differential flux $\bar{\Phi}_{(\text{He})}^{40^\circ}(E_k/A)$ ($\text{m}^2 \text{sr s MeV/A})^{-1}$;

Kinetic Energy per nucleon (GeV/A)	Geomagnetic Latitude (rad)				
	$ \Theta_M < 0.2$	$0.2 \leq \Theta_M < 0.3$	$0.3 \leq \Theta_M < 0.4$	$0.4 \leq \Theta_M < 0.5$	$0.5 \leq \Theta_M < 0.6$
0.1; 0.3	$(1.3 \pm 0.6) \times 10^{-5}$	$(1.9 \pm 0.4) \times 10^{-6}$	$(5.6 \pm 0.8) \times 10^{-6}$	$(8.4 \pm 0.9) \times 10^{-6}$	$(1.2 \pm 0.1) \times 10^{-5}$
0.3; 1	$(1.3 \pm 0.4) \times 10^{-5}$	$(5.1 \pm 0.4) \times 10^{-6}$	$(1.02 \pm 0.08) \times 10^{-5}$	$(8.9 \pm 0.8) \times 10^{-6}$	$(2.8 \pm 0.2) \times 10^{-5}$
1; 3	$(9.4 \pm 0.2) \times 10^{-5}$	$(1.1 \pm 0.1) \times 10^{-5}$	$(2.2 \pm 0.3) \times 10^{-5}$	$(0.9 \pm 0.2) \times 10^{-4}$	$(3.8 \pm 0.5) \times 10^{-4}$
3; 10	$(1.9 \pm 0.1) \times 10^{-4}$	$(2.7 \pm 0.2) \times 10^{-4}$	$(3.9 \pm 0.2) \times 10^{-4}$	$(8.1 \pm 0.3) \times 10^{-4}$	$(1.66 \pm 0.06) \times 10^{-3}$
10; 30	$(2.06 \pm 0.09) \times 10^{-4}$	$(2.09 \pm 0.09) \times 10^{-4}$	$(1.85 \pm 0.08) \times 10^{-4}$	$(1.53 \pm 0.08) \times 10^{-4}$	$(1.22 \pm 0.09) \times 10^{-4}$
30; 100	$(1.10 \pm 0.06) \times 10^{-5}$	$(1.12 \pm 0.06) \times 10^{-5}$	$(1.06 \pm 0.06) \times 10^{-5}$	$(1.03 \pm 0.06) \times 10^{-5}$	$(1.05 \pm 0.06) \times 10^{-5}$
100; 200	$(5.7 \pm 0.5) \times 10^{-7}$	$(6.4 \pm 0.3) \times 10^{-7}$	$(7.2 \pm 0.3) \times 10^{-7}$	$(6.0 \pm 0.3) \times 10^{-7}$	$(5.1 \pm 0.2) \times 10^{-7}$

Table 3.15: Downward He nuclei differential flux $\bar{\Phi}_{(\text{He})}^{40^\circ}(E_k/A)$ ($\text{m}^2 \text{sr s MeV/A}$) $^{-1}$:

Kinetic Energy per nucleon (GeV/A)	Geomagnetic Latitude (rad)			
	$0.6 \leq \Theta_M < 0.7$	$0.7 \leq \Theta_M < 0.8$	$0.8 \leq \Theta_M < 0.9$	$0.9 \leq \Theta_M < 1.0$ $1.0 \leq \Theta_M < 1.1$
0.1; 0.3	$(3.2 \pm 0.3) \times 10^{-5}$	$(6.8 \pm 0.6) \times 10^{-5}$	$(1.5 \pm 0.2) \times 10^{-3}$	$(2.2 \pm 0.2) \times 10^{-2}$ $(6.3 \pm 0.2) \times 10^{-2}$
0.3; 1	$(1.1 \pm 0.2) \times 10^{-4}$	$(1.2 \pm 0.3) \times 10^{-3}$	$(1.34 \pm 0.07) \times 10^{-2}$	$(5.3 \pm 0.2) \times 10^{-2}$ $(4.5 \pm 0.2) \times 10^{-2}$
1; 3	$(2.4 \pm 0.1) \times 10^{-3}$	$(1.04 \pm 0.04) \times 10^{-2}$	$(1.69 \pm 0.06) \times 10^{-2}$	$(9.7 \pm 0.9) \times 10^{-3}$ $(9.0 \pm 0.9) \times 10^{-3}$
3; 10	$(2.6 \pm 0.1) \times 10^{-3}$	$(1.8 \pm 0.1) \times 10^{-3}$	$(1.2 \pm 0.2) \times 10^{-3}$	$(1.2 \pm 0.1) \times 10^{-3}$ $(1.2 \pm 0.1) \times 10^{-3}$
10; 30	$(1.0 \pm 0.1) \times 10^{-4}$	$(0.9 \pm 0.1) \times 10^{-4}$	$(0.8 \pm 0.1) \times 10^{-4}$	$(0.8 \pm 0.1) \times 10^{-4}$ $(0.8 \pm 0.1) \times 10^{-4}$
30; 100	$(9.7 \pm 0.6) \times 10^{-6}$	$(9.3 \pm 0.5) \times 10^{-6}$	$(8.4 \pm 0.5) \times 10^{-6}$	$(7.8 \pm 0.6) \times 10^{-6}$ $(7.4 \pm 0.6) \times 10^{-6}$
100; 200	$(5.6 \pm 0.3) \times 10^{-7}$	$(6.7 \pm 0.3) \times 10^{-7}$	$(5.2 \pm 0.2) \times 10^{-7}$	$(5.5 \pm 0.3) \times 10^{-7}$ $(5.4 \pm 0.3) \times 10^{-7}$

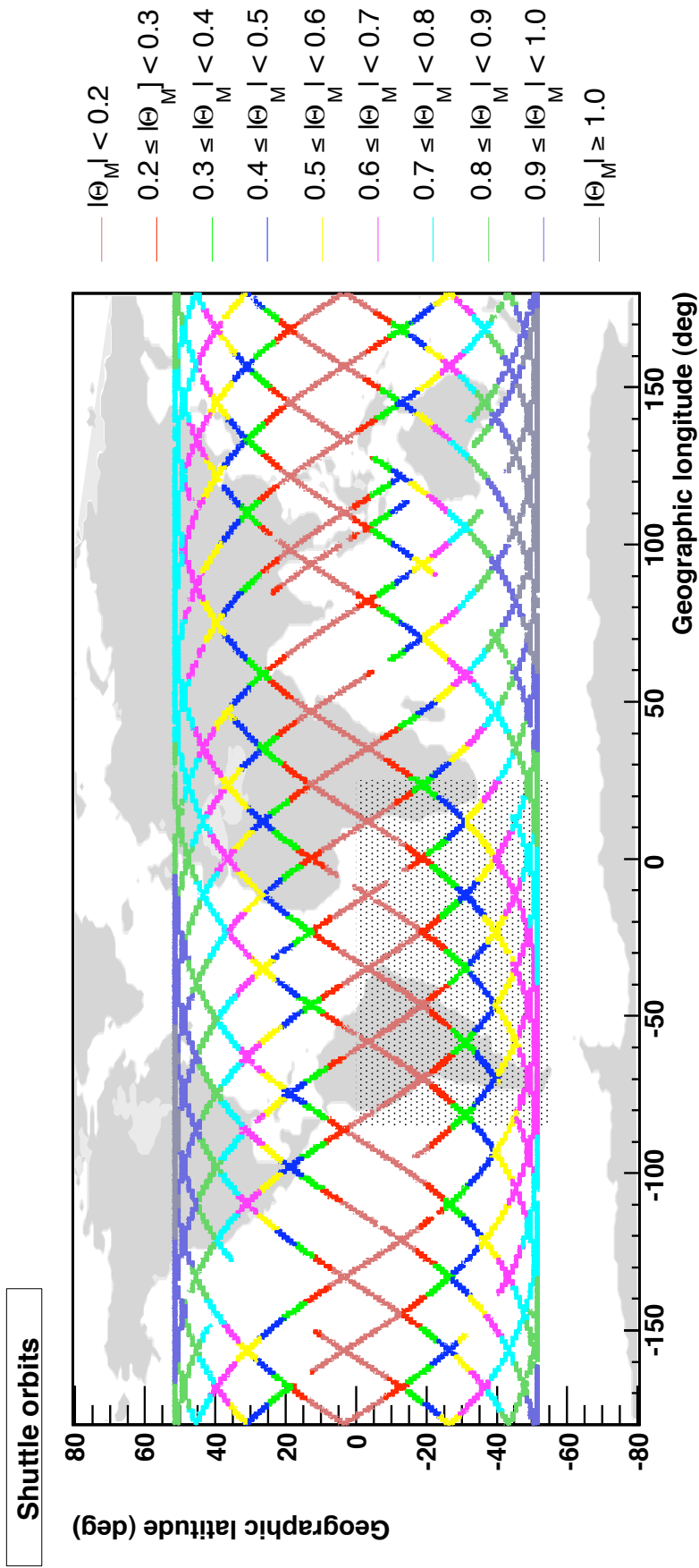


Figure 3.18: Shuttle orbits for a 24 hours flight period. Geomagnetic latitude regions are shown in different colors. The shaded area is the SAA exclusion region.

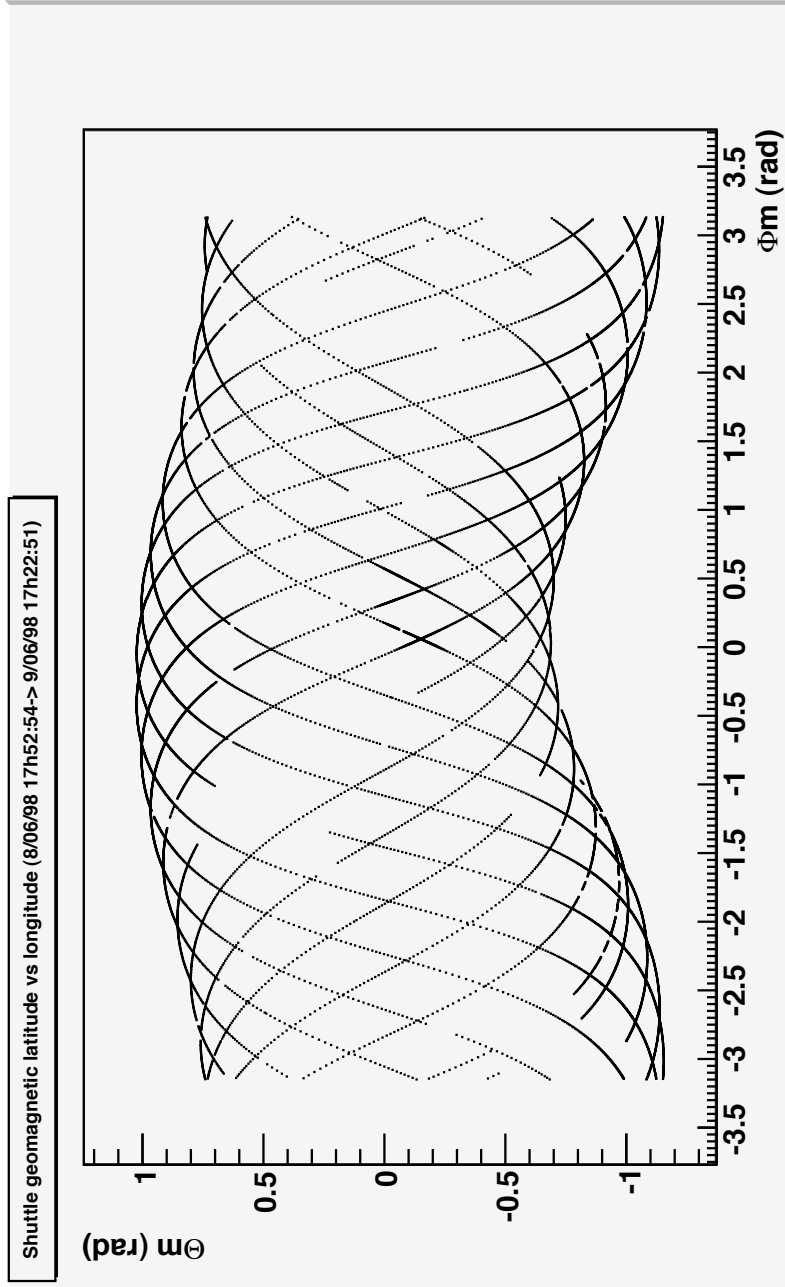


Figure 3.19: Space Shuttle geomagnetic orbits on a 24 hours flight period.

3.3 Search for rapid cosmic-ray flux variations

The amount of data collected after the Shuttle had undocked from the MIR station has been analysed in order to search for systematic electron, proton and He nuclei flux fluctuations as a function of time. Only downward going particles have been considered. Since data taken when the detector was facing the Earth are excluded, the Nadir pointing period (from 2h49 UT to 12h55 UT of June 12 1998) is in fact not included in the analysis. The pointing chronology [97], after undocking from MIR, is summarized in Table 3.16.

Period	AMS Z-axis pointing:	
	zenithal angle (fixed)	azimuthal angle (variable)
June 8 17h53 UT to June 9 17h42 UT	0°	—
June 9 17h46 UT to June 9 21h03 UT	45°	±60° around South
June 9 21h06 UT to June 10 18h39 UT	20°	±60° around South
June 10 19h49 UT to June 11 1h27 UT	30°	±60° around South
June 11 1h29 UT to June 12 2h36 UT	45°	±60° around South

Table 3.16: AMS pointing chronology after *Discovery* undocking from MIR. The Nadir pointing period is not shown since it has not been included in the analysis. For each pointing period the angle between the AMS Z-axis and the Zenith direction was kept fixed (within 1°) at the value quoted in the table. For non-zero zenithal angle pointing periods the AMS Z-axis azimuthal angle was continuously varying between -60° and $+60^\circ$ around the South direction [98, 99].

A more detailed chronology of the whole AMS-01 Flight is reported in Appendix B. In Section B.0.1 are shown the Shuttle attitude parameters as a function of Mission Elapsed Time for the period from June 8 to June 12.

3.3.1 Mean counting rate measurement

The geomagnetic region spanned by the Space Shuttle orbit (Figure 3.19) has been divided in 120 sectors with the following edges for the geomagnetic longitude:

$$\Phi_M = (\pm\pi; \pm\frac{2}{3}\pi; \pm\frac{1}{3}\pi; 0) \text{ rad}$$

and for the geomagnetic latitude:

$$\Theta_M = (\pm \frac{\pi}{2}; \pm 1; \pm 0.9; \pm 0.8; \pm 0.7; \pm 0.6; \pm 0.5; \pm 0.4; \pm 0.3; \pm 0.2; 0) \text{ rad.}$$

The South Atlantic Anomaly region has been excluded as explained in Section 3.1.

For each pointing period the mean counting rate for downward-going electrons, protons and He nuclei has been measured at each geomagnetic sector according to the following expression:

$$\bar{\Gamma}_{(i)}(E_k, \Phi_M, \Theta_M) = \frac{\bar{N}_{(i)}(E_k, \Phi_M, \Theta_M)}{T(\Phi_M, \Theta_M)} \quad i = e^-, p, \text{He} \quad (3.16)$$

where $T(\Phi_M, \Theta_M)$ and $\bar{N}_{(i)}(E_k, \Phi_M, \Theta_M)$ are the measurement time interval and the mean number of particles detected in the kinetic energy bin E_k respectively, at the geomagnetic sector (Φ_M, Θ_M) . The usual kinetic energy binning:

$$E_k : 0.1; 0.3; 1; 3; 10; 30; 100; 200 \text{ GeV/n}$$

has been used. Note that the measurement time is given by:

$$T(\Phi_M, \Theta_M) \equiv \Delta t(\Phi_M, \Theta_M) \cdot \text{DAQLifetime}(\Phi_M, \Theta_M) \quad (3.17)$$

where $\text{DAQLifetime}(\Phi_M, \Theta_M)$ is the detector lifetime (Figure 2.11), and $\Delta t(\Phi_M, \Theta_M)$ is the time spent inside the geomagnetic sector (Φ_M, Θ_M) , called the spanning time in the following.

The time spent inside each sector in a 24 hours data taking period is shown in Table(3.17). Periods when the Shuttle was passing across the SAA (see Section 3.1) and when the detector data acquisition was down are not taken into account. Depending on the Shuttle orbit the spanning time for the distinct sectors varied between 2 minutes and 24 minutes, with an average value of 10 minutes, as shown in Figure 3.20.

3.3.2 Actual counting rate measurement

To measure the actual counting rate the geomagnetic region has been split in smaller sectors, with the same geomagnetic latitude subdivision used for the mean counting rate and with the geomagnetic longitude binning 10 times finer than those reported in Section 3.3.1 in order to achieve a time sampling of about one minute. The actual sampling time varied between 30 seconds and 100 seconds (Table 3.18), with an average value of about 1 minute as shown in Figure 3.21.

The actual counting rate has been obtained similarly to equation (3.16):

$$\Gamma_{(i)}(E_k, \Phi_M, \Theta_M, t) = \frac{N_{(i)}(E_k, t)}{\tau(\Phi_M, \Theta_M)} \quad i = e^-, p, \text{He} \quad (3.18)$$

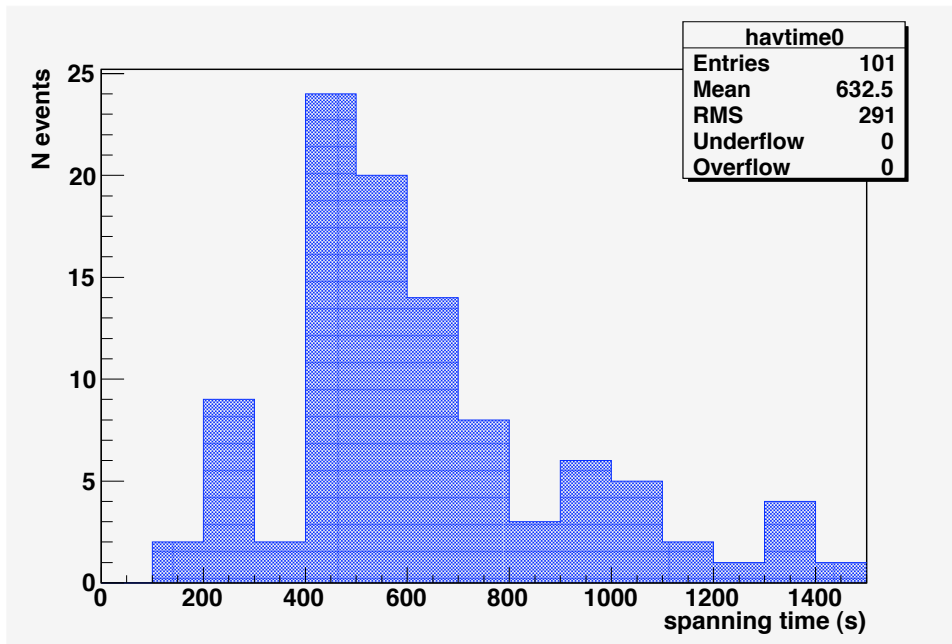


Figure 3.20: Time spent inside the geomagnetic sectors defined in Section 3.3.1, for the Zenith pointing period.

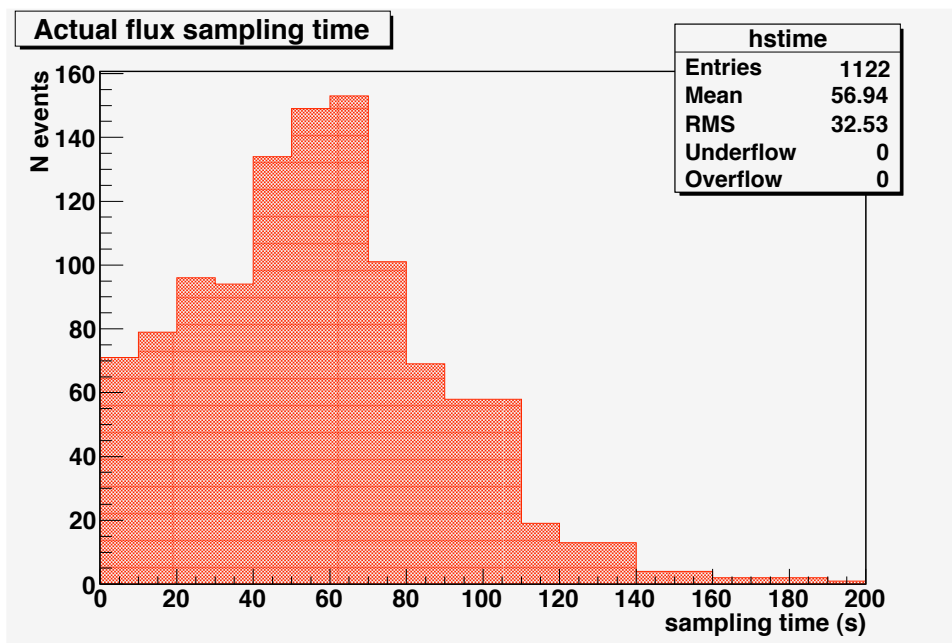


Figure 3.21: Actual counting rate sampling time for the Zenith pointing period.

	$-\pi \leq \Phi_M < -\frac{2}{3}\pi$	$-\frac{2}{3}\pi \leq \Phi_M < -\frac{1}{3}\pi$	$-\frac{1}{3}\pi \leq \Phi_M < 0$	$0 \leq \Phi_M < \frac{1}{3}\pi$	$\frac{1}{3}\pi \leq \Phi_M < \frac{2}{3}\pi$	$\frac{2}{3}\pi \leq \Phi_M < \pi$
$1 \leq \Theta_M < \frac{\pi}{2}$	0	0	609	249	0	0
$0.9 \leq \Theta_M < 1$	0	767	1157	1355	231	0
$0.8 \leq \Theta_M < 0.9$	286	1067	708	814	903	0
$0.7 \leq \Theta_M < 0.8$	1371	629	698	636	1035	1383
$0.6 \leq \Theta_M < 0.7$	876	418	401	651	777	625
$0.5 \leq \Theta_M < 0.6$	645	484	485	538	750	437
$0.4 \leq \Theta_M < 0.5$	600	460	484	540	694	511
$0.3 \leq \Theta_M < 0.4$	539	439	456	572	613	525
$0.2 \leq \Theta_M < 0.3$	583	362	449	574	582	426
$0 \leq \Theta_M < 0.2$	1054	985	818	434	1226	728
$-0.2 \leq \Theta_M < 0$	981	1093	776	0	509	1027
$-0.3 \leq \Theta_M < -0.2$	407	581	467	0	246	419
$-0.4 \leq \Theta_M < -0.3$	423	561	525	0	158	529
$-0.5 \leq \Theta_M < -0.4$	457	587	665	0	221	450
$-0.6 \leq \Theta_M < -0.5$	429	442	668	0	214	478
$-0.7 \leq \Theta_M < -0.6$	431	508	990	0	290	348
$-0.8 \leq \Theta_M < -0.7$	246	752	1148	0	469	464
$-0.9 \leq \Theta_M < -0.8$	534	920	208	0	657	580
$-1 \leq \Theta_M < -0.9$	617	943	0	0	786	558
$-\frac{\pi}{2} \leq \Theta_M < -1$	1435	507	0	0	135	1396

Table 3.17: Spanning time in seconds for each geomagnetic sector for the Zenith-pointing data taking period.

	$-\pi \leq \Phi_M < -\frac{2}{3}\pi$	$-\frac{2}{3}\pi \leq \Phi_M < -\frac{1}{3}\pi$	$-\frac{1}{3}\pi \leq \Phi_M < 0$	$0 \leq \Phi_M < \frac{1}{3}\pi$	$\frac{1}{3}\pi \leq \Phi_M < \frac{2}{3}\pi$	$\frac{2}{3}\pi \leq \Phi_M < \pi$
$1 \leq \Theta_M < \frac{\pi}{2}$	0	0	44	42	0	0
$0.9 \leq \Theta_M < 1$	0	45	48	52	46	0
$0.8 \leq \Theta_M < 0.9$	41	51	47	51	48	0
$0.7 \leq \Theta_M < 0.8$	57	52	63	64	49	66
$0.6 \leq \Theta_M < 0.7$	49	52	40	59	56	48
$0.5 \leq \Theta_M < 0.6$	46	61	61	60	75	49
$0.4 \leq \Theta_M < 0.5$	60	58	61	68	59	73
$0.3 \leq \Theta_M < 0.4$	49	55	65	64	68	66
$0.2 \leq \Theta_M < 0.3$	73	45	64	72	65	53
$0 \leq \Theta_M < 0.2$	81	90	102	48	94	73
$-0.2 \leq \Theta_M < 0$	82	84	86	0	73	103
$-0.3 \leq \Theta_M < -0.2$	68	73	52	0	82	47
$-0.4 \leq \Theta_M < -0.3$	53	62	75	0	32	88
$-0.5 \leq \Theta_M < -0.4$	57	65	51	0	70	50
$-0.6 \leq \Theta_M < -0.5$	61	49	69	0	54	53
$-0.7 \leq \Theta_M < -0.6$	62	51	62	0	73	50
$-0.8 \leq \Theta_M < -0.7$	41	58	64	0	47	58
$-0.9 \leq \Theta_M < -0.8$	59	48	42	0	51	53
$-1 \leq \Theta_M < -0.9$	44	43	0	0	44	47
$-\frac{\pi}{2} \leq \Theta_M < -1$	45	42	0	0	45	42

Table 3.18: Actual flux average sampling time in seconds for each geomagnetic sector for the Zenith-pointing data taking period.

where $N_{(i)}(E_k, t)$ and $\tau(\Phi_M, \Theta_M)$ are the actual number of detected particles and the measurement time inside the actual flux sampling geomagnetic sector. For the sake of notation simplicity the dependence on the geomagnetic position (Φ_M, Θ_M) in equation (3.18), as well as in the subsequent development of this document, has been omitted. For each actual counting rate measurement the expected counting rate is taken as being equal to the mean counting rate measured in the corresponding geomagnetic sector:

$$\Gamma_{(i)}^{exp}(E_k, \Phi_M, \Theta_M, t) \equiv \bar{\Gamma}_{(i)}(E_k, \Phi_M, \Theta_M). \quad (3.19)$$

As an example, Figure 3.22 shows the actual counting rate for protons compared to the expected counting rate and the flux variation in a three-hour period for two kinetic energy ranges, below and above the geomagnetic cutoff respectively. When the Shuttle was crossing the border of the SAA exclusion region⁷ the actual counting rate measured for particles with kinetic energy below the geomagnetic cutoff could be up to one order of magnitude higher than the mean flux. In order to better eliminate these variations due to geomagnetic structure, a more rigorous definition of the SAA has been adopted for the successive development of the analysis. Following a precedent study on particles trapped inside the SAA carried out with the AMS-01 data [100], the South Atlantic Anomaly excluding region has been redefined as the area where the local geomagnetic field is less than 0.26 Gauss. The corresponding region is shown in Figure 3.23.

3.3.3 Flux fluctuation occurrences

Flux fluctuations have been put in evidence studying the deviation of the measured actual number of particles, $N_{(i)}(E_k, t)$, from the expected Poisson distribution:

$$P(n, N_{(i)}^{exp}(E_k, t)) = e^{-N_{(i)}^{exp}(E_k, t)} \frac{N_{(i)}^{exp}(E_k, t)^n}{n!} \quad (3.20)$$

where the mean value is the expected actual counting number estimated from the mean flux measurement as follows:

$$N_{(i)}^{exp}(E_k, t) = \bar{\Gamma}_{(i)}(E_k, \Phi_M, \Theta_M) \cdot \tau(\Phi_M, \Theta_M). \quad (3.21)$$

For each actual number of particle measurement the probabilities of observing a number of particles above, $Prob(N \geq N_{(i)}(E_k, t))$ and below $Prob(N \leq N_{(i)}(E_k, t))$ the measured one have been computed from the Poisson distribution (3.20) as:

$$Prob(N \geq N_{(i)}(E_k, t)) = \sum_{n=N_{(i)}(E_k, t)}^{\infty} P(n, N_{(i)}^{exp}(E_k, t)) \quad (3.22)$$

$$Prob(N \leq N_{(i)}(E_k, t)) = \sum_{n=0}^{N_{(i)}(E_k, t)} P(n, N_{(i)}^{exp}(E_k, t)) \quad (3.23)$$

⁷Long.: 85° W; 25° E; Lat.: 0°; 55° S

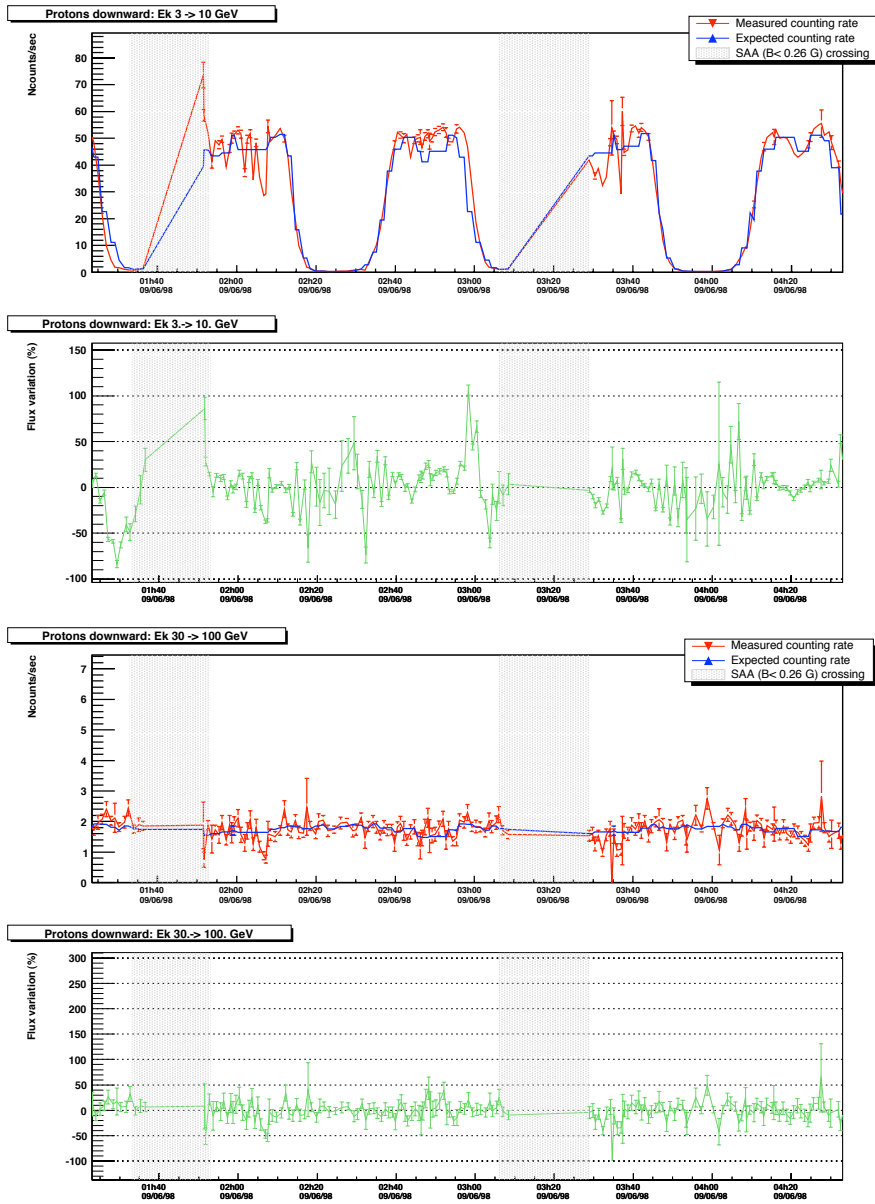


Figure 3.22: Proton actual counting rate (red curve) compared to the expected counting rate (blue curve) and flux variation (green curve) from 1h30 UT to 4h30 UT of June 9 1998 for kinetic energy ranges below (two uppermost panels) and above (two lowermost panels) the vertical geomagnetic cutoff. The grey regions highlight the periods when the Shuttle was inside the SAA region, defined as the region where the local geomagnetic field is less than 0.26 Gauss. Note the actual counting rate raise for under-cutoff protons when crossing the SAA.

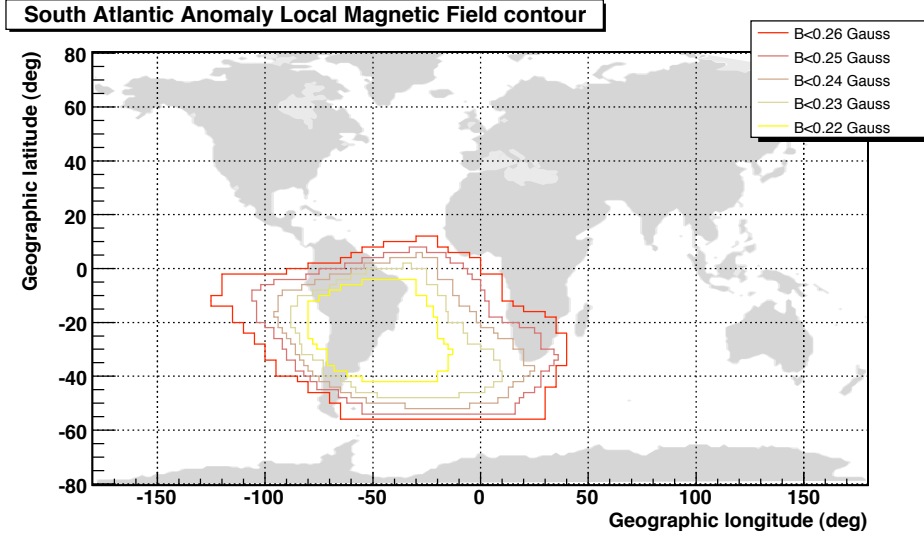


Figure 3.23: South Atlantic Anomaly local magnetic field contours at the AMS-01 flight altitude as calculated in Ref. [100].

These are, respectively, the probabilities to observe a statistical fluctuation upward and downward, which is at least as large as the observed one. These probabilities will be used to isolate fluctuations that are unlikely to be of statistical origin.

For the kinetic energy range above the geomagnetic cutoff, $30 \text{ GeV} \leq E_k < 200 \text{ GeV}$, both $Prob(N \geq N_{(i)}(E_k, t))$ and $Prob(N \leq N_{(i)}(E_k, t))$ have a flat distribution as shown in the two lowermost panels of Figure 3.24 for protons having kinetic energy between 30 GeV and 100 GeV. This fact indicates that the observed flux variations are compatible with the hypothesis of a statistical origin. There is little room for observable systematic variations in these fluxes.

On the contrary the probability distributions for the kinetic energy range below the geomagnetic cutoff, $0.1 \text{ GeV} \leq E_k < 30 \text{ GeV}$ peak at values close to 0 and 1, giving an indication of significant flux fluctuation occurrences. As an example $Prob(N \geq N_{(i)}(E_k, t))$ and $Prob(N \leq N_{(i)}(E_k, t))$ distributions for protons with kinetic energy between 3 GeV and 10 GeV are shown in the two uppermost panels of Figure 3.24. The same behaviour has been observed for electrons and He nuclei.

The remaining of the study has thus been focused on the under-cutoff kinetic energy range. A flux fluctuation occurrence in the kinetic energy bin E_k has been defined requiring a deviation from the expected Poisson distribution (3.20) greater than 3σ . Thus a significant deviation is defined by:

$$Prob(N \geq N_{(i)}(E_k, t)) < 10^{-3} \quad (3.24)$$

or

$$Prob(N \leq N_{(i)}(E_k, t)) < 10^{-3} \quad (3.25)$$

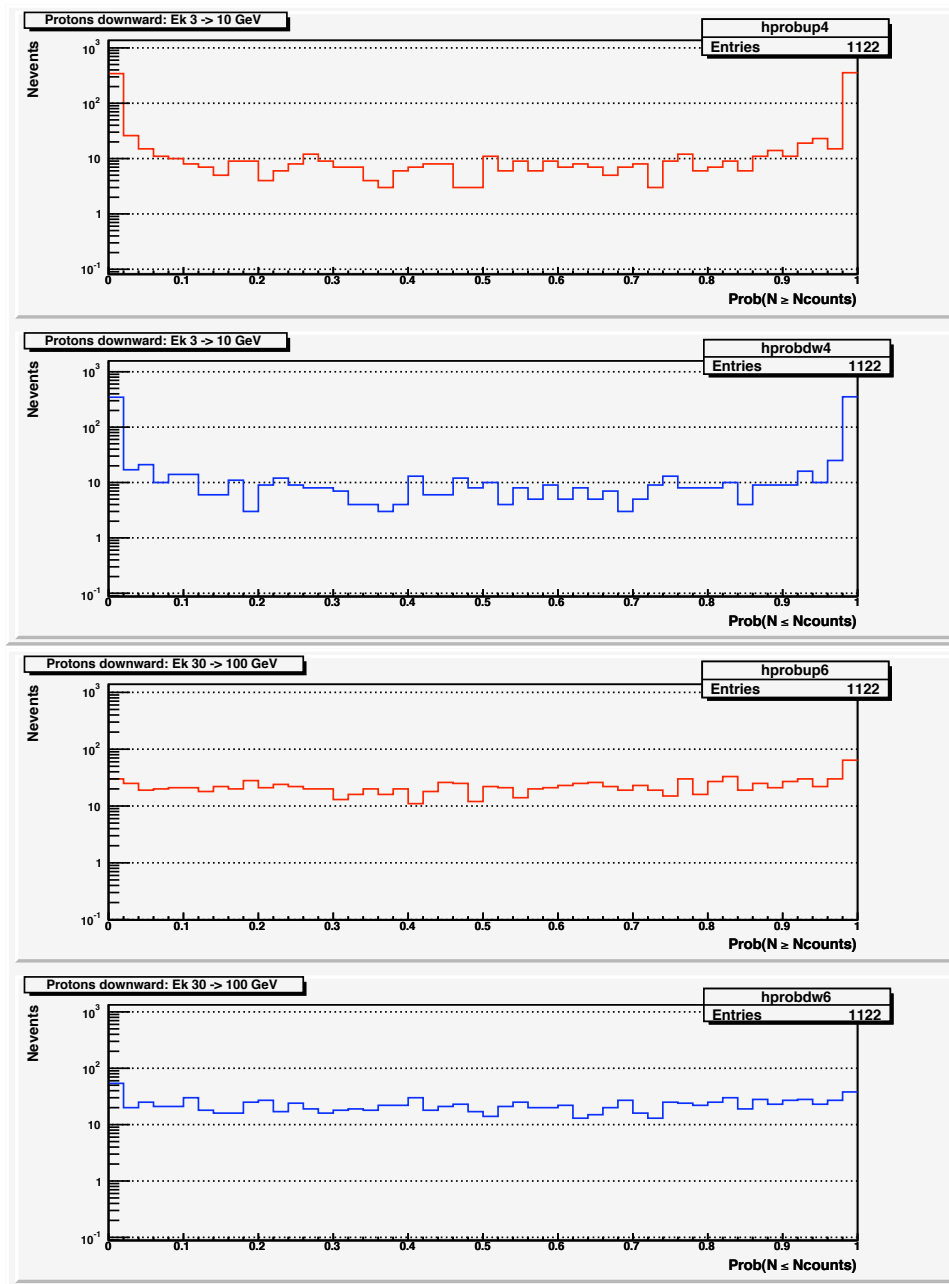


Figure 3.24: Probability distributions of observing a number of protons above, $Prob(N \geq N_{(i)}(E_k, t))$ (red curves), and below, $Prob(N \leq N_{(i)}(E_k, t))$ (blue curves), the measured actual number. Two upmost panels: $3 \leq E_k < 10$ GeV. The peak at low probabilities of the red[blue] curve is an indication of systematic flux increase[decrease] occurrences, while the peak at high probabilities is a reflection of the low probability peak of the complementary distribution (blue[red] curve). Two lowermost panels: $30 \leq E_k < 100$ GeV. The flatness of both probability distributions is the result of purely statistical flux fluctuations.

for positive and negative flux fluctuation events, respectively. Furthermore only those events for which a flux fluctuation has occurred in at least three adjacent kinetic energy bins out of the five below cutoff bins are kept. These events are listed in the catalog reported in Appendix A.

Significant flux fluctuations are observed for He nuclei and protons while they are rare for electrons. Several groups of time contiguous events lasting up to about 5 minutes are observed, some containing both positive and negative fluctuations.

The geomagnetic location of significant proton flux fluctuations is shown in Figure 3.25.

Next the frequencies of flux fluctuations, averaged over a three-hour period, have been computed as:

$$\nu_{fluct}^{(i)}(t) = \frac{N_{fluct}^{(i)}(t)}{\Delta t_{(3h)}} \quad i = e^-, p, \text{He} \quad (3.26)$$

where $\Delta t_{(3h)}$ and $N_{fluct}^{(i)}(t)$ are the measurement time and the number of fluctuation events observed in the three-hour absolute time period considered. Groups of time contiguous events are counted as a single event.

The frequencies of positive (top panel) and negative (bottom panel) flux fluctuations for electrons, protons and He nuclei are plotted versus the absolute time (given as Universal Time) in Figure 3.26.

The biggest effect is observed for protons. Although flux decreases occur more often than flux excesses, during active periods the two phenomena are observed essentially at the same time.

3.3.4 Comparison to the geomagnetic activity of 8-12 June 1998

In order to compare the level of flux fluctuation to the level of geomagnetic activity for the time interval covering the AMS-01 data taking period analysed (17h53 UT June 8 1998 to 2h36 UT June 12 1998), a three-hour-average proton flux fluctuation index, $Q_{fluct}^{(p)}$, has been defined as follows:

$$Q_{fluct}^{(p)}(t) = \sum_{k=0}^{n_{fluct}^{(p)}(t)} \frac{\tau_k \bar{i}_k}{\Delta t_{(3h)}} \quad (3.27)$$

where $\Delta t_{(3h)}$ and $n_{fluct}^{(p)}(t)$ are the measurement time and the total number of proton flux fluctuation events occurred in a three-hour period respectively, while τ_k and \bar{i}_k are the duration time and the intensity of the k -th fluctuation event. Here time contiguous events are treated separately.

For each event the intensity of the fluctuation is computed as the percentage flux variation averaged over the energy bins involved in the fluctuations. With this definition a negative fluctuation index corresponds to flux decreases dominance on flux increases, and viceversa a positive index reflects flux increases dominance on flux decreases.

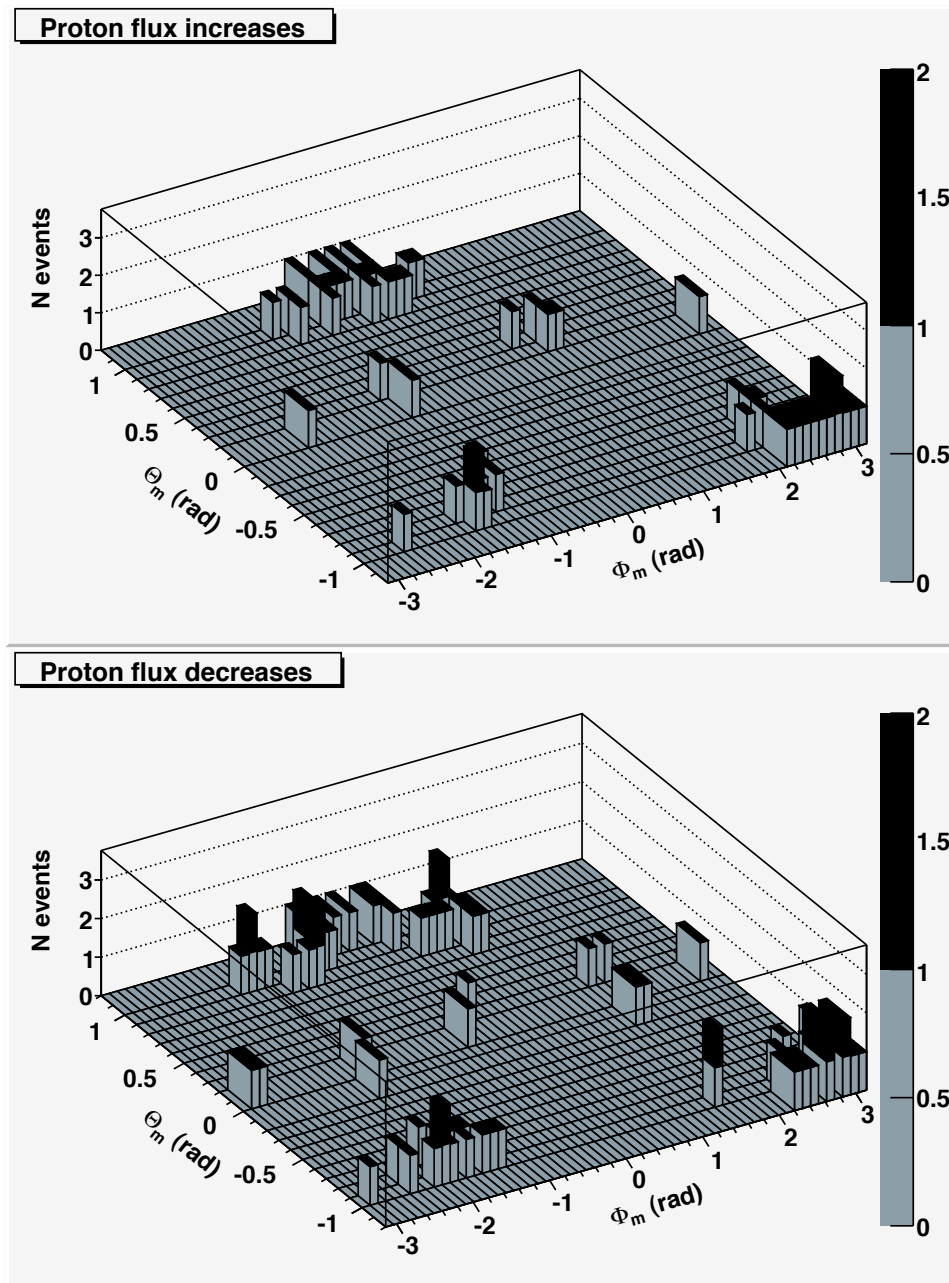


Figure 3.25: Geomagnetic location of significant proton flux increases (top panel) and decreases (bottom panel), for the Zenith pointing period.

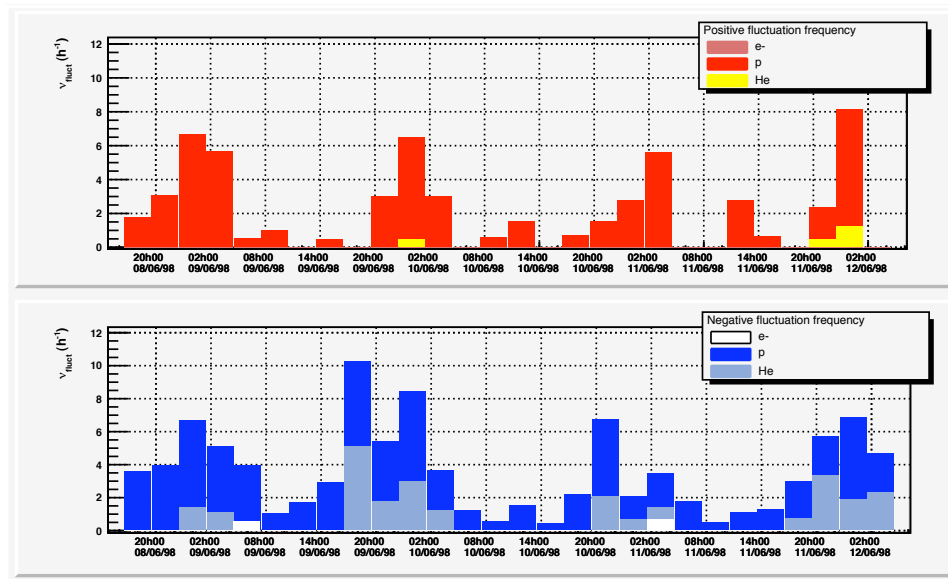


Figure 3.26: Flux fluctuation frequencies determined over a three-hour period for electrons, protons and He nuclei, observed from 17h53 UT June 8 1998 to 2h36 UT June 12 1998. The top panel shows frequencies for significant flux increases, the lower one those of flux decreases.

The flux fluctuation index for protons obtained for the time period 17h53 UT June 8 1998 to 2h36 UT June 12 1998 is reported in Figure 3.27.

Among the available indices describing the level of geomagnetic activity the planetary index K_P has been chosen, since it indicates the level of disturbance due to solar particle effects on the Earth's magnetic field.

The K_P index values for the period 18h00 UT June 8 1998 to 3h00 UT June 12 1998, retrieved from the Space Physics Interactive Data Resource (SPIDR) database [101], is shown in Figure 3.28.

The index K_P is calculated as a three-hour average from data taken from thirteen geomagnetic observatories measuring the Earth's magnetic field in subauroral latitudes ($44 - 60^\circ$).

The range of variation of the more unsettled horizontal field component is classified into the K_P index as disturbance levels ranging from 0 (quiet) to 9 (greatly disturbed) in 28 steps. Each activity level relates almost logarithmically to its corresponding disturbance amplitude.

Three-hour indices discriminate conservatively between true magnetic field perturbations and the quiet-day variations produced by ionospheric currents.

During the period considered in this work the level of geomagnetic activity was moderate, the K_P index being most of the time below level 3 and reaching at maximum level 4.7 at June 10 1998 midday.

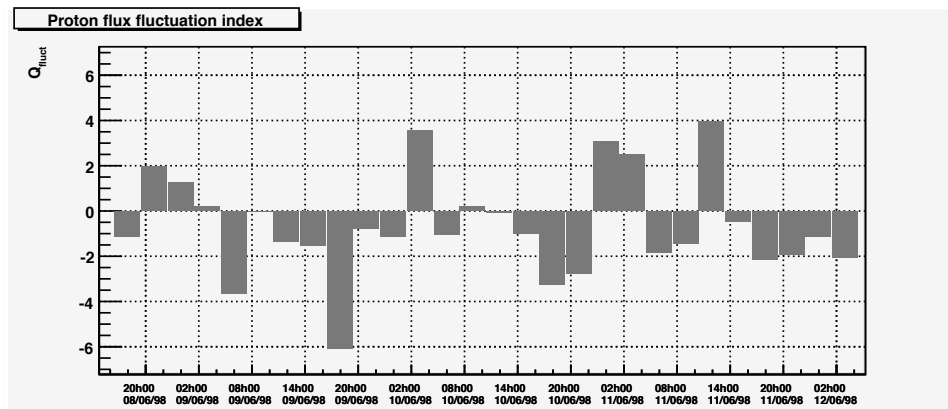


Figure 3.27: Proton flux fluctuation index $Q_{fluct}^{(p)}$ for the period 18h00 UT June 8 1998 to 3h00 UT June 12 1998.

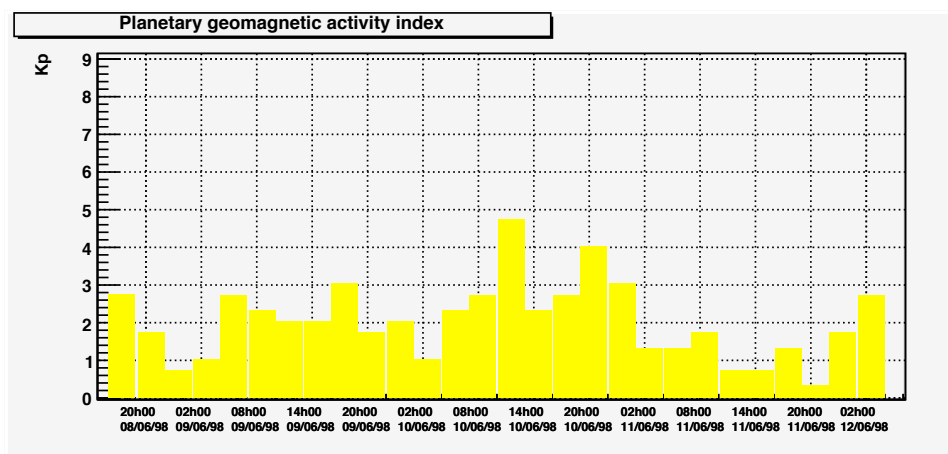


Figure 3.28: Planetary geomagnetic activity index K_P for the period 18h00 UT June 8 1998 to 3h00 UT June 12 1998.

The proton flux fluctuation index $Q_{fluct}^{(p)}$ is plotted against the corresponding K_P index in (Figure 3.29).

The Spearman rank correlation method [102, 103], applied to the proton flux fluctuation index $Q_{fluct}^{(p)}$ and to the K_P index pairs (Table 3.19), has given a correlation coefficient of -0.37 with 0.99 significance, resulting in the correspondence between high geomagnetic activity levels and proton flux decreases.

Since no systematic fluctuations have been observed for high energy particles, the correlation between magnetic disturbances and cosmic ray flux decreases concerns only under-cutoff particles, that is secondary particles created from the interaction of primary cosmic rays with the Earth's atmosphere which then stay trapped

UT	K_P	rank_{K_P}	$Q_{fluct}^{(p)}$	$\text{rank}_{Q_{fluct}^{(p)}}$
Jun 8 18:00	2.7	7	-1.1	16
Jun 8 21:00	1.7	17.5	2	5
Jun 9 00:00	0.7	26	1.2	6
Jun 9 03:00	1	23.5	0.2	7.5
Jun 9 06:00	2.7	7	-3.6	27
Jun 9 09:00	2.3	11	0	9.5
Jun 9 12:00	2	14	-1.3	18
Jun 9 15:00	2	14	-1.5	20
Jun 9 18:00	3	3.5	-6.1	28
Jun 9 21:00	1.7	17.5	-0.7	12
Jun 10 00:00	2	14	-1.1	16
Jun 10 03:00	1	23.5	3.5	2
Jun 10 06:00	2.3	11	-1	13.5
Jun 10 09:00	2.7	7	0.2	7.5
Jun 10 12:00	4.7	1	0	9.5
Jun 10 15:00	2.3	11	-1	13.5
Jun 10 18:00	2.7	7	-3.2	26
Jun 10 21:00	4	2	-2.7	25
Jun 11 00:00	3	3.5	3	3
Jun 11 03:00	1.3	21	2.5	4
Jun 11 06:00	1.3	21	-1.8	21
Jun 11 09:00	1.7	17.5	-1.4	19
Jun 11 12:00	0.7	26	3.9	1
Jun 11 15:00	0.7	26	-0.4	11
Jun 11 18:00	1.3	21	-2.1	24
Jun 11 21:00	0.3	28	-1.9	22
Jun 12 00:00	1.7	17.5	-1.1	16
Jun 12 03:00	2.7	7	-2	23

Table 3.19: Proton flux fluctuation index $Q_{fluct}^{(p)}$ and K_P index pairs, with the corresponding Spearman ranks.

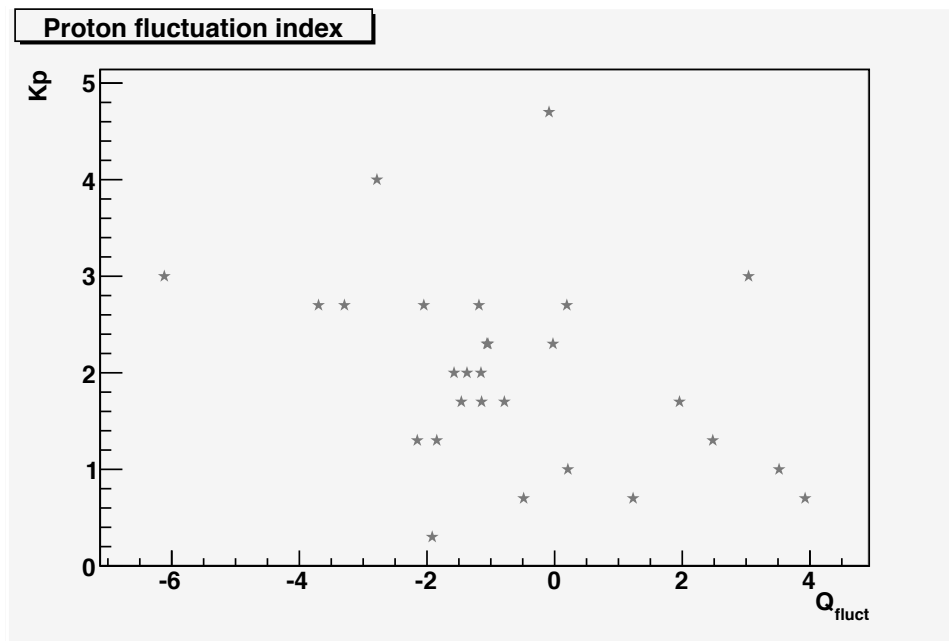


Figure 3.29: Proton flux fluctuation index versus the planetary geomagnetic activity index K_P for the period 18h00 UT June 8 1998 to 3h00 UT June 12 1998.

in the geomagnetic field until they are re-absorbed.

During quiet space weather conditions the secondary flux is kept constant by the equilibrium between their creation and subsequent re-absorption. The correspondence between the occurrence of magnetic disturbances and secondary flux decrease, resulting from the present work, indicates that magnetic disturbances break this equilibrium diminishing the ability of the Earth's magnetic field to trap secondaries, which thus can escape the magnetic bottle more easily than usual.

Chapter 4

Construction of the AMS-02 detector

The main AMS mission aims at the installation of a more sophisticated detector, AMS-02, on the International Space Station (ISS) (Figure 4.1) for a three-year data taking period. The new detector has been built on the basis of the experience gathered by means of the AMS-01 precursor flight.

In particular, AMS-02 incorporates a more powerful spectrometer, and more complete and redundant particle identification, as shown in Figure 4.3. The core of the AMS-02 detector is a spectrometer consisting of a Silicon Tracker inserted in the inner bore of a superconducting magnet, which extends the rigidity range for

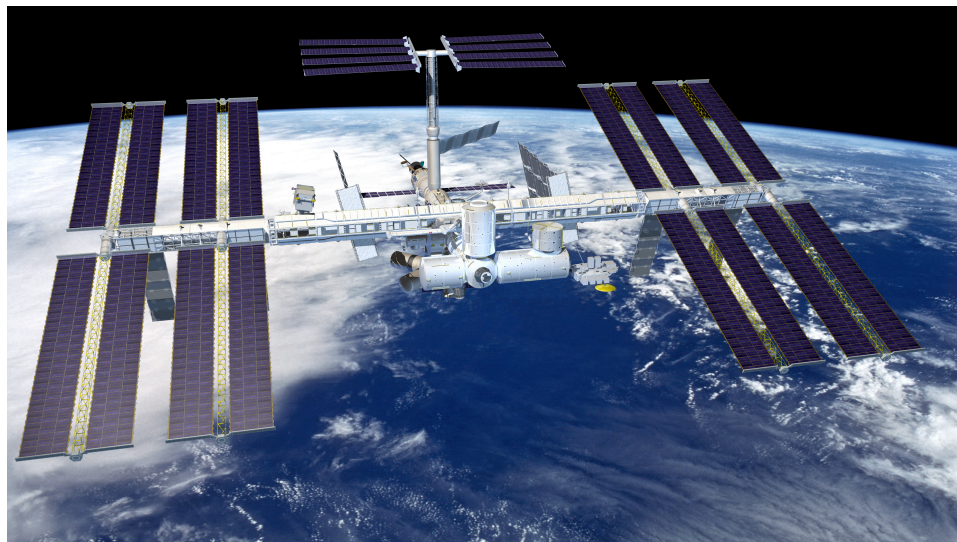


Figure 4.1: Computer-generated artist's rendering of the completely assembled International Space Station with the AMS-02 detector installed on it.

charged particles up to the multi-TV region.

Two scintillator hodoscopes located respectively on top and bottom of the magnetic spectrometer compose the Time Of Flight (TOF) system, providing the main trigger to the whole AMS-02 detector together with particle velocity and charge measurements. A Ring Imaging Cherenkov detector (RICH), situated below the spectrometer, will give further velocity and charge measurements. A Transition Radiation Detector (TRD) and an Electromagnetic Calorimeter (ECal) respectively placed on the very top and bottom of the apparatus will allow the separation between light and heavy particles. Finally accurate knowledge of the AMS-02 detector will be ensured by a Star Tracker [104], an imaging optical instrument able to autonomously recognize a stellar field and to calculate its own orientation with respect to an inertial frame.

The design and construction of the AMS-02 have started soon after the completion of the AMS-01 mission. Currently all the sub-detectors, support and service structures and most of the electronics have been completed and delivered to the AMS assembly facility at the CERN Preveessin site (at the border between France and Switzerland). The Superconducting Magnet is expected for the Spring 2008. Dry assembly activities have started since last Autumn in order to gather experience for the final assembly of the detector which will be performed in the next months. Then the AMS-02 detector will undergo thermo-vacuum tests at the ESTEC facility in the Netherlands, before being shipped to NASA Kennedy Space Center waiting for the launch to the ISS during one of the future Space Shuttle missions.

4.1 The AMS-02 Magnet

The magnet system [105] consists of superconducting coils, a superfluid helium vessel and a cryogenic system, all enclosed in a toroidal vacuum tank with inner diameter of 1.1 m, outer diameter of 2.7 m and height 0.9 m (Figure 4.2).

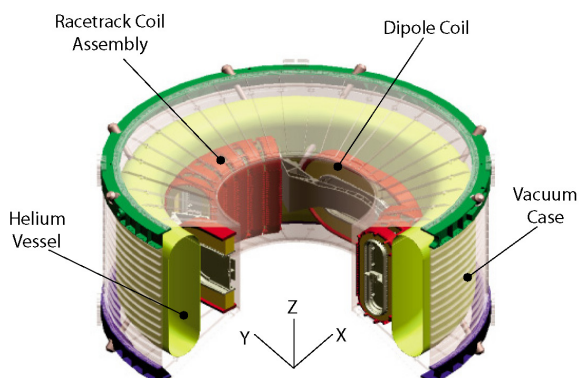


Figure 4.2: The AMS-02 magnet system. Also shown is the AMS reference axis.

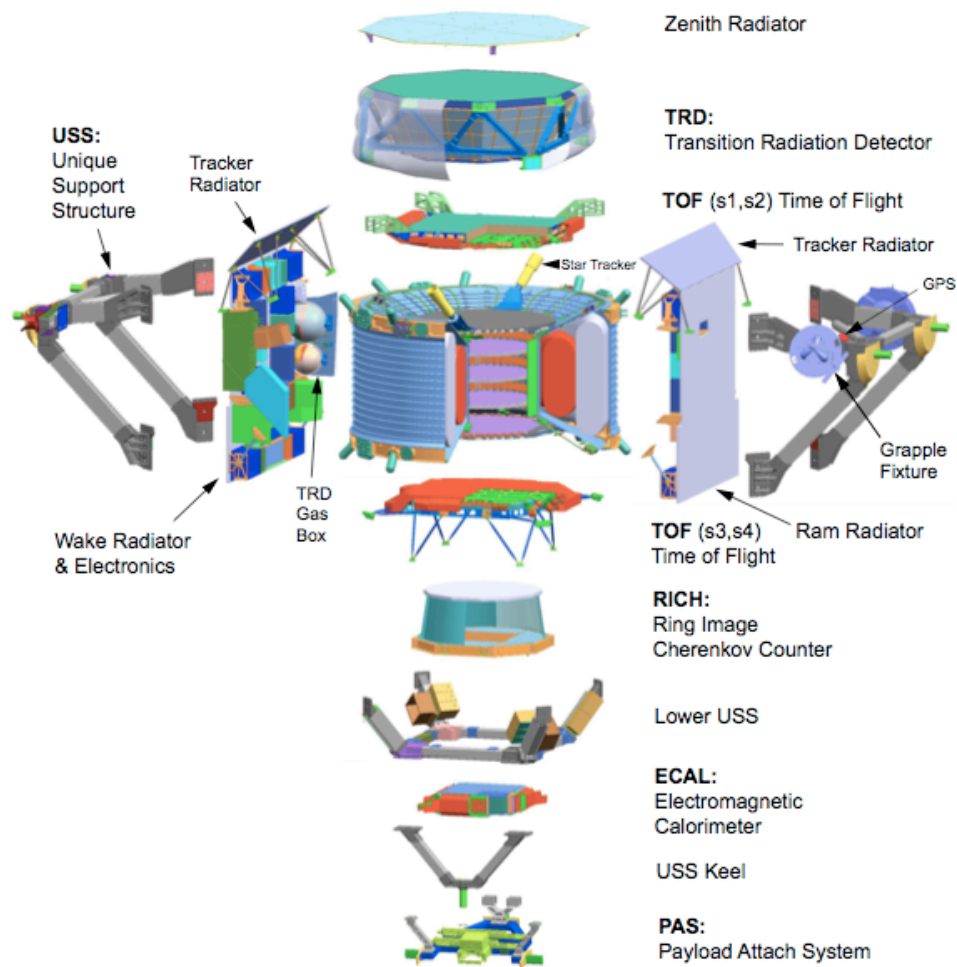


Figure 4.3: Exploded view of the AMS-02 detector.

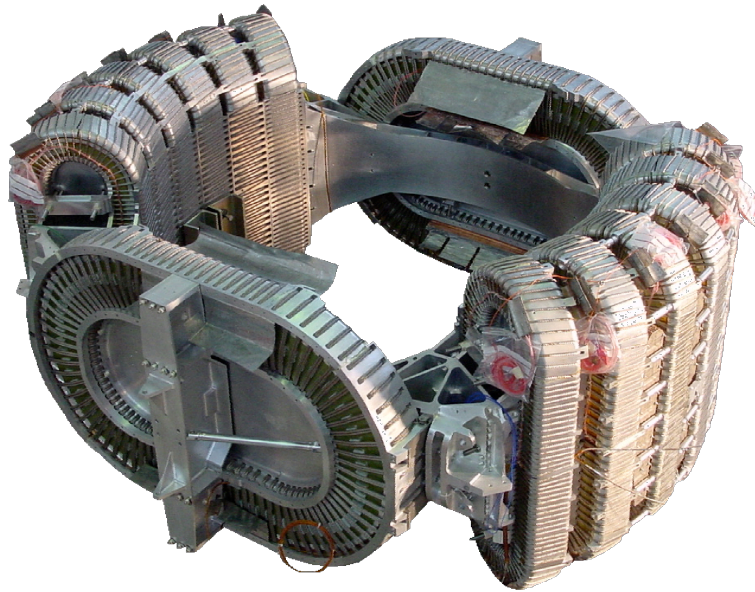


Figure 4.4: Picture of the superconducting coils assembled in the magic ring configuration.

The coils, made of multifilamentary Niobium-Titanium wire, are arranged in a magic ring configuration (Figure 4.4). The two dipole coils generate the main dipolar field parallel to the AMS X-axis (Figure 4.2). The twelve racetrack coils have been introduced to minimize the stray field and the magnetic dipole moment of the overall system. Reducing the dipole moment is crucial to avoid an undesirable torque on the ISS resulting from the interaction with the Earth magnetic field. Reducing the stray field is critical to protect the astronaut's life saving system during excursions in the vicinity of AMS-02. With the chosen configuration the flux return coils also contribute to increase the magnitude of the overall dipolar field.

The magnet operates at a temperature of 1.8 K, cooled by superfluid helium (He II) stored into the vessel. It will be launched at the operating temperature with the vessel full of 2500 litres of He II, sufficient to ensure the magnet functionality for at least three years. The choice of superfluid helium with respect to normal liquid helium has been driven by the limited available volume and by the peculiar conditions in space. In fact He II has a higher specific latent heat and density, which gives a useful endurance benefit, and it does not undergo thermal stratification in zero gravity, allowing to keep the system isothermal.

At nominal current (459 A) the coils produce a central field of 0.9 Tesla, resulting in a bending power Bl^2 of 0.86 Tesla m². Together with the improved Tracker performance, this will lead to an almost ten-fold improvement of the AMS-02 rigidity resolution (Figure 4.11) with respect to the AMS-01 performance (Figures 2.5 and 2.6). The magnet will be charged in space by an on-board power

supply and then operated in persistent mode, that is once the current has reached the nominal value a superconducting switch is closed and the current will continue to circulate without attenuation in the superconducting loop.

The construction of the AMS-02 magnet system is in its final stage and is expected to be completed by the Spring 2008.

4.2 The AMS-02 Silicon Tracker

The Silicon Tracker [106] is composed by eight layers of double-sided silicon sensors installed on five planes of an ultra-light support structure made of Aluminum honeycomb and carbon fiber foils. A carbon fiber cylindrical shell supports the planes 2 to 4, located in the inner bore of the magnet, constituting the Inner Tracker (Figure 4.5). Two carbon fiber conical flanges support the exterior planes 1 and 5 respectively. With respect to the AMS-01 configuration, the number of silicon layers has been increased from 6 to 8 by suppressing one internal plane and equipping both sides of the remaining three inner planes. The inner planes have a diameter of 1 m, while the outer planes have a diameter of 1.4 m.

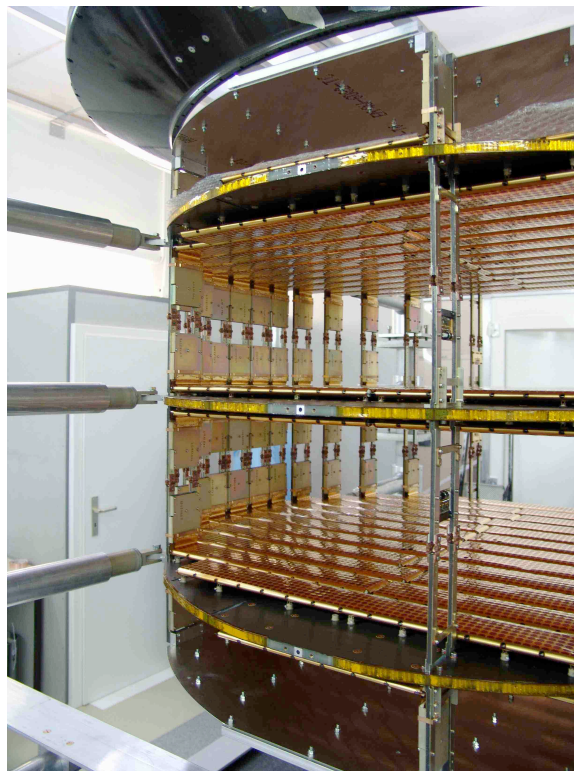


Figure 4.5: A picture of the three inner planes and the upper conical flange on the assembly jig.

The presence of the superconducting magnet requires an active cooling system for the Tracker, which is provided by a set of evaporator loop connected to radiators facing the deep space.

With AMS-01 it was found that the carbon fiber Tracker support structure is stable at the $15\ \mu\text{m}$ level, but excursions up to $30\ \mu\text{m}$ occurred in correlation to the thermal conditions following changes in the spacecraft attitude [21]. Thus a Tracker Alignment System (TAS) [107] has been introduced in the AMS-02 setup. The TAS provides optically generated signals in the eight silicon layers that mimic straight tracks, in order to trace changes in the tracker geometry with a position and angular accuracy better than $5\ \mu\text{m}$ and $2\ \mu\text{rad}$ respectively. This allows arc minute precision pointing of weak astrophysical sources, useful for photon detection.

The AMS-02 silicon sensors

The high modularity, low voltage levels ($< 100\ \text{V}$) and gas-free operation make them very well suited for operation of silicon sensor in space. Silicon microstrip detectors, originally designed for colliding beam experiments, have been adapted to meet the AMS requirements. Since AMS-02 relies completely on the Silicon Tracker to get the tracking information, a large surface area and higher inter-strip capacitance is needed. The major challenges were to maintain the required mechanical precision and low-noise performance in the large scale application [108].

The AMS-02 Silicon Tracker make use of n-type, high resistivity ($> 6\ \text{k}\Omega$) sensors biased with the punch-through technique [108]. The strip and metalization layout is shown in Figure 4.6. The influence of surface charge on the position

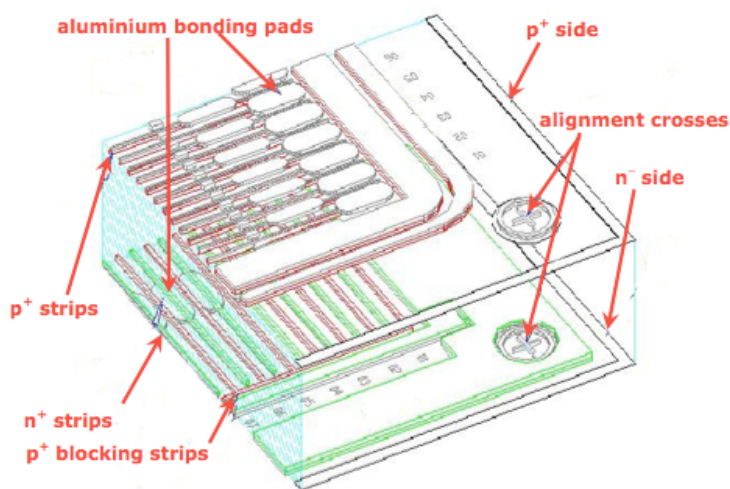


Figure 4.6: Layout of the AMS-02 double-sided silicon micro-strip sensor.

measurement obtained from the ohmic side is minimized implanting p^+ blocking strips on the n-side. The sensor design uses capacitive charge coupling with implantation (readout) strip pitches of 27.5 (110) μm for the p-side and 104 (208) μm for the n-side. The finer pitch p-side strips measure the bending coordinate and the orthogonal n-side strips measure the not bending coordinate.

The ionization loss of singly charged particles traversing the fully depleted, reverse-biased 300 ± 10 μm thick sensor is described by a Landau distribution. The peak energy loss of a singly charged, minimum ionizing particle at normal incidence produces 22,000 electron-hole pairs. The opposite sign charge carriers drift rapidly ($10 - 25$ ns) in the electric field to the two surfaces (p/n) where the accumulated charge on metallized strips is fed to the front-end electronics. The position of the particle is determined by the relative signal levels observed at the readout strip positions. At the single sensor level, the position resolution depends on the sampling pitch and the signal-to-noise performance.

Production of the AMS-02 silicon ladders

The silicon sensors are arranged in 192 modules (ladders) of variable number of sensors (7 to 15) in order to match the circular geometry of the supporting planes. The ladder main components are shown in Figure 4.7.

The silicon sensors are glued on a metalized upilex film (long kapton), which

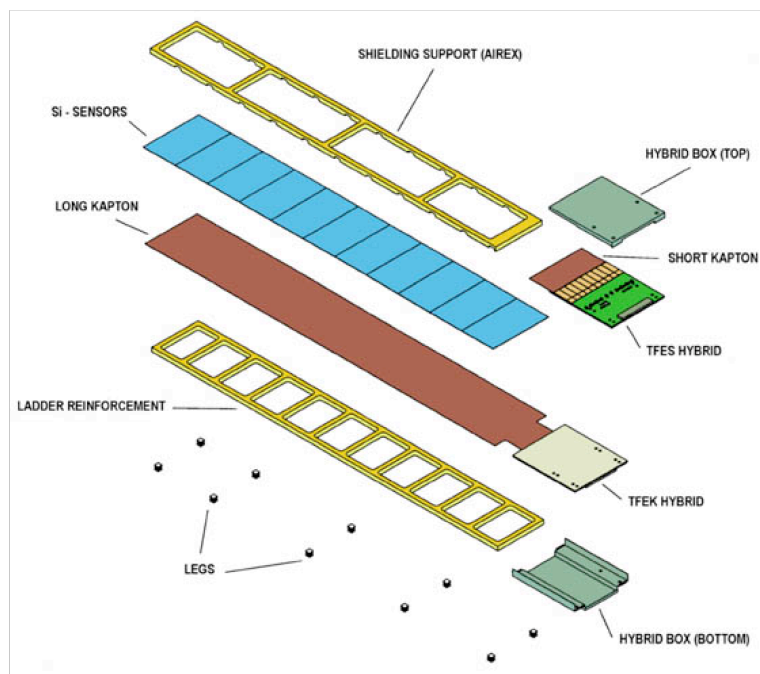


Figure 4.7: Exploded view of the silicon ladder.

serves as routing cable to bring the n-side signals to the n-side front-end electronics (TFES hybrid). A shorter metalized upilex film (short kapton) joins the p-side strip, connected by means of ultrasonic bonding, to the p-side front-end electronics (TFEK hybrid).

A foam supporting reinforcement (ladder reinforcement) is glued on the bottom side of the long kapton. The exposed side of the ladder reinforcement is covered by a thin layer of carbon fiber, on which are glued small aluminum frames (legs). The legs contain a screw fixation hole to fix the module on the tracker supporting planes. The front-end hybrids are mounted back-to-back and enclosed in an aluminum box. The surface of the hybrid box is treated to make it conductive.

A second foam structure (shielding support) is glued on top of the silicon sensors to protect the n-side bonding wires. Then the ladder is wrapped in an electromagnetic shielding, consisting of a doubly-metalized upilex film, which is electrically connected to the hybrid box.

The ladder production has been organized in three assembly lines: DPNC-University of Geneva, INFN-Perugia (Italy) and an industrial firm in Italy (G&A Engineering). For the massive production most of the ladder assembly, consisting in the assembly of silicon sensors with kapton cables, hybrids and reinforcement, was performed in Italy, while DPNC-University of Geneva took care of the ladder completion (legs gluing, hybrid box mounting and shielding wrapping), reparation (if needed) and integration onto the support planes.

The principal goals of the ladder fabrication has been to guarantee a systematic precision for the relative alignment of the silicon sensors better than $5 \mu\text{m}$, and minimize the performance degradation due to handling and ultra-sonic bonding.

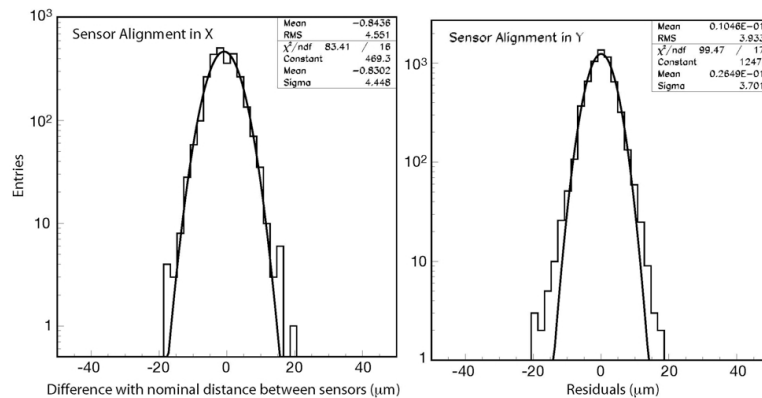


Figure 4.8: Assembly precision of 125 AMS-02 ladders. Left panel: Distribution of the measured differences of the distance between adjacent sensors and the nominal distance ($640 \mu\text{m}$ including $40 \mu\text{m}$ gap between sensors). Right panel: Residual distribution of the sensor positions about the line fits defining the ladder axis parallel to the magnetic field (Pictures from W. Burger).

The alignment precision was provided by the mechanical precision of the jigs (1 to 2 μm) and the precision of the sensor cut ($< 5 \mu\text{m}$). The results of metrology measurement of the sensor alignment for 125 (out of 192) AMS-02 ladders are shown in Figure 4.8. The mean misalignment is less than 1 μm , random alignment variations are less than 5 μm in both directions.

A particular effort has been made to maintain the low noise by passivation of the silicon and by optimization of the ladder assembly procedure. During the production phase each ladder has undergone an extensive series of electrical tests to verify that the ladder noise level and response to signal met the AMS-02 requirements. The electrical tests consisted in ladder calibration and measurement of the ladder response to a radioactive source after each assembly step.

The resulting single channel noise distribution of all flight ladders in the inner Tracker is shown in Figure 4.9. It presents a large improvement with respect to the AMS-01 silicon ladders noise level (Figure 2.7). With a cut of 5 ADC counts defining a high noise level, only 1.6% of the bending direction channels and 3.4% in the non bending direction are to be considered noisy.

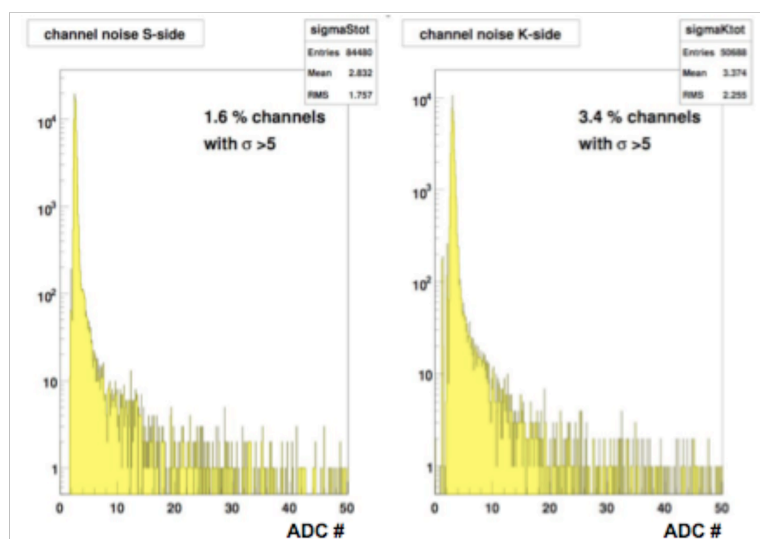


Figure 4.9: Noise level of the 142 ladders composing the Inner Tracker for the p-side (left panel) and n-side (right panel) channels. A channel is considered noisy when the channel noise, σ , is above 5 ADC counts (Picture from Ph. Azzarello).

Ladders which did not meet the alignment and performance requirements were considered for reparation, which has consisted in hybrid, silicon sensor or short kapton replacement depending on the noticed problem. In total 59 ladders have undergone reparation, of which 56 were successfully repaired and could be reintegrated into the assembly line.

In total about 220 ladders have been produced, of which 90% fulfill the AMS-02

quality requirements. With the alignment precision within $5 \mu\text{m}$ and with less than 5% noisy channels on p- and n-side, the AMS-02 silicon ladders are of excellent quality.

Supervision, quality control and traceability of the overall production activities have been ensured by a database, where all the information is stored concerning the components used, the tests performed and the operators on a ladder by ladder level.

AMS-02 Tracker performances

An extensive series of tests has been performed to verify the performance of the AMS-02 Silicon Tracker. Beside the bench tests on the ladder by ladder level, beam tests with minimum ionizing particles, light ions and heavy ions have been carried out.

A measurement of the position resolution was provided by a dedicated setup consisting of a reference telescope composed of four single-sided silicon sensors with $50 \mu\text{m}$ pitch readout and an AMS-02 prototype ladder. The detectors were placed in a 120 GeV muon beam at CERN [109]. The tracking resolution measured is $\sim 10 \mu\text{m}$ in the bending direction and $30 \mu\text{m}$ in the orthogonal direction (Figure 4.10). The expected rigidity resolution for protons and He nuclei is shown in Figure 4.11.

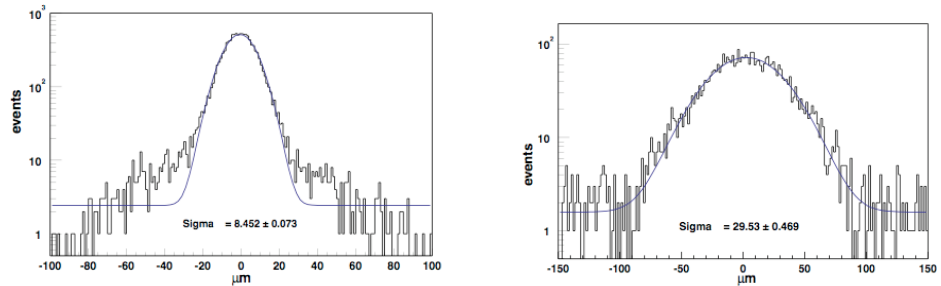


Figure 4.10: Residual distribution of hits on the AMS-02 prototype ladder with respect to the position expected from the reference telescope, for the p-side (left panel) and the n-side (right panel), which in the AMS detector will measure the bending and not bending coordinates respectively (From Ref. [109]).

The measurement of the specific energy loss, $dE/dx \propto Z^2$, in the silicon allows the measurement of the particle absolute charge and hence the identification of nuclei. To study the AMS-02 ladder response to light and heavy ions, six ladders were exposed to an ion beam at CERN in October 2003. A fragmentation beam was produced with primary indium ions impinging with an energy of 135 GeV/A on a beryllium target. The fragmentation ions were selected according to their A/Z ratio, and different data samples, corresponding to $A/Z = 1$, $A/Z = 2$ and $A/Z = 2.25$, were collected. An independent measurement of the ion charge was

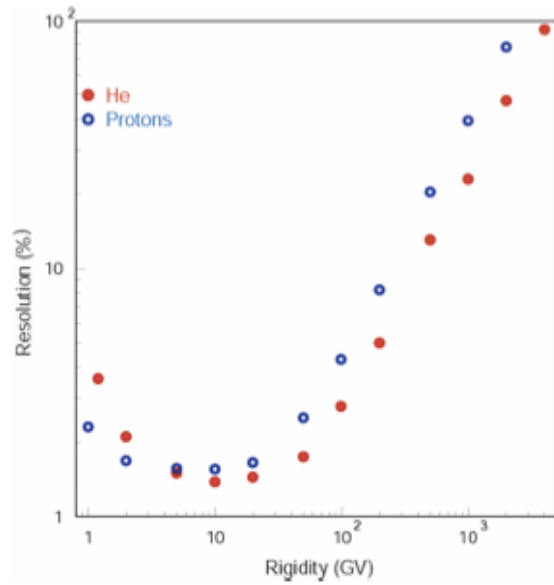


Figure 4.11: Silicon Tracker expected rigidity resolution for protons and He nuclei (From Ref. [21]).

also performed by the prototype AMS-02 RICH detector (see Section 4.6). The silicon ladder Z measurement allowed to distinguish ion species up to $Z = 25$ with the n-side (Figure 4.12) and up to $Z = 16$ with the p-side [110].

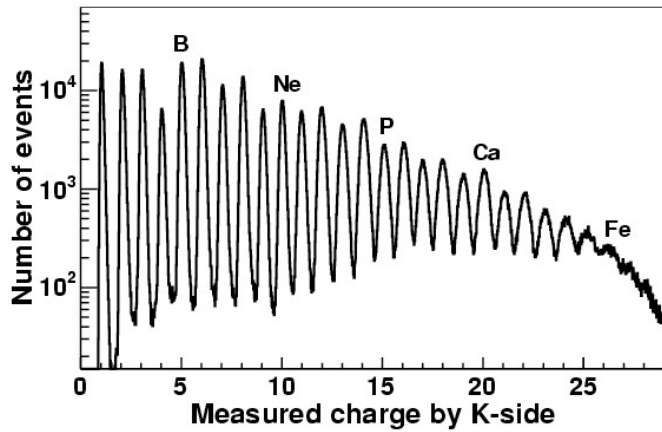


Figure 4.12: Combined Z measurements for 4 or more ladders on the n-side (From Ref. [110]).

The feasibility of measuring converted photons with the Silicon Tracker, detecting the e^+e^- pair produced in the material upstream of the detector, has been

studied exposing a subset of silicon ladders, disposed in a configuration similar to the AMS-02 Silicon Tracker, and a subset of the electromagnetic calorimeter were exposed to electrons of momentum ranging from 1 to 10 GeV at the CERN PS T7 line beam.

The test has demonstrated the capability of the AMS-02 Silicon Tracker to measure converted photons with an energy resolution of 1.5% and angular resolution, σ_{68} , defined by the angular distance from the incoming beam that contains 68% of the events, of 0.8° [111].

AMS-02 Tracker integration

When ladders equipping a full Tracker layer were completely assembled, they were installed on the corresponding support plane, which had been previously equipped with cooling bars. The ladder hybrids are mounted on carbon fiber-metal cooling bars (Figure 4.13) connected to evaporator cooling loops, which evacuate the heat generated by the front-end electronics to the exterior through the radiator panels.

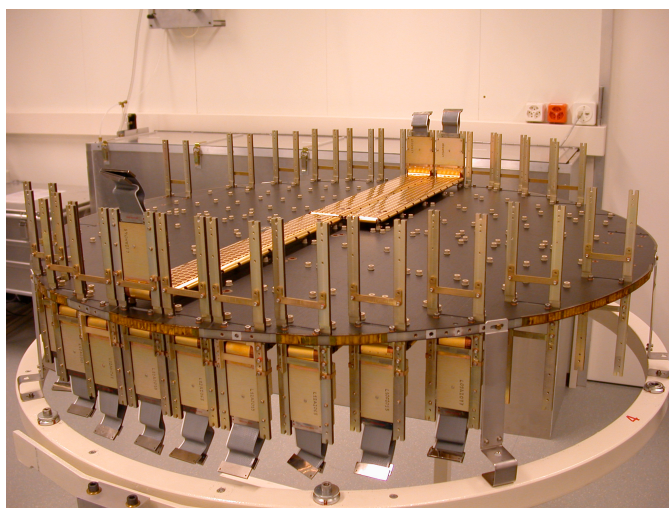


Figure 4.13: One of the inner planes (plane 5) of the Silicon Tracker equipped with cooling bars, being completed with ladders.

After completion of a layer a complete series of calibration tests was performed on the ladders to ensure that their quality did not degrade during integration.

The silicon layer assembly started in September 2003, the three inner planes were completed at the beginning of 2006, and soon after the assembly of the Inner Tracker could start. During the assembly the three planes were supported by an integration jig (Figure 4.5), which allowed the positioning of the planes at the correct distance.

Then the cooling bars of adjacent planes were connected. The flat cables, linking the front-end electronics to the electronics board, were attached to the hybrids

and functional electric tests were performed to verify all connections. Thermal and magnetic field sensors have been installed in the Inner Tracker volume. Finally the Tracker supporting shell and the conical flanges were mounted and the two inner cooling loops were installed on the cooling bars of layers 2 and 7. Meanwhile the assembly of the two outer planes proceeded with ladder integration, installation of the two outer cooling loops, one on each plane, and cabling.

In September 2007 the Inner Tracker and the two completed outer planes, equipped with flight cables and cooling loops, have been the first AMS-02 sub-detectors delivered to the AMS assembly cleanroom at CERN, where an integration trial of the AMS-02 detector started soon after (Figures 4.14 and 4.15).



Figure 4.14: AMS-02 assembly trial: insertion of the Inner Tracker in the magnet vacuum case.

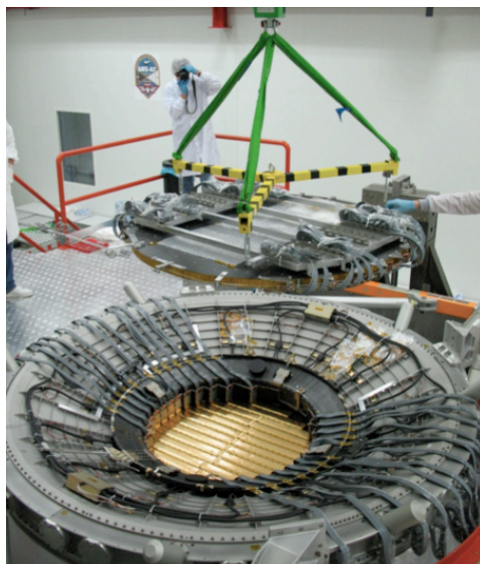


Figure 4.15: AMS-02 assembly trial: positioning of the upper Silicon Tracker outer plane.

4.3 The AMS-02 Counter System

The Counter System, consisting of veto counters and a Time Of Flight (TOF) system [112], provides the trigger signals to the AMS-02 detector. Moreover the TOF system measures the particle velocity and arrival direction, as well as the absolute charge.

The veto counters

In order to reject particles entering the detector laterally outside the main geometrical acceptance, an AntiCoincidence Counter (ACC) [113] is placed between the inner bore of the magnet vacuum tank and the Silicon Tracker supporting shell. The ACC consists of scintillator panels connected at both ends to magnetic field insensitive PhotoMultiplier Tubes (PMTs), placed on the upper and lower conical flanges, through optical fibers. The tests performed have shown that the ACC exhibits a high degree of homogeneity and high efficiency.

The Time Of Flight hodoscopes

The TOF system has been designed to provide a fast trigger for charged particles and converted photons, selecting at the trigger level particles within the main AMS acceptance. It also measures the particle velocity including the discrimination between upward and downward going particles.

The geometrical acceptance of the TOF is $0.4 \text{ m}^2 \text{ sr}$, maximizing the sensitivity of the spectrometer for antimatter search.

The TOF system is composed of four roughly circular planes of scintillator paddles, one pair of planes placed above the magnet (upper TOF) and one pair below (lower TOF). Each plane has a sensitive area of 1.2 m^2 and within one plane the paddles are overlapped by 0.5 cm to avoid geometrical inefficiencies. The paddles in the two adjacent planes are orthogonal (Figure 4.16). Each paddle is instrumented at both ends with PMTs, connected through light guides. The TOF



Figure 4.16: Picture of a pair of TOF planes.

counters operate in the magnet stray field. Since the PMTs are sensitive to magnetic field and the use of a magnetic shielding is prevented by weight restrictions, a suitable PMT has been chosen, which can operate under these conditions provided that is aligned within 45° of the field direction. The light guides have been adapted to respect this alignment condition (see Figure 4.16).

The TOF counters have been tested in ion beams at CERN in 2002 and again in 2003. Four scintillators (C1, C2, C3 and C4) with different configuration of the light guides have been exposed to a 158 GeV/A ion beam. The ion charge has been well measured by all counters. The measurement obtained with the worst light guide configuration is shown in Figure (4.18). The time of flight measurement between two counters is shown in Figure (4.17) as a function of the particle charge, from which is inferred a time resolution for the TOF system of the order of 130 ps for MIPs.

The TOF system has been completed and delivered to the AMS assembly facility. In November 2007, after the insertion of the Tracker into the magnet vacuum case, an integration trial of the upper TOF on top of the spectrometer has been performed.

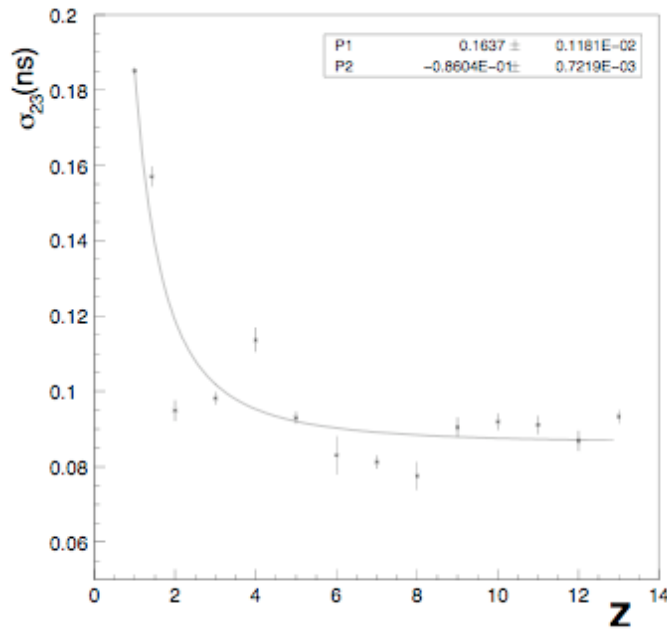


Figure 4.17: Time of Flight resolution, $\simeq \sigma_{23}$, obtained with the TOF counters C2 and C3 versus particle charge. The time resolution for the four TOF planes is $\simeq \sigma_{23}/\sqrt{2}$ (From Ref. [112]).

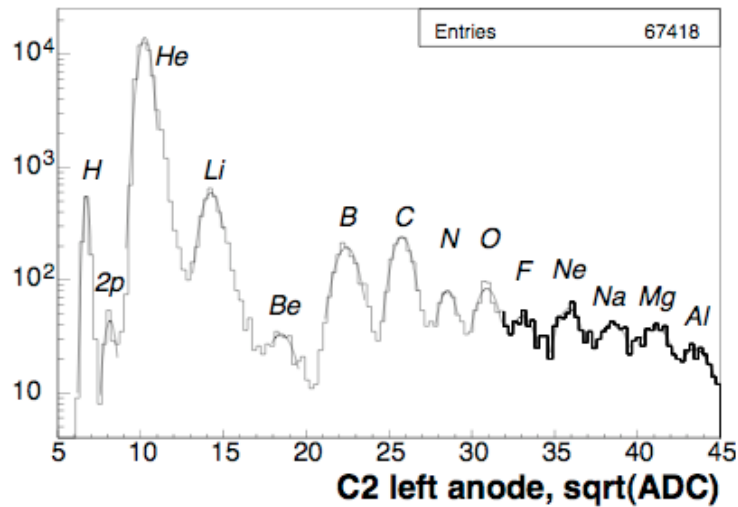


Figure 4.18: The square root of the integrated charge measured with the left anode of the TOF counter C2 shows peaks corresponding to different beam particles (From Ref. [112]).

4.4 The Transition Radiation Detector

The TRD [114] detects the transition radiation (TR) X-rays emitted by highly relativistic ($E/m > 10^3$) charged particles upon changes in the index of refraction of the traversed medium. Protons up to 300 GV can be distinguished from positrons of the same rigidity recording both the direct ionisation signal from the primary particle and the TR photons.

The AMS-02 TRD design makes use of a 0.06 g/cm^3 polypropylene/polyethylene fiber fleece as radiator. Straw tubes, filled with a Xe : CO₂ (80%:20%) gas mixture and operated at 1600 V, serve as radiation detectors. Since the probability for a particle to emit a TR photon at a single interface is very small (10^{-2}) a multilayer structure is needed.

The AMS-02 TRD has the shape of a conical octagon of 2 m diameter. In total 328 modules, each containing 16 straw tubes, of lengths between 0.8 and 2 m, are arranged in 20 layers, each with 20 mm of $10 \mu\text{m}$ fiber fleece. The lower and upper four layers are oriented parallel to the AMS-02 magnetic field while the middle 12 layers run perpendicular to provide 3D tracking.

To verify the proton rejection power of the AMS-02 TRD design a full 20 layer prototype was built with 40 modules of 40 cm length arranged in two adjacent towers. The setup has been exposed to particle beams in the CERN T9, X7 and H6 lines. The particle trigger with scintillator panels and threshold or differential Cerenkov counters allowed the selection of electrons, muons and pions up to

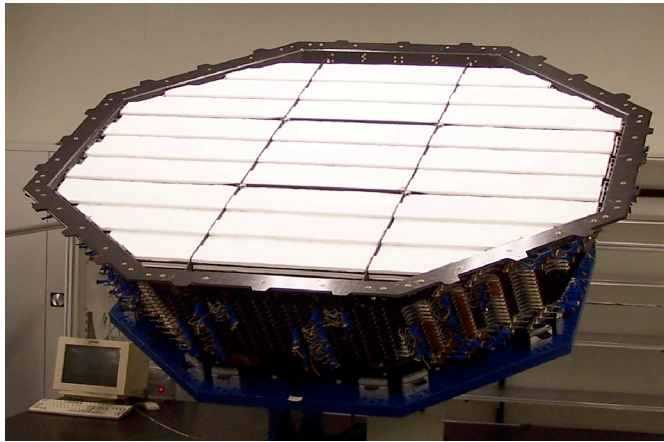


Figure 4.19: Picture of the AMS-02 Transition Radiation Detector.

100 GeV and protons up to 250 GeV.

To analyze the test beam results, protons are separated from electrons with a likelihood algorithm [114], which uses as probability density the tube energy spectra measured from clean single track events (Figure 4.20). The proton rejection factor is determined as the inverse proton selection efficiency with a likelihood cut set for an electron efficiency of 90%. For proton beam energies between 15 and 250 GeV the proton rejection is above 100, in agreement with MonteCarlo simulation (Figure 4.21).

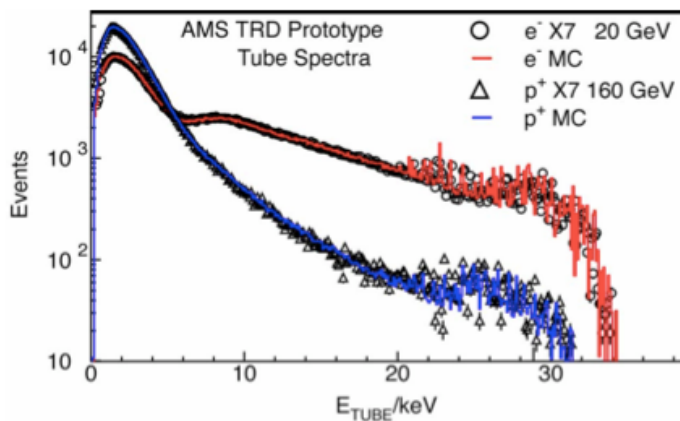


Figure 4.20: Energy spectra for all tubes on the reconstructed track for preselected clean single track events. Proton and electron GEANT3 MonteCarlo simulations are shown together with the test beam measurements. The proton spectrum follows a typical Landau distribution, while the electron spectrum has in addition a transition radiation component, clearly visible above 6 keV (From Ref. [114]).

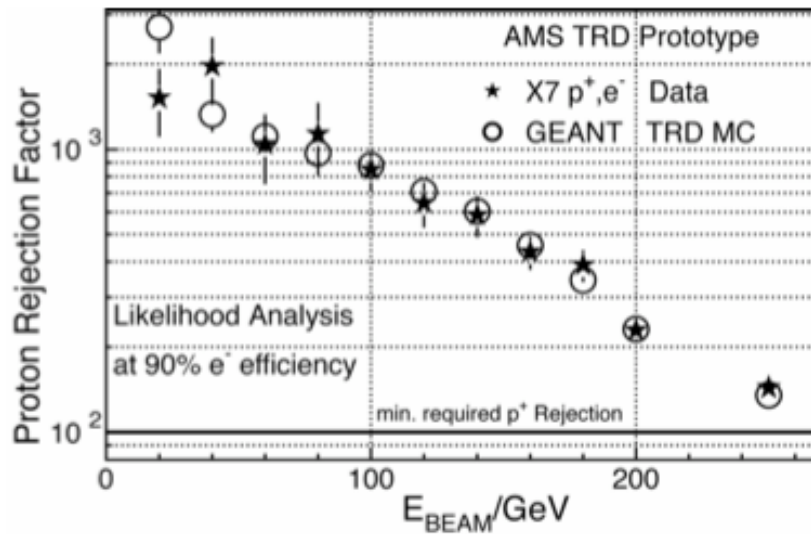


Figure 4.21: AMS-02 TRD proton rejection factor (From Ref. [114]).

The TRD detector has been completed and shipped to CERN, where an integration trial on top of the upper TOF has been performed successfully in late November 2007.

4.5 The Electromagnetic calorimeter

The AMS-02 Electromagnetic Calorimeter (ECAL) [115] is a fine grain lead-scintillating fiber sampling calorimeter, that allows precise three-dimensional imaging of the longitudinal and lateral shower development, providing high ($\geq 10^6$) electron/hadron discrimination in combination with the other AMS-02 sub-detectors. The light collection system and electronics are optimized for the calorimeter to measure electromagnetic particles over a wide energy range, from GeV up to TeV.

The ECAL consists of a lead/scintillating fiber sandwich with an active area of $648 \times 648 \text{ mm}^2$ and a thickness of 166.5 mm (Figure 4.22). The calorimeter is composed of nine superlayers, each made of eleven 1 mm thick grooved lead foils interleaved with 1 mm diameter scintillating fibers and glued together with epoxy (Figure 4.23).

In total nine superlayers, summing up to 17 radiation lengths, are stacked one of top of the other with the fibers alternatively oriented along the X and Y directions.

The fibers are read out, on one end only, by photomultipliers with four anode pads, each covering an active area of $9 \times 9 \text{ mm}^2$, corresponding to 35 fibers defined as a cell (Figure 4.23). In total the ECAL is subdivided into 1296 cells, allowing a sampling of the longitudinal shower profile by 18 independent measurements.

Since the residual magnetic field at the ECAL location can reach up to 20 Gauss,

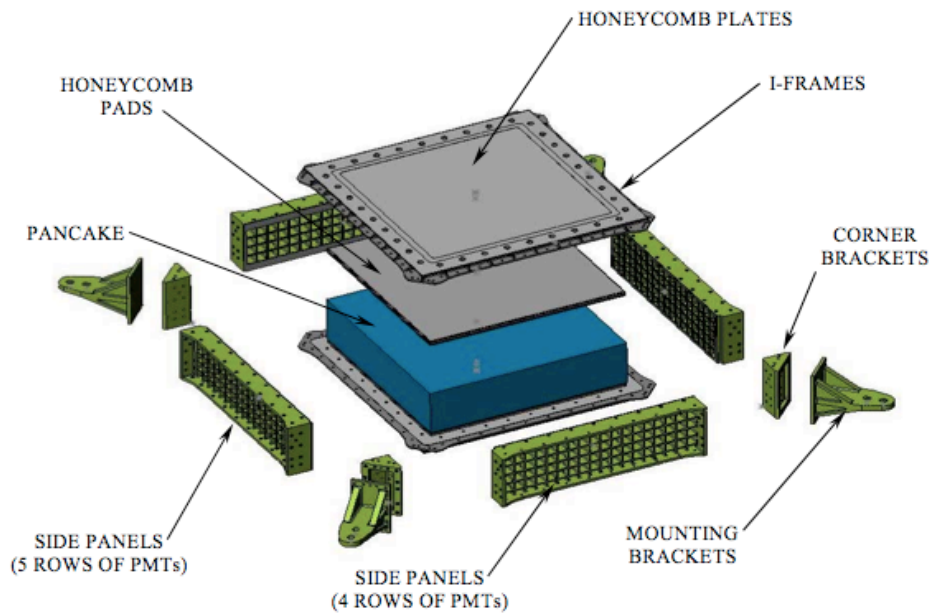


Figure 4.22: Exploded view of the AMS-02 Electromagnetic calorimeter.

each PMT is surrounded by a magnetic shield which also contains light guides and the front-end electronics.

The ECAL support structure is made of an aluminum alloy and consists of four lateral panels which contain the PMTs and top and bottom honeycomb plates (Figure 4.22). It has been designed to minimum weight with a first resonance frequency above 50 Hz, a capability to face accelerations up to 14 g in any direction and thermal insulation limiting the temperature gradient to $\pm 5^\circ \text{C}$ (the external temperature can range from -40°C to $+50^\circ \text{C}$).

The ECAL qualification model has been exposed to the CERN SPS beam line H6A with muons, 120 GeV protons and antiprotons, and 3 to 180 GeV e^\pm . The calorimeter was partially equipped with PMTs covering a $126 \times 126 \text{ mm}^2$ corner

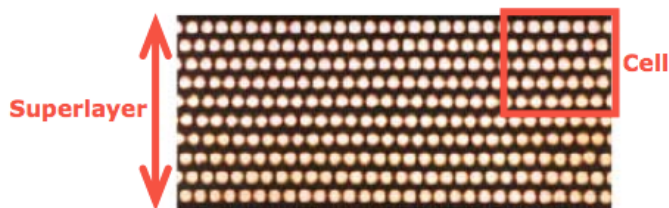


Figure 4.23: Cross section of the ECAL lead-fiber-glue composite structure.

of the ECAL. The calorimeter energy resolution estimate obtained for electrons entering the detector at the center of the equipped region is shown in the left panel of Figure 4.24 as a function of the beam energy.

The energy resolution is well parametrized by

$$\sigma(E)/E = (10.2 \pm 0.3)\% / \sqrt{E(\text{GeV})} \oplus (2.3 \pm 0.1)\%$$

The energy measurement and resolution were also studied for electrons impinging the detector near the edges. For e^\pm entering the ECAL at distances less than 30 mm from the edge, corrections greater than 20% have to be applied to the measured energy.

The angular resolution, defined by the angular distance from the incoming beam that contains 68% of the events, as a function of the incoming electron is well described by

$$\Delta\theta_{68\%} = (8.0 \pm 0.1) / \sqrt{E(\text{GeV})} \oplus (0.57 \pm 0.04)^\circ$$

as shown in the right panel of Figure 4.24. The electron/proton rejection power has been studied with a neural network method, which takes into account the main shower shape characteristics (Figure 4.25). The rejection power is improved of a factor 10 by combining Tracker and ECAL information to determine the energy/momentum ratio. Adding the Transition Radiation Detector information leads to an overall proton rejection power of 10^6 for the AMS-02 detector.

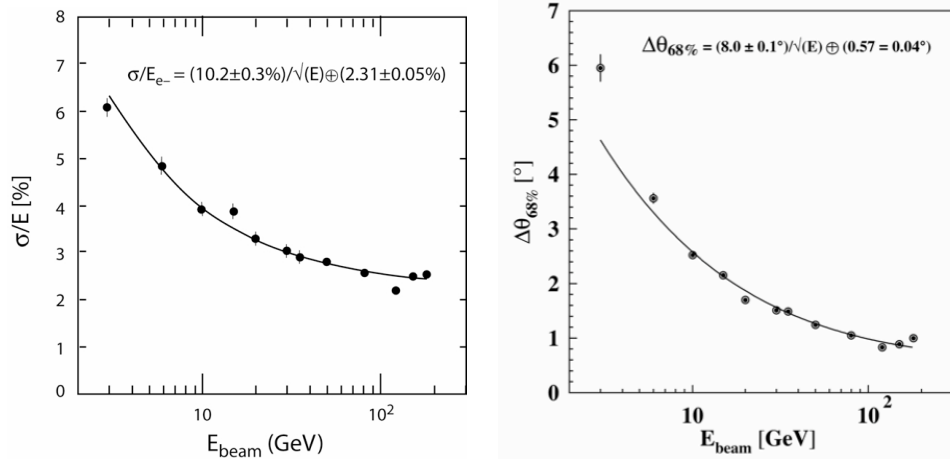


Figure 4.24: ECAL energy resolution (left panel) and angular resolution (right panel) versus electron energy (From Ref. [115]).

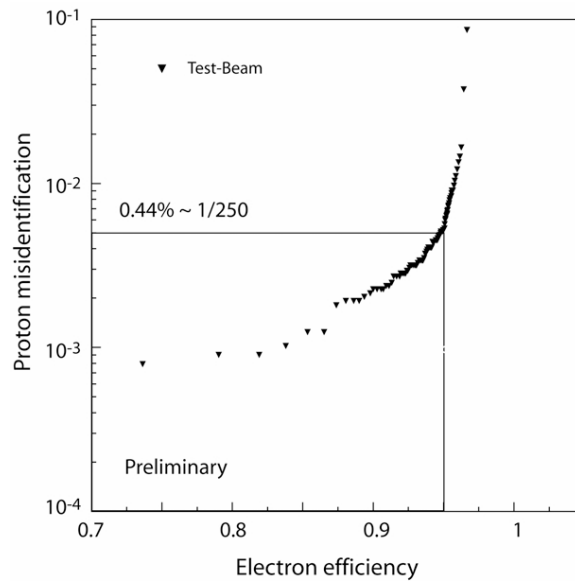


Figure 4.25: Misidentification of 120 GeV protons versus 50 GeV electron efficiency after a neural network selection (E/p matching not included). For an electron efficiency of 0.95, the proton rejection is about 250 (From Ref. [115]).

4.6 The Ring Imaging Cerenkov detector

Isotopic mass separation over a wide range of energies requires, in addition to an accurate momentum measurement, a velocity determination with low relative uncertainty, since $\Delta m/m = (\Delta p/p) \oplus \gamma^2(\Delta\beta/\beta)$. In the AMS-02 detector, the momentum is determined from the information provided by the Silicon Tracker with a relative accuracy of $\sim 1\%$ over a wide range of energies. This entails an error of the same order on the mass of the particle so, in order to match this uncertainty, the velocity has to be measured with a relative accuracy of about 0.1%. For this purpose a Ring Imaging Cerenkov (RICH) detector has been included in the AMS-02 setup [116], between the lower TOF and the ECAL.

The RICH design has been driven by a set of constraints imposed by the operation in space, which imposes as usual size, weight and power consumption restrictions, the operation in the magnet stray field, amounting to ~ 300 G, and minimization of material in front of the ECAL.

The RICH has a truncated conical shape with a top radius of 60 cm, a bottom radius of 67 cm and a total height of 60.5 cm (Figure 4.26), covering 80% of the AMS-02 magnet acceptance. A supporting plane on the top holds a 3 cm thick layer of dielectric material (radiator). The lower plane, which has a 64×64 cm² square central hole to let particles go unaffected to the ECAL, supports an array of 680 light guides and multipixel photomultipliers as well as the front-end electron-

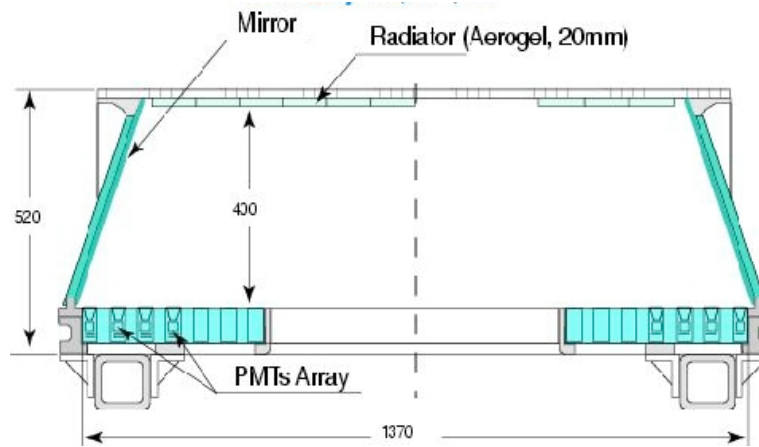


Figure 4.26: Drawing of the AMS-02 Ring Imaging Cerenkov detector.

ics. A thin film of reflecting coating is deposited on the inner surface of the conical shape (mirror), in order to increase the device acceptance.

A charged particle coming from above first crosses the radiator creating a cone of Cerenkov radiation. The properties of this radiation cone depend on the velocity of the charged particle, β , and the refractive index of the material, $n(\omega)$. For a particle of charge Ze , the half opening angle of the cone is given by $\cos \theta = 1/\beta n(\omega)$, resulting in a threshold velocity $\beta_{min} = 1/n(\omega)$ for Cerenkov radiation emission. Since the number of radiated photons in a frequency range $d\omega$ for a traversed length dx in the radiator is proportional to $Z^2 \sin \theta$, the RICH also provides an independent estimation of the charge of the incoming particle.

The radiator is made of aerogel tiles with refractive index 1.05, and sodium fluoride (NaF) tiles in the center, covering an area of $34 \times 34 \text{ cm}^2$, in order to increase the photon detection efficiency for those particles falling upon the central hole of the detection plane. Indeed NaF has a higher refractive index ($n = 1.336$) which gives a wider Cerenkov cone.

Most of the photons go directly to the PMTs in the lower plane. The others are reflected on the lateral mirror before reaching the PMTs. From the spatial coordinates of the photomultiplier pixels and the direction of the incoming particle, the Cerenkov cone is reconstructed and the velocity of the particle determined. Upward going particles do not leave this signal and thus can be unambiguously discriminated.

In order to validate the design of the AMS-02 RICH, a prototype consisting of an array of 9×11 cells similar to those of the final setup were constructed, and exposed to cosmic muons and fragmented ions from CERN SPS beams in 2002 and 2003 [117]. An adjustable supporting structure was used to test different sets of aerogels at variable expansion heights. The setup was completed by a Silicon Tracker ladder telescope placed upstream in the beam, two multiwire proportional

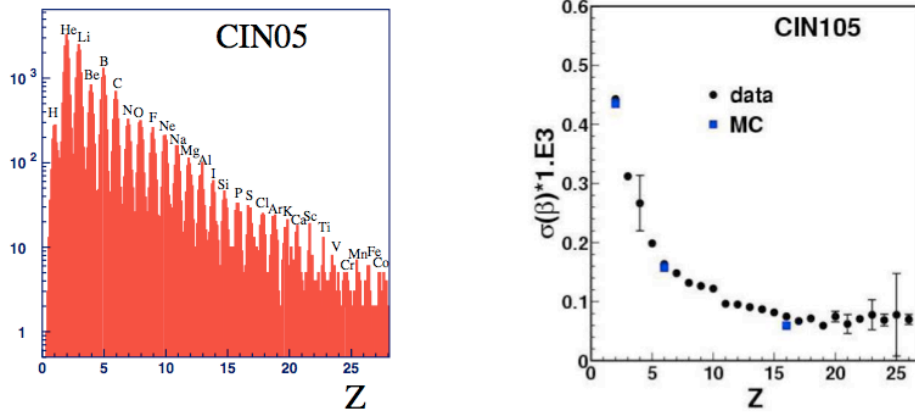


Figure 4.27: Performance of the CIN05 aerogel exposed to a 158 GeV fragmented Indium beam. Left panel: Measured distribution of charges (From Ref. [116]). Right panel: Dependence of the velocity resolution on the charge of the nuclei (From Ref. [117]).

chambers and scintillator counters.

One of the key issue of test was the evaluation of the aerogel samples in order to make a choice for the final radiator construction. The required criteria for a good candidate were a high photon yield and accurate velocity and charge measurements. These tests led to the choice of a 1.05 refractive index aerogel produced by the Catalysis Institute of Novosibirsk (CIN05).

The velocity resolution scales with the detected signal, and hence with the squared charge. For helium a relative accuracy of $\Delta\beta/\beta \simeq 0.45 \times 10^{-3}$ is obtained for the CIN05 aerogel (Figure 4.27). Charge peaks up to iron were identified, with a resolution around 0.15 for low Z ions together with a systematic uncertainty, scaling with the charge, of 1.2% due to non-uniformities.

Thus, the Silicon Tracker and the RICH identify nuclear charge independently and with comparable resolution, up to iron group nuclei.

Chapter 5

Conclusions

The AMS-01 flight has taken place just two years after the solar minimum of 1996, and in a period of low solar activity level. Only two CME events associated with medium intensity X-ray flares have been observed on June 8th and June 11th respectively (see Appendix C). No extreme solar phenomena have been observed by dedicated detectors in the period from June 2 to June 12 1998. Consequently the geomagnetic and neutron monitor records do not report significant disturbances and variabilities.

While on one side this has been positive for the measurement of cosmic ray composition and energy spectra with the AMS-01 detector, which thus has not been affected by enhanced solar activity, for what concerns the study presented here more subtle effects are expected.

Electron, proton and He nuclei flux variations have been searched in the whole energy range accessible to the AMS-01 detector (100 MeV/n - 200 GeV/n), for the time interval for which suitable AMS-01 data are available (from June 8 to June 12 1998). Systematic variations of cosmic ray fluxes have been observed in the energy range from 100 MeV/n to 30 GeV/n, mainly in the proton channel, correlated to the level of geomagnetic disturbances due to the solar activity. Flux decreases have been observed more frequently than flux increases, the latter being sporadic for He nuclei and even absent for electrons.

The most significant correlation has been observed between the frequency of systematic flux decreases at low energies and the occurrence of magnetic disturbances. It concerns under-cutoff particles, whose flux is kept constant in quiet space weather by a dynamical equilibrium between the creation of secondaries from interaction of primary cosmic rays with the atmosphere, and their subsequent re-absorption.

Since the primary flux over cut-off is found to have no systematic fluctuations, the observed correlation must be due to a diminished ability of the Earth's magnetic field to trap secondaries. It appears that during magnetic disturbances, more particles escape from the geomagnetic bottle than usual.

More data taken over a longer period will be needed to fully understand these

subtle effects and observe the influence of more violent solar phenomena. The PAMELA and AMS-02 missions will provide these data.

The AMS-02 detector, which is currently at the final stage of its construction, will be installed on the International Space Station during the rising phase of the solar cycle, at solar activity conditions similar to those at which the AMS-01 detector has operated 10 years ago. Thus this analysis might be used as seed for further studies on cosmic ray variations with the final AMS detector.

The improved performance of the AMS-02 detector and its capability of detecting gamma rays will allow the refinement of cosmic ray spectra measurements and to perform more sensitive dark matter and antimatter searches, with respect to those carried out with the prototype detector, AMS-01.

The AMS-02 subdetectors have been completed and delivered to the AMS assembly facility at CERN. The detector integration will start in Spring 2008. Afterwards the final space qualification tests will be performed on the completely assembled detector at ESTEC. Finally, by the end of 2008, the AMS-02 detector will be shipped to the NASA Kennedy Space Center, ready for installation on the International Space Station during one of the last Space Shuttle missions.

Appendix A

Catalog of cosmic-ray flux fluctuation events

Electron, proton and He nuclei flux fluctuation events found for the time period 17h53 UT June 8 1998 to 2h36 UT June 12 1998 are listed in Section A.1, A.2 and A.3 respectively.

In each list are reported the following quantities:

`nbins` number of kinetic energy bins involved in the fluctuation event out of the five bins in which the range 0.1 – 30 GeV/n has been divided;

`up/dw` flag specifying the type of fluctuation: `up` for positive and `dw` for negative;

`Likelihood` fluctuation likelihood defined as the product of the probabilities (3.24)/(3.25) for positive/negative fluctuations of the kinetic energy bins involved in the fluctuation event;

`Dtime (s)` actual counting number sampling time;

`date_enter` date at which the measurement has started, corresponds to the entry time in an actual counting number sampling geomagnetic sector;

`date_exit` date at which the measurement has ended, corresponds to the exit time from the above-mentioned geomagnetic sector.

A.1 Electron flux fluctuation occurrences

<code>nbins</code>	<code>Likelihood</code>	<code>Dtime (s)</code>	<code>date_enter</code>	<code>date_exit</code>
3dw	1.96463e-21	44	Jun 9 02:07:02	Jun 9 02:07:46
3dw	4.51094e-20	41	Jun 11 03:08:52	Jun 11 03:09:33

A.2 Proton flux fluctuation occurrences

nbins	Likelihood	Dtime (s)		date_enter		date_exit
3up	2.15474e-13	36	Jun	8 17:53:14	Jun	8 17:53:50
3dw	7.63959e-280	64	Jun	8 18:11:00	Jun	8 18:12:04
3up	2.00812e-182	54	Jun	8 18:18:15	Jun	8 18:19:09
3up	2.63477e-142	55	Jun	8 18:19:09	Jun	8 18:20:04
3up	2.60526e-123	35	Jun	8 18:22:26	Jun	8 18:23:21
3dw	1.63501e-182	53	Jun	8 18:57:36	Jun	8 18:58:29
3dw	1.84206e-108	72	Jun	8 18:58:29	Jun	8 18:59:41
3dw	2.48576e-108	8	Jun	8 19:01:45	Jun	8 19:01:53
3dw	0	61	Jun	8 19:01:53	Jun	8 19:02:54
3dw	0	60	Jun	8 19:02:54	Jun	8 19:03:54
3dw	1.50805e-257	77	Jun	8 19:40:21	Jun	8 19:41:38
3up	2.2792e-171	48	Jun	8 19:54:17	Jun	8 19:55:05
5up	9.03424e-319	46	Jun	8 19:56:49	Jun	8 19:57:35
5up	1.00797e-302	104	Jun	8 19:59:10	Jun	8 20:00:54
5up	4.62171e-158	103	Jun	8 20:01:02	Jun	8 20:02:45
3up	1.05982e-164	79	Jun	8 20:29:21	Jun	8 20:30:40
3up	0	71	Jun	8 20:30:40	Jun	8 20:31:51
5dw	1.56612e-179	62	Jun	8 20:31:54	Jun	8 20:32:56
3dw	1.08991e-52	106	Jun	8 20:53:57	Jun	8 20:55:43
3dw	5.30863e-84	34	Jun	8 21:13:03	Jun	8 21:13:37
3dw	1.47747e-101	78	Jun	8 21:15:11	Jun	8 21:16:29
5dw	1.49488e-127	25	Jun	8 21:17:13	Jun	8 21:17:37
3up	1.76908e-43	14	Jun	8 21:30:48	Jun	8 21:31:02
3up	1.49273e-22	62	Jun	8 21:49:45	Jun	8 21:50:47
3up	3.3468e-94	63	Jun	8 22:04:13	Jun	8 22:05:16
4up	8.60238e-165	60	Jun	8 22:05:16	Jun	8 22:06:16
4up	0	56	Jun	8 22:06:16	Jun	8 22:07:12
4up	4.11558e-248	43	Jun	8 22:10:02	Jun	8 22:10:45
4up	1.07236e-192	54	Jun	8 22:10:45	Jun	8 22:11:39
3dw	0	59	Jun	8 22:13:41	Jun	8 22:14:40
3dw	2.39047e-199	78	Jun	8 22:14:51	Jun	8 22:16:09
3dw	1.57832e-227	66	Jun	8 22:16:09	Jun	8 22:17:15
3dw	1.1868e-19	74	Jun	8 22:34:29	Jun	8 22:35:43
4up	3.22993e-235	111	Jun	8 22:44:27	Jun	8 22:46:18
3up	1.62492e-99	104	Jun	8 22:46:26	Jun	8 22:48:10
4dw	4.01549e-140	82	Jun	8 22:48:14	Jun	8 22:49:36
5dw	0	39	Jun	8 22:52:04	Jun	8 22:52:42
3up	3.28155e-28	48	Jun	8 22:52:42	Jun	8 22:53:30
4up	1.07577e-33	41	Jun	8 22:54:55	Jun	8 22:55:36
3dw	0	48	Jun	8 23:03:40	Jun	8 23:04:28
3dw	3.37996e-190	71	Jun	8 23:05:09	Jun	8 23:06:20

3dw	3.37321e-246	34	Jun	8	23:33:33	Jun	8	23:34:07
4dw	1.62702e-195	46	Jun	8	23:35:54	Jun	8	23:36:40
5dw	2.91877e-139	63	Jun	8	23:36:40	Jun	8	23:37:43
4dw	3.71687e-28	18	Jun	8	23:39:20	Jun	8	23:39:38
5dw	7.23929e-156	51	Jun	8	23:40:29	Jun	8	23:41:20
3up	6.05653e-34	51	Jun	8	23:42:11	Jun	8	23:43:02
5dw	6.66528e-158	51	Jun	8	23:43:02	Jun	8	23:43:53
5dw	2.37695e-319	31	Jun	8	23:43:53	Jun	8	23:44:24
3dw	4.27848e-116	82	Jun	8	23:48:03	Jun	8	23:49:25
3dw	0	58	Jun	8	23:49:25	Jun	8	23:50:23
3up	1.92785e-28	109	Jun	8	23:58:17	Jun	9	00:00:06
3up	3.89326e-17	71	Jun	9	00:00:06	Jun	9	00:01:17
4up	8.10172e-29	37	Jun	9	00:01:17	Jun	9	00:01:54
3up	1.31888e-174	41	Jun	9	00:23:26	Jun	9	00:24:07
5up	2.73207e-37	52	Jun	9	00:25:36	Jun	9	00:26:28
5dw	1.43353e-60	29	Jun	9	00:26:28	Jun	9	00:27:16
4up	1.72684e-28	46	Jun	9	00:27:16	Jun	9	00:28:02
4up	2.42177e-31	42	Jun	9	00:28:02	Jun	9	00:28:44
4up	1.61165e-25	40	Jun	9	00:29:25	Jun	9	00:30:05
3up	1.17525e-23	41	Jun	9	00:30:05	Jun	9	00:30:46
4up	9.96116e-70	71	Jun	9	00:35:41	Jun	9	00:36:52
4up	0	58	Jun	9	01:07:49	Jun	9	01:08:47
4dw	1.26303e-111	61	Jun	9	01:10:08	Jun	9	01:11:09
5dw	2.55606e-42	46	Jun	9	01:12:10	Jun	9	01:12:56
4dw	4.69698e-67	51	Jun	9	01:12:56	Jun	9	01:13:47
5up	1.77155e-88	51	Jun	9	01:14:37	Jun	9	01:15:28
4up	5.61256e-34	54	Jun	9	01:16:18	Jun	9	01:17:12
4up	0	44	Jun	9	01:20:47	Jun	9	01:21:31
4up	3.12487e-28	52	Jun	9	01:59:51	Jun	9	02:00:43
4up	3.59201e-22	48	Jun	9	02:00:43	Jun	9	02:01:31
4dw	7.83132e-32	28	Jun	9	02:01:51	Jun	9	02:02:19
3up	1.80839e-24	45	Jun	9	02:02:19	Jun	9	02:03:04
5dw	7.95479e-122	45	Jun	9	02:03:49	Jun	9	02:04:34
3up	3.7185e-15	47	Jun	9	02:04:34	Jun	9	02:05:21
5dw	9.54015e-209	50	Jun	9	02:05:21	Jun	9	02:06:11
5dw	0	51	Jun	9	02:06:11	Jun	9	02:07:02
5dw	0	44	Jun	9	02:07:02	Jun	9	02:07:46
3dw	0	72	Jun	9	02:09:06	Jun	9	02:10:18
3up	1.36174e-28	54	Jun	9	02:25:46	Jun	9	02:26:40
3up	0	54	Jun	9	02:44:24	Jun	9	02:45:18
4up	1.8036e-50	42	Jun	9	02:47:53	Jun	9	02:48:35
3up	1.93519e-26	10	Jun	9	02:48:35	Jun	9	02:48:45
4up	9.90191e-112	52	Jun	9	02:48:45	Jun	9	02:49:37
4up	3.66348e-130	56	Jun	9	02:49:37	Jun	9	02:50:33

4up	1.95361e-138	60	Jun	9	02:50:33	Jun	9	02:51:33
3up	0	45	Jun	9	02:53:05	Jun	9	02:53:50
4dw	1.16176e-47	31	Jun	9	03:30:10	Jun	9	03:30:41
4up	2.05453e-254	55	Jun	9	03:33:46	Jun	9	03:34:41
5dw	0	37	Jun	9	03:36:41	Jun	9	03:37:18
3dw	7.66135e-264	39	Jun	9	03:43:36	Jun	9	03:44:15
4dw	4.84749e-179	81	Jun	9	03:45:02	Jun	9	03:46:23
3dw	7.11403e-174	52	Jun	9	04:15:41	Jun	9	04:16:33
3up	1.10012e-74	51	Jun	9	04:18:26	Jun	9	04:19:19
3dw	3.07781e-178	56	Jun	9	04:22:01	Jun	9	04:22:57
3up	1.36447e-44	26	Jun	9	04:24:37	Jun	9	04:25:03
3dw	4.09998e-46	102	Jun	9	04:38:13	Jun	9	04:39:55
5dw	3.59687e-85	29	Jun	9	05:05:59	Jun	9	05:06:28
3up	6.63701e-118	56	Jun	9	05:11:46	Jun	9	05:12:42
3dw	1.64285e-22	39	Jun	9	05:33:42	Jun	9	05:34:21
3dw	4.32622e-263	57	Jun	9	05:50:28	Jun	9	05:51:25
3dw	2.36564e-194	57	Jun	9	05:51:25	Jun	9	05:52:22
3dw	1.52603e-156	55	Jun	9	05:52:22	Jun	9	05:53:17
3dw	8.30298e-168	58	Jun	9	05:53:17	Jun	9	05:54:15
5dw	0	49	Jun	9	05:55:27	Jun	9	05:56:16
3dw	0	71	Jun	9	05:57:22	Jun	9	05:58:33
3dw	1.38551e-138	12	Jun	9	05:58:33	Jun	9	05:58:45
3dw	4.14307e-41	55	Jun	9	06:12:05	Jun	9	06:13:00
3up	2.12615e-31	74	Jun	9	09:17:15	Jun	9	09:18:29
3dw	5.07083e-32	105	Jun	9	10:00:08	Jun	9	10:01:53
3dw	2.86922e-16	126	Jun	9	10:44:44	Jun	9	10:46:50
3dw	2.34342e-32	115	Jun	9	11:39:57	Jun	9	11:41:52
3dw	2.49432e-14	26	Jun	9	12:23:00	Jun	9	12:23:26
3up	5.4666e-20	107	Jun	9	14:42:49	Jun	9	14:44:36
3dw	2.06857e-31	88	Jun	9	15:17:18	Jun	9	15:18:46
5dw	8.64458e-263	63	Jun	9	15:35:01	Jun	9	15:36:04
5dw	1.24607e-167	13	Jun	9	15:38:04	Jun	9	15:38:17
5dw	0	40	Jun	9	15:38:45	Jun	9	15:39:25
4dw	7.05947e-99	58	Jun	9	15:39:46	Jun	9	15:40:44
5dw	0	80	Jun	9	16:23:29	Jun	9	16:24:49
4dw	2.84636e-239	79	Jun	9	16:24:49	Jun	9	16:26:08
3dw	1.57019e-19	91	Jun	9	16:49:10	Jun	9	16:50:41
4dw	6.64753e-181	57	Jun	9	17:07:52	Jun	9	17:08:49
5dw	0	38	Jun	9	17:11:05	Jun	9	17:12:04
5dw	0	58	Jun	9	17:12:04	Jun	9	17:13:02
5dw	4.95502e-91	33	Jun	9	17:13:02	Jun	9	17:13:56
5dw	3.16154e-269	42	Jun	9	17:14:53	Jun	9	17:15:35
5dw	1.81166e-81	41	Jun	9	17:16:52	Jun	9	17:17:33
4dw	2.53763e-135	57	Jun	9	17:17:33	Jun	9	17:18:30

4dw	1.14403e-230	41	Jun	9	17:18:51	Jun	9	17:19:32
4dw	1.20752e-22	10	Jun	9	20:16:15	Jun	9	20:16:25
5dw	6.03428e-138	38	Jun	9	20:16:25	Jun	9	20:17:03
5dw	3.81772e-169	4	Jun	9	20:23:53	Jun	9	20:23:57
5dw	4.41774e-135	77	Jun	9	20:27:43	Jun	9	20:29:00
3dw	1.09211e-68	72	Jun	9	20:59:52	Jun	9	21:01:04
3up	2.48523e-130	12	Jun	9	21:02:19	Jun	9	21:02:31
3up	1.09144e-180	42	Jun	9	21:05:42	Jun	9	21:06:23
3up	2.40353e-204	54	Jun	9	21:07:17	Jun	9	21:08:11
3dw	0	60	Jun	9	21:12:02	Jun	9	21:13:02
3dw	2.9758e-18	32	Jun	9	21:27:18	Jun	9	21:27:50
5dw	3.3113e-241	43	Jun	9	21:46:38	Jun	9	21:47:21
4up	7.78717e-34	57	Jun	9	21:49:42	Jun	9	21:50:39
5dw	3.27103e-143	46	Jun	9	21:51:30	Jun	9	21:52:16
4up	1.45416e-38	42	Jun	9	21:52:16	Jun	9	21:52:58
3up	6.60042e-17	41	Jun	9	21:52:58	Jun	9	21:53:39
3dw	5.1065e-196	74	Jun	9	22:32:14	Jun	9	22:33:28
4dw	1.12883e-64	6	Jun	9	22:34:39	Jun	9	22:34:45
3dw	6.91886e-49	67	Jun	9	22:34:45	Jun	9	22:35:52
4up	1.75942e-125	61	Jun	9	22:35:52	Jun	9	22:36:53
4up	2.75862e-218	58	Jun	9	22:36:53	Jun	9	22:37:51
3up	4.67577e-87	21	Jun	9	22:37:51	Jun	9	22:38:12
4up	9.22049e-56	13	Jun	9	22:38:32	Jun	9	22:38:45
5up	1.35824e-172	52	Jun	9	22:38:45	Jun	9	22:39:37
3dw	3.2073e-138	12	Jun	9	22:46:15	Jun	9	22:46:27
3dw	0	82	Jun	9	22:47:33	Jun	9	22:48:55
4dw	3.75854e-234	106	Jun	9	22:49:02	Jun	9	22:50:48
5up	3.71797e-46	107	Jun	9	22:58:38	Jun	9	23:00:25
3dw	1.64106e-85	105	Jun	9	23:18:18	Jun	9	23:20:03
3up	2.81973e-243	51	Jun	9	23:21:28	Jun	9	23:22:19
5dw	0	52	Jun	9	23:22:50	Jun	9	23:23:42
3up	1.03899e-25	49	Jun	9	23:24:35	Jun	9	23:25:24
5dw	0	46	Jun	9	23:25:24	Jun	9	23:26:09
5dw	7.14888e-310	40	Jun	9	23:26:09	Jun	9	23:26:49
5dw	0	41	Jun	9	23:26:49	Jun	9	23:27:30
5dw	0	39	Jun	9	23:27:30	Jun	9	23:28:09
5dw	0	39	Jun	9	23:28:09	Jun	9	23:28:48
5dw	2.60824e-290	41	Jun	9	23:28:48	Jun	9	23:29:29
4up	1.20494e-25	41	Jun	9	23:29:29	Jun	9	23:30:10
5dw	3.10093e-222	43	Jun	9	23:30:10	Jun	9	23:30:53
3up	1.08606e-20	50	Jun	9	23:31:40	Jun	9	23:32:30
4dw	1.54702e-76	97	Jun	9	23:39:53	Jun	9	23:41:30
3dw	1.64866e-284	79	Jun	10	00:05:50	Jun	10	00:07:09
3dw	0	58	Jun	10	00:07:20	Jun	10	00:08:18

5dw	2.26193e-225	62	Jun 10	00:08:18	Jun 10	00:09:20
4up	5.36297e-79	23	Jun 10	00:10:18	Jun 10	00:10:41
5up	1.2454e-91	31	Jun 10	00:10:41	Jun 10	00:11:12
5dw	1.93307e-182	50	Jun 10	00:12:04	Jun 10	00:12:54
5dw	2.50037e-63	9	Jun 10	00:12:54	Jun 10	00:13:03
5dw	1.02347e-121	21	Jun 10	00:13:23	Jun 10	00:13:44
5dw	1.03468e-235	50	Jun 10	00:13:44	Jun 10	00:14:34
5up	1.06052e-131	52	Jun 10	00:14:34	Jun 10	00:15:26
3up	0	58	Jun 10	00:16:21	Jun 10	00:17:19
3up	4.74675e-81	9	Jun 10	00:19:27	Jun 10	00:19:36
3dw	6.7932e-111	57	Jun 10	00:20:57	Jun 10	00:21:54
3up	3.28617e-25	110	Jun 10	00:29:51	Jun 10	00:31:41
5up	2.14648e-49	71	Jun 10	00:31:41	Jun 10	00:32:52
5up	3.35099e-57	38	Jun 10	00:32:52	Jun 10	00:33:30
4dw	5.68249e-87	55	Jun 10	00:54:02	Jun 10	00:54:57
5dw	1.45303e-215	48	Jun 10	00:56:25	Jun 10	00:57:12
4up	1.46594e-29	55	Jun 10	00:57:12	Jun 10	00:58:07
4up	2.70542e-45	51	Jun 10	00:58:07	Jun 10	00:58:58
4up	3.31037e-64	48	Jun 10	00:58:58	Jun 10	00:59:46
4up	1.35639e-44	44	Jun 10	00:59:46	Jun 10	01:00:30
5up	1.82913e-43	45	Jun 10	01:00:30	Jun 10	01:01:15
4up	1.45383e-28	42	Jun 10	01:01:15	Jun 10	01:01:57
4up	2.22712e-31	43	Jun 10	01:01:57	Jun 10	01:02:40
4up	6.6038e-39	44	Jun 10	01:02:40	Jun 10	01:03:24
4up	1.66359e-34	46	Jun 10	01:03:24	Jun 10	01:04:10
4up	1.39903e-31	49	Jun 10	01:04:10	Jun 10	01:04:59
4dw	0	72	Jun 10	01:07:56	Jun 10	01:09:08
5dw	4.28712e-176	56	Jun 10	01:42:41	Jun 10	01:43:37
5dw	1.87013e-79	33	Jun 10	01:43:37	Jun 10	01:44:10
4dw	1.01602e-43	19	Jun 10	01:44:10	Jun 10	01:44:29
5dw	9.9345e-84	32	Jun 10	01:44:29	Jun 10	01:45:01
3up	0	70	Jun 10	01:52:01	Jun 10	01:53:11
3up	4.8953e-257	81	Jun 10	01:53:11	Jun 10	01:54:32
4up	0	104	Jun 10	01:54:39	Jun 10	01:56:23
4up	2.62928e-30	53	Jun 10	02:32:10	Jun 10	02:33:03
5dw	1.95453e-318	49	Jun 10	02:34:43	Jun 10	02:35:32
3dw	1.28447e-146	57	Jun 10	03:13:57	Jun 10	03:14:54
3up	4.29837e-74	56	Jun 10	03:15:52	Jun 10	03:16:48
3up	7.34175e-242	52	Jun 10	03:16:48	Jun 10	03:17:40
3up	0	52	Jun 10	03:17:40	Jun 10	03:18:32
5dw	4.08764e-159	24	Jun 10	03:20:49	Jun 10	03:21:13
4up	1.93941e-212	23	Jun 10	03:23:55	Jun 10	03:24:18
4dw	9.2512e-92	57	Jun 10	04:07:54	Jun 10	04:08:51
4dw	6.50123e-136	105	Jun 10	04:17:15	Jun 10	04:19:00

3dw	1.01312e-230	51	Jun 10	04:48:01	Jun 10	04:48:52
3dw	8.87792e-155	56	Jun 10	04:48:52	Jun 10	04:49:48
3dw	4.34529e-84	56	Jun 10	04:49:48	Jun 10	04:50:44
4dw	8.79861e-150	15	Jun 10	06:31:30	Jun 10	06:31:45
5dw	4.31368e-27	137	Jun 10	07:34:56	Jun 10	07:37:13
3up	1.86063e-26	140	Jun 10	08:14:58	Jun 10	08:17:18
5dw	3.93806e-100	76	Jun 10	10:37:50	Jun 10	10:39:06
5dw	2.37862e-73	82	Jun 10	10:40:01	Jun 10	10:41:23
4up	1.32481e-37	48	Jun 10	12:48:30	Jun 10	12:49:18
4up	2.80111e-99	81	Jun 10	13:04:45	Jun 10	13:06:06
4dw	0	77	Jun 10	15:23:08	Jun 10	15:24:25
5dw	6.22234e-271	77	Jun 10	15:24:25	Jun 10	15:25:42
4dw	1.51629e-309	72	Jun 10	16:53:32	Jun 10	16:54:44
4dw	0	39	Jun 10	16:56:43	Jun 10	16:57:22
4dw	0	71	Jun 10	16:57:22	Jun 10	16:58:33
3up	2.59792e-207	28	Jun 10	17:49:15	Jun 10	17:49:43
3dw	0	27	Jun 10	18:31:04	Jun 10	18:31:31
3dw	0	61	Jun 10	18:31:31	Jun 10	18:32:32
3dw	0	60	Jun 10	18:32:32	Jun 10	18:33:32
3dw	0	40	Jun 10	18:33:32	Jun 10	18:34:12
5dw	8.80524e-141	17	Jun 10	20:04:20	Jun 10	20:04:37
3dw	5.00364e-30	64	Jun 10	20:24:01	Jun 10	20:25:05
4dw	6.20693e-57	164	Jun 10	20:25:46	Jun 10	20:28:30
5dw	1.55649e-184	20	Jun 10	20:49:22	Jun 10	20:50:10
3up	3.67643e-12	43	Jun 10	20:50:54	Jun 10	20:51:37
5dw	0	46	Jun 10	20:55:39	Jun 10	20:56:25
5dw	0	50	Jun 10	20:56:25	Jun 10	20:57:15
3dw	5.33238e-34	24	Jun 10	21:30:55	Jun 10	21:31:19
5dw	9.04163e-108	65	Jun 10	21:33:54	Jun 10	21:34:59
3up	1.93675e-128	56	Jun 10	21:35:59	Jun 10	21:36:55
5dw	1.51318e-141	16	Jun 10	21:37:31	Jun 10	21:37:47
5dw	0	54	Jun 10	21:37:47	Jun 10	21:38:41
5up	1.20818e-73	52	Jun 10	21:38:41	Jun 10	21:39:33
4up	2.64594e-50	55	Jun 10	21:39:33	Jun 10	21:40:27
3dw	1.67069e-282	24	Jun 10	21:44:25	Jun 10	21:44:49
3up	7.52797e-14	160	Jun 10	21:59:21	Jun 10	22:02:21
4dw	3.85537e-75	45	Jun 10	22:12:47	Jun 10	22:13:32
5dw	8.5557e-192	53	Jun 10	22:18:23	Jun 10	22:19:16
4dw	2.43576e-58	3	Jun 10	22:20:30	Jun 10	22:20:33
3dw	5.12575e-29	64	Jun 10	22:20:33	Jun 10	22:21:37
5dw	0	31	Jun 10	22:23:37	Jun 10	22:24:08
5dw	1.59233e-112	18	Jun 10	23:17:20	Jun 10	23:17:38
3up	9.27634e-243	57	Jun 10	23:17:59	Jun 10	23:18:56
3up	4.96801e-14	104	Jun 10	23:28:20	Jun 10	23:30:04

3up	1.66362e-30	109	Jun 10	23:30:09	Jun 10	23:31:58
4up	1.07656e-17	107	Jun 10	23:31:58	Jun 10	23:33:45
3up	1.77559e-39	7	Jun 10	23:54:15	Jun 10	23:54:22
5dw	4.66436e-72	30	Jun 10	23:56:15	Jun 10	23:57:05
4dw	2.99246e-103	33	Jun 11	00:39:48	Jun 11	00:40:50
5dw	0	32	Jun 11	01:36:22	Jun 11	01:36:54
5dw	1.15829e-296	35	Jun 11	01:36:54	Jun 11	01:37:29
4up	4.41076e-196	56	Jun 11	02:14:04	Jun 11	02:15:00
3up	0	54	Jun 11	02:15:00	Jun 11	02:15:53
3up	5.66165e-57	51	Jun 11	02:16:45	Jun 11	02:17:36
3up	1.28685e-109	51	Jun 11	02:17:36	Jun 11	02:18:27
3up	7.27712e-171	56	Jun 11	02:19:20	Jun 11	02:20:16
3up	1.29932e-78	64	Jun 11	02:21:14	Jun 11	02:22:18
3up	0	33	Jun 11	02:22:55	Jun 11	02:23:28
3up	1.15775e-296	78	Jun 11	02:23:28	Jun 11	02:24:46
4up	0	45	Jun 11	02:26:16	Jun 11	02:27:01
3up	1.03054e-40	55	Jun 11	03:04:19	Jun 11	03:05:14
3up	8.68274e-50	53	Jun 11	03:05:14	Jun 11	03:06:07
3up	2.45741e-126	54	Jun 11	03:06:07	Jun 11	03:07:01
5dw	0	41	Jun 11	03:08:52	Jun 11	03:09:33
4dw	2.33577e-239	60	Jun 11	03:43:00	Jun 11	03:44:00
3dw	9.94903e-191	59	Jun 11	03:46:10	Jun 11	03:47:09
3up	1.37115e-118	54	Jun 11	03:49:53	Jun 11	03:50:47
4up	2.34893e-168	54	Jun 11	03:50:47	Jun 11	03:51:41
3dw	3.45666e-11	92	Jun 11	04:08:03	Jun 11	04:09:35
5dw	5.61741e-68	79	Jun 11	05:02:55	Jun 11	05:04:14
4dw	0	39	Jun 11	05:21:18	Jun 11	05:21:57
5dw	0	56	Jun 11	05:21:57	Jun 11	05:22:53
4dw	1.99575e-222	26	Jun 11	05:22:53	Jun 11	05:23:19
3dw	1.19286e-132	11	Jun 11	05:28:08	Jun 11	05:28:19
5dw	1.25952e-103	134	Jun 11	09:35:35	Jun 11	09:37:49
5dw	9.54171e-55	43	Jun 11	09:37:49	Jun 11	09:38:32
5up	6.33766e-204	82	Jun 11	11:58:04	Jun 11	11:59:47
4up	3.16119e-286	67	Jun 11	12:01:41	Jun 11	12:02:48
4up	4.6134e-97	81	Jun 11	12:04:21	Jun 11	12:05:42
4up	7.3711e-145	78	Jun 11	12:05:42	Jun 11	12:07:00
4dw	0	78	Jun 11	12:13:16	Jun 11	12:14:34
5dw	6.63722e-101	72	Jun 11	12:55:05	Jun 11	12:56:17
5up	1.15618e-61	33	Jun 11	13:18:08	Jun 11	13:18:41
5up	2.21721e-136	40	Jun 11	13:21:17	Jun 11	13:21:57
4dw	0	67	Jun 11	14:22:50	Jun 11	14:23:57
4up	0	68	Jun 11	14:29:49	Jun 11	14:30:57
5dw	9.70468e-50	63	Jun 11	15:09:12	Jun 11	15:10:15
5dw	4.46684e-263	54	Jun 11	15:50:15	Jun 11	15:51:09

3dw	6.46896e-277	48	Jun	11	17:26:26	Jun	11	17:27:14
3dw	8.27328e-189	71	Jun	11	17:27:14	Jun	11	17:28:25
3dw	1.81911e-258	14	Jun	11	17:31:24	Jun	11	17:31:38
5dw	7.82847e-175	47	Jun	11	18:11:30	Jun	11	18:12:37
5dw	6.85469e-55	46	Jun	11	19:24:16	Jun	11	19:25:02
4dw	6.97697e-303	17	Jun	11	19:43:05	Jun	11	19:43:22
4dw	1.30669e-170	75	Jun	11	19:43:22	Jun	11	19:44:37
5dw	0	17	Jun	11	19:47:15	Jun	11	19:47:32
5dw	0	39	Jun	11	19:58:00	Jun	11	19:58:39
5dw	1.28042e-99	43	Jun	11	20:31:38	Jun	11	20:32:21
4up	1.22753e-158	59	Jun	11	20:33:24	Jun	11	20:34:23
5up	2.58974e-210	54	Jun	11	20:36:12	Jun	11	20:37:06
4up	5.33057e-193	53	Jun	11	20:37:06	Jun	11	20:37:59
3dw	0	31	Jun	11	20:41:54	Jun	11	20:42:25
5up	8.10707e-90	41	Jun	11	20:59:23	Jun	11	21:00:04
5dw	6.33046e-124	82	Jun	11	21:16:13	Jun	11	21:17:35
4up	2.14848e-37	47	Jun	11	21:20:36	Jun	11	21:21:23
5dw	0	31	Jun	11	21:22:16	Jun	11	21:22:47
3dw	0	48	Jun	11	22:01:17	Jun	11	22:02:05
3dw	3.1227e-159	55	Jun	11	22:03:39	Jun	11	22:04:34
5dw	7.67602e-216	17	Jun	11	22:07:11	Jun	11	22:07:28
5dw	0	53	Jun	11	22:07:28	Jun	11	22:08:21
5dw	0	67	Jun	11	22:12:00	Jun	11	22:13:07
5dw	5.2356e-222	40	Jun	11	22:13:07	Jun	11	22:13:47
3up	0	17	Jun	11	22:13:47	Jun	11	22:14:04
5dw	0	44	Jun	11	22:14:04	Jun	11	22:14:48
4dw	0	43	Jun	11	22:14:48	Jun	11	22:15:31
5dw	5.61643e-147	83	Jun	11	22:16:02	Jun	11	22:17:25
3dw	1.81944e-251	34	Jun	11	22:17:25	Jun	11	22:17:59
5dw	0	41	Jun	11	22:49:19	Jun	11	22:50:00
4up	1.86646e-25	58	Jun	11	22:52:24	Jun	11	22:53:22
3up	3.73884e-27	50	Jun	11	22:53:22	Jun	11	22:54:12
4up	3.3816e-37	48	Jun	11	22:54:12	Jun	11	22:55:00
4up	8.59854e-26	41	Jun	11	22:55:43	Jun	11	22:56:24
5dw	0	39	Jun	11	22:57:05	Jun	11	22:57:44
3up	2.5701e-15	39	Jun	11	22:57:44	Jun	11	22:58:23
5dw	0	47	Jun	11	23:04:31	Jun	11	23:05:18
3dw	1.72945e-13	74	Jun	11	23:07:42	Jun	11	23:08:56
4dw	8.06874e-103	46	Jun	11	23:09:50	Jun	11	23:10:36
5dw	3.06125e-129	99	Jun	11	23:10:36	Jun	11	23:12:15
4dw	2.92835e-20	13	Jun	11	23:12:15	Jun	11	23:12:28
5dw	2.29797e-106	84	Jun	11	23:12:28	Jun	11	23:13:52
5dw	2.55915e-112	96	Jun	11	23:13:52	Jun	11	23:15:28
5dw	5.56892e-92	86	Jun	11	23:15:36	Jun	11	23:17:02

4dw	2.78679e-134	59	Jun	11	23:37:48	Jun	11	23:38:47
5dw	2.37265e-111	9	Jun	11	23:39:33	Jun	11	23:39:42
5dw	0	52	Jun	11	23:39:42	Jun	11	23:40:34
5dw	0	51	Jun	11	23:40:34	Jun	11	23:41:25
4up	4.49524e-28	49	Jun	11	23:41:25	Jun	11	23:42:14
4up	7.03397e-55	50	Jun	11	23:42:14	Jun	11	23:43:04
4up	5.64419e-39	51	Jun	11	23:43:04	Jun	11	23:43:55
4up	5.36904e-55	52	Jun	11	23:43:55	Jun	11	23:44:47
4up	0	57	Jun	11	23:44:49	Jun	11	23:45:46
3up	0	59	Jun	11	23:48:14	Jun	11	23:49:13
4dw	2.57194e-33	78	Jun	12	00:21:41	Jun	12	00:22:59
4dw	8.03715e-203	78	Jun	12	00:23:11	Jun	12	00:24:29
5up	8.00514e-68	60	Jun	12	00:24:29	Jun	12	00:25:29
5up	2.08927e-111	40	Jun	12	00:25:35	Jun	12	00:26:35
4up	3.4164e-38	44	Jun	12	00:29:04	Jun	12	00:29:48
5up	8.46588e-34	45	Jun	12	00:29:48	Jun	12	00:30:33
3up	1.14087e-22	22	Jun	12	00:30:33	Jun	12	00:30:55
3dw	5.37834e-173	44	Jun	12	01:09:09	Jun	12	01:09:53
4up	1.63879e-44	51	Jun	12	01:14:26	Jun	12	01:15:17
5up	1.27605e-73	51	Jun	12	01:15:17	Jun	12	01:16:08
3up	1.52894e-163	33	Jun	12	01:22:06	Jun	12	01:22:39
4up	0	74	Jun	12	01:23:02	Jun	12	01:24:16
4up	5.18779e-246	56	Jun	12	01:25:15	Jun	12	01:26:11
5dw	1.56158e-68	39	Jun	12	02:00:35	Jun	12	02:01:14
5dw	8.41247e-288	50	Jun	12	02:03:48	Jun	12	02:04:38
5dw	1.50078e-316	13	Jun	12	02:04:38	Jun	12	02:05:12

A.3 He nuclei flux fluctuation occurrences

nbins	Likelihood	Dtime (s)		date_enter		date_exit
5dw	4.5442e-47	39	Jun	8 22:52:04	Jun	8 22:52:42
4dw	8.4989e-41	31	Jun	8 23:43:53	Jun	8 23:44:24
3dw	2.07831e-23	82	Jun	8 23:48:03	Jun	8 23:49:25
3dw	5.93112e-100	58	Jun	8 23:49:25	Jun	8 23:50:23
4dw	1.76085e-53	51	Jun	9 02:06:11	Jun	9 02:07:02
5dw	5.27757e-52	44	Jun	9 02:07:02	Jun	9 02:07:46
4dw	3.09066e-33	37	Jun	9 03:36:41	Jun	9 03:37:18
3dw	2.92721e-39	58	Jun	9 17:12:04	Jun	9 17:13:02
4dw	1.20436e-43	42	Jun	9 17:14:53	Jun	9 17:15:35
3dw	4.22658e-15	41	Jun	9 17:18:51	Jun	9 17:19:32
3dw	1.82075e-25	4	Jun	9 20:23:53	Jun	9 20:23:57
3dw	6.81893e-24	43	Jun	9 21:46:38	Jun	9 21:47:21
3dw	5.86626e-24	38	Jun	9 21:54:18	Jun	9 21:54:56

3dw	7.37611e-90	82	Jun	9	22:47:33	Jun	9	22:48:55
4dw	6.02591e-75	52	Jun	9	23:22:50	Jun	9	23:23:42
5dw	1.80881e-73	46	Jun	9	23:25:24	Jun	9	23:26:09
4dw	6.97296e-46	40	Jun	9	23:26:09	Jun	9	23:26:49
4dw	4.40092e-73	41	Jun	9	23:26:49	Jun	9	23:27:30
4dw	3.14728e-55	39	Jun	9	23:27:30	Jun	9	23:28:09
4dw	5.29016e-59	39	Jun	9	23:28:09	Jun	9	23:28:48
4dw	1.65337e-46	41	Jun	9	23:28:48	Jun	9	23:29:29
3dw	2.34867e-18	62	Jun	10	00:08:18	Jun	10	00:09:20
3dw	1.39577e-22	21	Jun	10	00:13:23	Jun	10	00:13:44
4dw	7.15663e-35	50	Jun	10	00:13:44	Jun	10	00:14:34
3up	6.55525e-14	52	Jun	10	00:14:34	Jun	10	00:15:26
3dw	1.06587e-29	48	Jun	10	00:56:25	Jun	10	00:57:12
3dw	2.31905e-18	56	Jun	10	01:42:41	Jun	10	01:43:37
4dw	1.18344e-46	49	Jun	10	02:34:43	Jun	10	02:35:32
4dw	9.14379e-33	20	Jun	10	20:49:22	Jun	10	20:50:10
5dw	3.21529e-58	46	Jun	10	20:55:39	Jun	10	20:56:25
4dw	5.99193e-107	50	Jun	10	20:56:25	Jun	10	20:57:15
5dw	7.79003e-64	54	Jun	10	21:37:47	Jun	10	21:38:41
4dw	1.66225e-76	31	Jun	10	22:23:37	Jun	10	22:24:08
3dw	4.76869e-15	18	Jun	10	23:17:20	Jun	10	23:17:38
4dw	7.37903e-106	32	Jun	11	01:36:22	Jun	11	01:36:54
4dw	1.3406e-30	35	Jun	11	01:36:54	Jun	11	01:37:29
4dw	3.19317e-98	41	Jun	11	03:08:52	Jun	11	03:09:33
4dw	1.31837e-49	32	Jun	11	18:10:58	Jun	11	18:11:30
3dw	1.55323e-30	17	Jun	11	19:43:05	Jun	11	19:43:22
4dw	1.46398e-43	17	Jun	11	19:47:15	Jun	11	19:47:32
4dw	3.32893e-92	39	Jun	11	19:58:00	Jun	11	19:58:39
3up	3.28171e-17	54	Jun	11	20:36:12	Jun	11	20:37:06
4dw	8.86256e-26	82	Jun	11	21:16:13	Jun	11	21:17:35
5dw	2.77342e-97	31	Jun	11	21:22:16	Jun	11	21:22:47
4dw	8.86147e-55	36	Jun	11	22:06:35	Jun	11	22:07:11
4dw	5.38744e-30	17	Jun	11	22:07:11	Jun	11	22:07:28
4dw	4.7196e-51	53	Jun	11	22:07:28	Jun	11	22:08:21
3dw	6.25339e-28	44	Jun	11	22:14:04	Jun	11	22:14:48
4dw	1.42345e-46	41	Jun	11	22:49:19	Jun	11	22:50:00
4dw	1.30361e-35	39	Jun	11	22:57:05	Jun	11	22:57:44
3dw	1.95534e-17	9	Jun	11	23:39:33	Jun	11	23:39:42
4dw	6.25017e-81	52	Jun	11	23:39:42	Jun	11	23:40:34
4dw	8.10264e-61	51	Jun	11	23:40:34	Jun	11	23:41:25
4up	5.69587e-17	50	Jun	11	23:42:14	Jun	11	23:43:04
3up	1.81458e-22	57	Jun	11	23:44:49	Jun	11	23:45:46
4dw	6.16139e-43	50	Jun	12	02:03:48	Jun	12	02:04:38
5dw	1.62435e-38	13	Jun	12	02:04:38	Jun	12	02:05:12

Appendix B

AMS Flight Chronology

The tables below, retrieved from the AMS-01 Experiment Online Monitoring web page [97], give a summary of the main events concerning AMS during the flight STS-91 from June 2 to June 12, 1998. The events concerning the Shuttle are in **red**. The Orbital maneuverings correspond to changes to the orbit parameters. The modifications of the Shuttle attitude are in **blue**. The angle of the AMS +Z-axis is given relative to the Zenith (or to the Nadir). The corresponding time is taken from the CAS (Customer Ancillary Service or Calibrated Ancillary System) data, more precise than AMS log book [99]. The AMS events are shown in **green**. The Power steps are taken from the AMS log book, the Slow Rate Data Link (SRDL) availability from the SRDL files.

UT day	UT	Mission Elapsed Time		Event
	ddd:hh:mm:ss	dd:hh:mm:ss	dec. hours	STS attitude AMS
June 2	153:22:06:24	00:00:00	0.0	Liftoff
June 2	153:22:50:34	00:00:44:10	0.733	Insertion in orbit
June 2	153:23:50:02	00:01:43:38	1.727	Payload bay opening
June 3	154:00: 22	00:02:16	2.27	AMS pointing to Nadir
June 3	154:01:09	00:03:03	3.05	Power Step 1 (start monitoring)
June 3	154:01:37	00:03:31	3.52	End of AMS pointing to Nadir
June 3	154:01:47:41	00:03:41:18	3.69	Orbital maneuvering
June 3	154:02:16	00:04:10	4.17	AMS pointing 45° to Zenith
June 3	154:05:11	00:07:05	7.08	Power Step 2
June 3	154:05:19	00:07:13	7.21	Power Step 3
June 3	154:05:32	00:07:26	7.43	Data acquisition started
June 3	154:14:11	00:16:05	16.08	End of AMS pointing 45° to Zenith
June 3	154:14:34:14	00:16:27:50	16.464	Orbital maneuvering

UT day	UT	Mission Elapsed Time		Event
	ddd:hh:mm:ss	dd:hh:mm:ss	dec. hours	STS attitude AMS
June 3	154:17:08	00:19:02	19.03	AMS pointing 45° to Zenith
June 3	154:21:07	00:23:01	23.02	End of AMS pointing 45° to Zenith
June 3	154:21:23:31	00:23:17:08	23.285	Orbital maneuvering
June 3	154:21:39	00:23:33	23.55	AMS pointing 45° to Zenith
June 3	154:23:04	01:00:58	24.96	SRDL down
June 3	154:23:29	01:01:23	25.38	SRDL up
June 4	155:11:42	01:13:36	37.60	End of AMS pointing 45° to Zenith
June 4	155:15:06	01:17:00	41.00	AMS pointing to Zenith
June 4	155:15:26	01:17:20	41.326	MIR Rendezvous
June 4	155:16:58	01:18:52	42.866	End of AMS pointing to Zenith
June 4	155:16:58	01:18:52	42.866	MIR Docking
June 8	159:15:57	05:17:51	137.91	MIR Undocking
June 8	159:17:53	05:19:47	139.78	AMS pointing to Zenith
June 9	160:07:03	06:08:57	152.95	SRDL down
June 9	160:07:43	06:09:37	153.62	SRDL up
June 9	160:12:52	06:14:46	158.77	End of AMS pointing to Zenith
June 9	160:13:03	06:14:57	158.95	AMS pointing to Zenith
June 9	160:17:31	06:19:25	163.42	Power Step 1
June 9	160:17:42	06:19:36	163.60	End of AMS pointing to Zenith
June 9	160:17:46	06:19:40	163.67	AMS pointing 45° to Zenith
June 9	160:20:10	06:22:04	166.07	Power Step 3
June 9	160:21:03	06:22:57	166.95	End of AMS pointing 45° to Zenith
June 9	160:21:06	06:23:00	167.00	AMS pointing 20° to Zenith
June 10	161:11:14	07:13:08	181.13	Power Step 1
June 10	161:12:14	07:14:08	182.13	Power Step 3
June 10	161:12:21	07:14:15	182.25	End of AMS pointing 20° to Zenith
June 10	161:12:31	07:14:25	182.42	AMS pointing 20° to Zenith
June 10	161:18:37	07:20:31	188.52	Power Step 1
June 10	161:18:39	07:20:33	188.55	End of AMS pointing 20° to Zenith
June 10	161:19:22	07:21:16	189.27	Power Step 3
June 10	161:19:49	07:21:43	189.72	AMS pointing 30° to Zenith
June 11	162:01:27	08:03:21	195.35	End of AMS pointing 30° to Zenith
June 11	162:01:29	08:03:23	195.38	AMS pointing 45° to Zenith
June 11	162:12:06	08:14:00	206.00	SRDL down (scheduled)
June 11	162:13:04	08:14:58	206.97	SRDL up
June 11	162:13:21	08:15:15	207.25	End of AMS pointing 45° to Zenith
June 11	162:13:39	08:15:33	207.55	AMS pointing 45° to Zenith
June 11	162:16:06	08:18:00	210.00	End of AMS pointing 45° to Zenith
June 11	162:16:30:00	08:18:23:36	210.393	Orbital maneuvering

UT day	UT	Mission Elapsed Time		Event
	ddd:hh:mm:ss	dd:hh:mm:ss	dec. hours	STS attitude AMS
June 11	162:16:49	08:18:43	210.72	AMS pointing 45° to Zenith
June 11	162:18:40	08:20:34	212.55	SRDL down (scheduled)
June 11	162:18:45	08:20:39	212.65	End of AMS pointing 45° to Zenith
June 11	162:19:18	08:21:12	213.20	SRDL up
June 11	162:19:42	08:21:36	213.60	AMS pointing 45° to Zenith
June 11	162:22:09	09:00:03	216.04	SRDL down
June 11	162:22:33	09:00:27	216.44	SRDL up
June 12	163:02:36	09:04:30	220.50	End of AMS pointing 45° to Zenith
June 12	163:02:49	09:04:43	220.72	AMS pointing to Nadir
June 12	163:12:46	09:14:40	230.666	Power Step 1
June 12	163:12:55	09:14:49	230.82	End of AMS pointing to Nadir
June 12	163:14:00	09:15:54	231.9	AMS deactivation (end monitoring)
June 12	163:14:15:36	09:16:09:12	232.153	Payload bay closed
June 12	163:16:52:25	09:18:46	234.766	Deorbiting maneuvering
June 12	163:18:00:18	09:19:53:54	235.898	Touch down

B.0.1 Attitude parameters from June 8 to June 12

The pictures below, retrieved from the AMS-01 Experiment Online Monitoring web page [98], report the Shuttle attitude parameters for the period from June 8 to June 12. Each figure contains the following graphs:

- Angle between the Shuttle Z-axis and the direction of the Vernal point [deg] vs. MET. This angle should be constant if the Shuttle attitude is fixed like during the docking with Mir. It varies periodically if the Shuttle attitude is fixed relative to LVLH¹, like during the AMS data taking.
- Angle between the Shuttle Z-axis and the Nadir direction [deg] vs. MET. This is equivalent to the angle between AMS Z-axis and the Zenith direction. This angle is constant when the Shuttle attitude is fixed relative to LVLH. It varies periodically when the Shuttle attitude is fixed relative to the stars, like during docking.
- Angle between the North and the projection of AMS Z-axis on an horizontal plane [deg] vs. MET. This angle is poorly determined when the Z-axis direction is vertical.
- Angle between AMS Z-axis and the Earth brim [deg] vs. MET. The blue line corresponds to 50 deg. When the angle is greater than 50 deg. the Earth

¹The definition of the various reference frames used can be found in Ref. [99].

is not in AMS field of view.

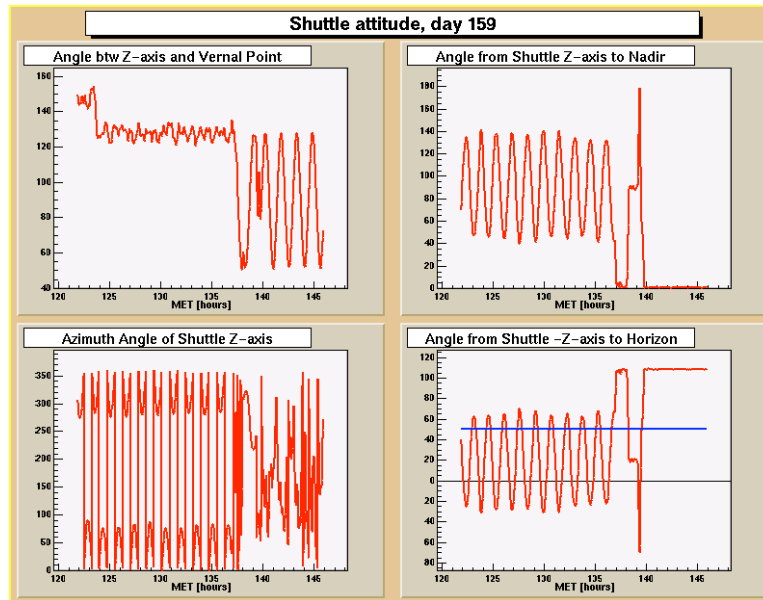


Figure B.1: Shuttle attitude parameters: June 8.

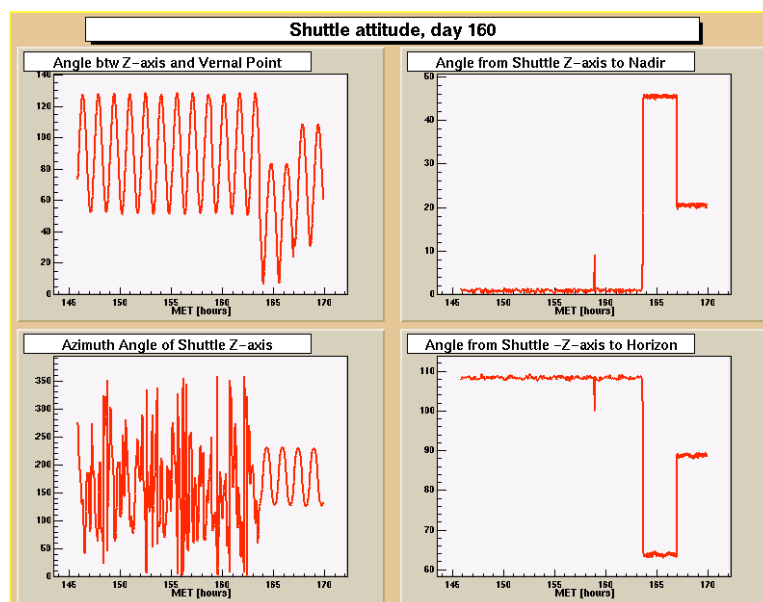


Figure B.2: Shuttle attitude parameters: June 9.

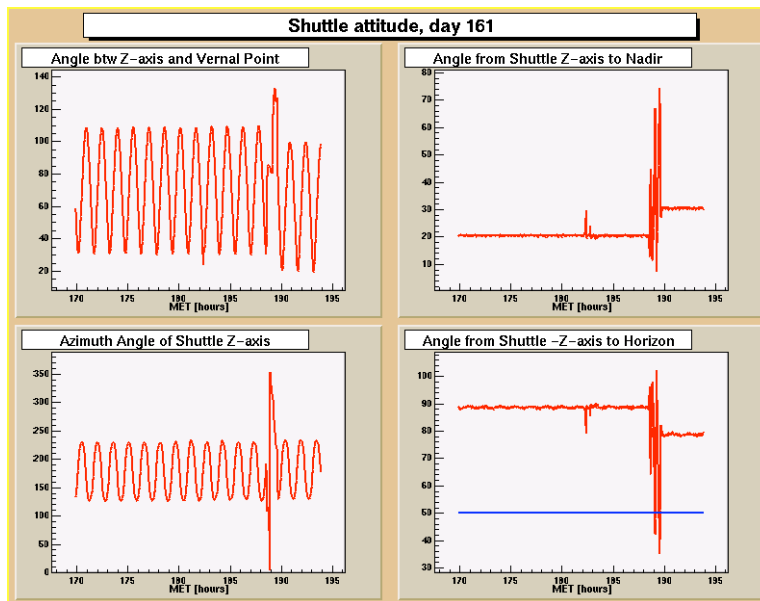


Figure B.3: Shuttle attitude parameters: June 10.

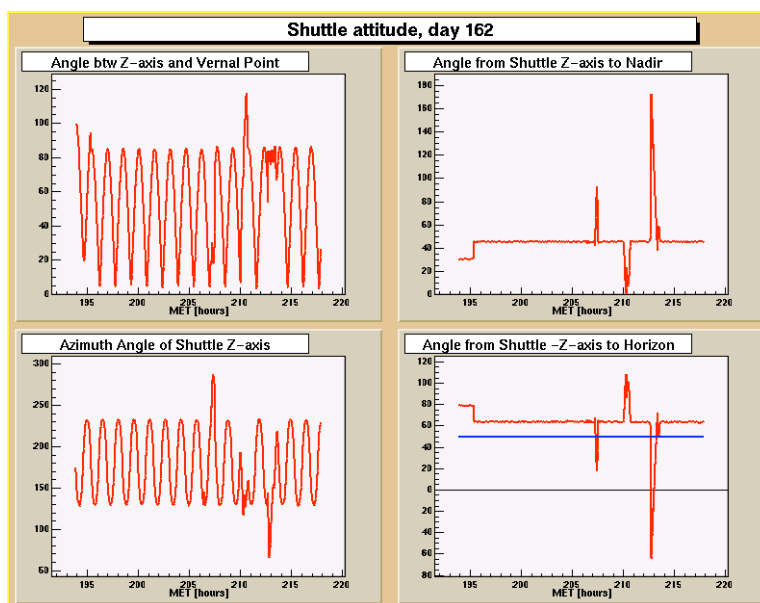


Figure B.4: Shuttle attitude parameters: June 11.

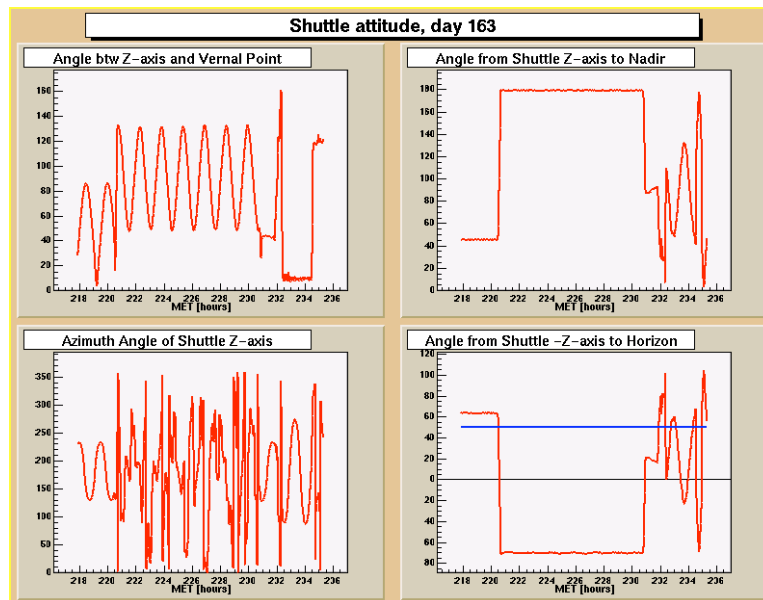


Figure B.5: Shuttle attitude parameters: June 12.

Appendix C

Solar activity in June 1998

In 1998 the Sun was at the rising phase of its cycle, the solar minimum being occurred in 1996. Thus the AMS-01 flight has taken place during a period of low solar activity level. In this chapter are reported the observations of the solar activity for the period of interest (1st to 15th June 1998) performed by dedicated experiment.

GOES observations from 1st to 15th June 1998.

Figure C.1 reports (from top to bottom) the measurements performed by the X-ray Sensor (XRS), Energetic Particle Sensor (EPS) and Magnetometer on board the Geostationary Operational Environmental Satellites (GOES) [11], and the McMurdo neutron monitor [74]. The XRS provides whole-sun X-ray (XL: 1 – 8 Å, XS: 0.5 – 3 Å) fluxes, on the left vertical scale is indicated the solar flare classification. The ESP are solid-state discrimination detectors sensitive to > 2 MeV electrons (E1), > 100 MeV protons (I1-I6) and 150 – 500 MeV He nuclei (A5, A6). The Magnetometer measures the Interplanetary Magnetic Field (IMF) vector: the plot shows the component HP perpendicular to the satellite's orbital plane.

The GOES X-ray solar flare catalog, retrieved from the European Grid of Solar Observations (EGSO) [118], is reported in Tables C.3, C.4 and C.5. X-ray flares are classified according to the order of magnitude of the peak burst intensity, I , measured at the Earth by satellites in the 1 – 8 Å band as specified in Table C.1. The number following the X-ray class code (B, C, M, X) represents the peak burst

Table C.1: X-ray flare classification.

Class	W/m^2
B	$I < 10^{-6}$
C	$10^{-6} \leq I < 10^{-5}$
M	$10^{-5} \leq I < 10^{-4}$
X	$I \geq 10^{-4}$

intensity I . For events correlated to an optical flare the heliographic latitude and longitude, the active region identification number, the Carrington longitude and the class of the correlated optical event are given. Optical flares are classified according to their brightness (f=faint, n=normal, b=bright) and importance, which is related to the flare area (s, 1, 2 or 3).

LASCO coronal mass ejection catalog.

Tables C.6, C.7, C.8 and C.9 report the coronal mass ejections (CMEs) manually identified from the Large Angle and Spectrometric Coronagraph (LASCO) [119] on board the Solar and Heliospheric Observatory (SOHO) [120] mission from 1st to 15th June 1998.

Since CMEs take from less of one day up to five days to reach the Earth, the period of interest for the work presented in this document reduces to 3th-11th June 1998.

Only data gaps of three hours duration or more are reported. For the period of interest the LASCO C2 downtime was:

1998/06/10 18:06 - 1998/06/10 21:10

LASCO has three telescopes C1, C2 and C3, however only C2 and C3 data are used for uniformity because C1 was disabled in June 1998. For each CME the catalog reports the date and time of first appearance in the C2 field of view, the central position angle (CPA) and the angular width. Since more than 10 CMEs can occur on a single day, the CPA allow to distinguish CMEs appearing simultaneously in the C2 field of view. CMEs having an apparent width of 360 deg are marked as Halo in the CPA column. Halo CMEs can be symmetric (S) or asymmetric (brightness asymmetry (BA) or outline asymmetry (OA)) with respect to the occulting disk. The halo CMEs are accordingly labeled as Halo (S), Halo (BA), and Halo (OA).

The next two columns report the CME linear speed, obtained by fitting a straight line, and acceleration. For some CMEs, which show significant acceleration, the linear fit is not suitable. However, the linear speed serves as an average speed within the LASCO field of view.

The acceleration of a CME can be positive, negative or close to zero meaning CMEs speed up, move with constant speed or slow down within the LASCO field of view. A minimum of three height-time measurements are needed for an estimate of the acceleration, but the accuracy increases when there are more measurements. Accelerations with just three measurements are not reliable and are marked with a superscript, *1.

Each CME is also characterized by a mass and a kinetic energy. There are generally large uncertainties in these numbers. Estimation of CME mass involves a number of assumptions, so the values given should be taken as representative. For example, most CMEs show an increase in mass when they traverse the first several solar radii, and then the mass reaches a quasi-constant value. This constant value is

taken as the representative mass. Some CMEs fade within the first few solar radii. In these cases the mass corresponds to the time of last measurement. The mass estimates of halo CMEs are also very uncertain. The kinetic energy is obtained from the linear speed and the representative mass. Mass and kinetic energy values subject to such uncertainties are superscripted with *2.

The next column gives the position angle at which the height-time measurements are made (MPA for measurement position angle). Ideally, the MPA and CPA must be the same. However, some CMEs move nonradially so the two do not coincide. Even though there is no CPA for a halo CME, there is an MPA, corresponding to the PA of the fastest moving segment of the CME leading edge.

The last column of the list contains some remarks regarding the number of data points and other limitations.

The list has been retrieved from the SOHO LASCO CME CATALOG:
http://cdaw.gsfc.nasa.gov/CME_list/UNIVERSAL/1998_06/univ1998_06.html

Solar related events observed at Earth from 1st to 15th June 1998.

Solar Energetic Particles

No Solar Energetic Particle events have been observed during the period of interest.

Ground Level Enhancements

No cosmic ray Ground Level Enhancements have been observed during the period of interest.

Magnetic storms

The only magnetic storm reported between June 1 and June 15 1998 has occurred on June 14 , when AMS-01 had been already shut down. The British Antarctic Survey (BAS) [121] magnetic storm catalog is reported in Table C.2. In the table are listed the magnetic storm start time, peak time, end time, and duration in hours (hduration), and the Disturbance Storm Time (DST).

Table C.2: British Antarctic Survey magnetic storm catalog:

time start	time peak	time end	DST	hduration
1998-06-14 06:00	1998-06-14 10:00	1998-06-14 18:00	-55	12

The list has been retrieved from the European Grid of Solar Observations (EGSO).

Figure C.1: GOES observations from 1st to 15th June 1998

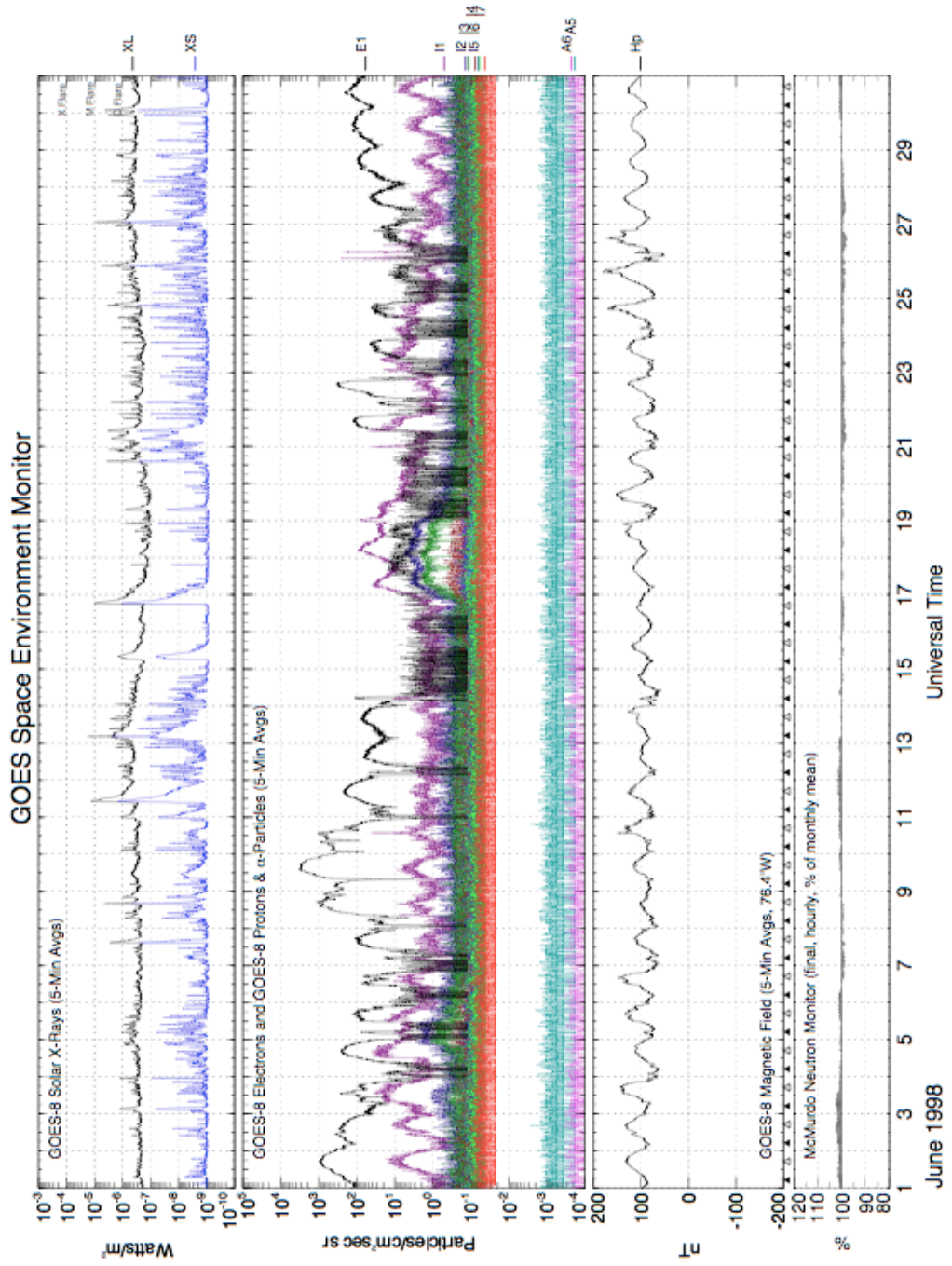


Table C.3: GOES Solar flare catalog 1.3

time	time	time	active region	heliographic	heliographic	Carrington	xray	optical
start	peak	end	number	latitude	longitude	longitude	class	class
1998-06-02 14:18	1998-06-02 14:23	1998-06-02 14:28					B7.7	
1998-06-03 02:34	1998-06-03 03:03	1998-06-03 03:57					C1.4	
1998-06-03 13:07	1998-06-03 13:10	1998-06-03 13:14	8233	27	-65	-7.2	B5.3	sf
1998-06-03 14:24	1998-06-03 14:28	1998-06-03 14:32	8233				B4.7	
1998-06-03 16:17	1998-06-03 16:21	1998-06-03 16:25	8233				B4.0	
1998-06-03 23:01	1998-06-03 23:08	1998-06-03 23:13					C1.6	
1998-06-04 11:20	1998-06-04 11:24	1998-06-04 11:27	8232	-23	-49	-3.45	B7.0	sf
1998-06-04 20:34	1998-06-04 20:39	1998-06-04 20:46	8232	-27	-51	-10.54	C1.0	sf
1998-06-04 21:28	1998-06-04 21:43	1998-06-04 21:49	8232	-25	-49	-9.04	C1.0	sf
1998-06-05 03:02	1998-06-05 03:08	1998-06-05 03:13					B6.7	
1998-06-05 04:39	1998-06-05 04:45	1998-06-05 04:51	8232	-26	-43	-7	C1.4	sf
1998-06-05 06:43	1998-06-05 06:48	1998-06-05 06:54	8232	-25	-45	-10.14	B9.0	sf
1998-06-05 09:47	1998-06-05 09:53	1998-06-05 09:57	8232	-23	-43	-9.83	C1.2	sf
1998-06-05 14:15	1998-06-05 14:20	1998-06-05 14:23	8232	-24	-41	-10.29	C1.1	sf
1998-06-05 15:03	1998-06-05 15:08	1998-06-05 15:14					B6.8	
1998-06-07 11:07	1998-06-07 11:12	1998-06-07 11:17	8236	21	16	21.97	B5.2	sf
1998-06-07 14:43	1998-06-07 14:54	1998-06-07 15:16	8232	-23	-12	-8.02	C3.2	1f
1998-06-08 03:35	1998-06-08 03:40	1998-06-08 03:49					B4.1	
1998-06-08 06:39	1998-06-08 06:51	1998-06-08 08:06					B9.1	
1998-06-08 09:45	1998-06-08 09:57	1998-06-08 10:31					B9.0	

Table C.4: GOES Solar flare catalog 2.3

time	time	time	active region	heliographic	heliographic	Carrington	xray	optical
start	peak	end	number	latitude	longitude	longitude	class	class
1998-06-08 13:49	1998-06-08 13:53	1998-06-08 13:58					B4.3	
1998-06-08 15:56	1998-06-08 16:07	1998-06-08 16:14	8232	-18	3	353.08	C5.2	2n
1998-06-08 19:45	1998-06-08 20:09	1998-06-08 20:56		-30	8	355.97	C1.0	sf
1998-06-09 04:25	1998-06-09 04:32	1998-06-09 04:41					B6.1	
1998-06-09 08:35	1998-06-09 08:39	1998-06-09 08:46					B4.0	
1998-06-09 16:10	1998-06-09 16:13	1998-06-09 16:15					B4.3	
1998-06-10 02:24	1998-06-10 02:32	1998-06-10 02:44					C1.3	
1998-06-10 04:02	1998-06-10 04:08	1998-06-10 04:13					C1.2	
1998-06-10 07:00	1998-06-10 07:07	1998-06-10 07:17					B7.2	
1998-06-10 23:11	1998-06-11 00:14	1998-06-11 01:20					C1.1	
1998-06-11 09:57	1998-06-11 10:27	1998-06-11 11:18					M1.4	
1998-06-12 00:23	1998-06-12 00:27	1998-06-12 00:31					B6.7	
1998-06-12 00:32	1998-06-12 02:02	1998-06-12 02:48					C1.1	
1998-06-12 02:49	1998-06-12 02:52	1998-06-12 02:54	8240	-19	70	14.37	C1.2	sf
1998-06-12 04:52	1998-06-12 04:56	1998-06-12 04:59	8238	18	-11	292.24	B9.3	sf
1998-06-12 05:37	1998-06-12 05:40	1998-06-12 05:42	8240	-22	74	16.82	C1.4	sf
1998-06-12 06:13	1998-06-12 06:17	1998-06-12 06:21					C1.0	
1998-06-12 08:20	1998-06-12 08:27	1998-06-12 08:31					C1.1	
1998-06-12 09:14	1998-06-12 09:19	1998-06-12 09:21	8240	-22	77	17.83	C3.1	1f
1998-06-12 21:06	1998-06-12 21:13	1998-06-12 21:29	8242	-25	-54	240.28	C2.1	sf
1998-06-12 22:47	1998-06-12 22:50	1998-06-12 22:53					B9.0	

Table C.5: GOES Solar flare catalog 3.3

time start	time peak	time end	active region number	heliographic latitude	heliographic longitude	Carrington longitude	xray class	optical class
1998-06-12 23:11	1998-06-12 23:18	1998-06-12 23:27	8242	-24	-53	240.13	C1.8	
1998-06-13 01:49	1998-06-13 01:55	1998-06-13 02:00					C1.4	
1998-06-13 02:15	1998-06-13 03:57	1998-06-13 06:21					C2.6	
1998-06-13 04:15	1998-06-13 04:20	1998-06-13 04:28	8242	-27	-54	236.34	M1.9	1n
1998-06-13 09:09	1998-06-13 09:17	1998-06-13 09:32					C3.4	
1998-06-13 12:03	1998-06-13 12:10	1998-06-13 12:15					C1.3	
1998-06-13 14:58	1998-06-13 15:32	1998-06-13 15:54	8237				C2.9	
1998-06-13 17:19	1998-06-13 17:28	1998-06-13 17:32	8242	-23	-43	240.13	C2.4	sf
1998-06-13 17:55	1998-06-13 17:59	1998-06-13 18:02	8242	-20	-45	237.8	C1.3	sf
1998-06-13 23:49	1998-06-14 00:03	1998-06-14 00:20					B9.4	
1998-06-14 01:03	1998-06-14 01:09	1998-06-14 01:13					C3.0	
1998-06-14 04:32	1998-06-14 04:36	1998-06-14 04:42	8245	-31	-12	264.95	B6.5	sf
1998-06-14 05:17	1998-06-14 05:21	1998-06-14 05:24	8242	-22	-35	241.53	B8.1	sf
1998-06-14 08:36	1998-06-14 08:39	1998-06-14 08:42	8243	15	-62	212.7	B6.6	sf
1998-06-14 15:25	1998-06-14 15:29	1998-06-14 15:36	8243	14	-59	211.94	B6.5	sf
1998-06-15 06:00	1998-06-15 07:50	1998-06-15 09:37	8232				C1.4	

Table C.6: LASCO coronal mass ejection catalog 1.4:

First C2 Date Time (UT)	Central PA (deg)	Angular Width (deg)	Linear Speed (km/s)	Accel (m/s ²)	Mass (gram)	Kinetic Energy (erg)	MPA (deg)	Remarks
1998/06/01 11:27:05	263	38	467	60.5*1	—	—	269	Poor Event; Only 3 points; Only C2
1998/06/01 15:00:26	92	11	435	-8.1*1	1.2e+14	1.1e+29	88	Poor Event
1998/06/01 17:27:07	255	8	238	125.6*1	—	—	262	Poor Event; Only 3 points; Only C2
1998/06/02 02:04:10	254	51	210	12.4*1	1.2e+14	2.6e+28	246	Poor Event; Only C2
1998/06/02 02:59:51	118	95	291	2.0	2.4e+15	1.0e+30	117	
1998/06/02 08:08:36	245	59	751	45.2	9.6e+15	2.7e+31	239	
1998/06/02 21:06:24	50	61	782	18.3	2.1e+15	6.5e+30	64	
1998/06/03 09:58:55	68	25	252	31.1*1	—	—	66	
1998/06/03 12:02:22	90	147	818	-6.7	5.5e+15*2	1.8e+31*2	85	Partial Halo
1998/06/03 13:55:05	253	21	370	6.2	—	—	251	
1998/06/03 18:27:05	251	10	362	21.6	—	—	251	
1998/06/03 22:02:09	245	7	232	5.5	—	—	249	
1998/06/03 23:28:13	244	8	318	8.7*1	—	—	250	
1998/06/03 23:28:13	267	11	409	-10.7	—	—	267	
1998/06/03 23:28:13	265	16	586	13.2	—	—	268	
1998/06/04 02:04:45	Halo (OA)	360	1802	-6.5*1	—	—	314	Only 3 points
1998/06/04 06:31:11	45	34	805	13.7	1.4e+15	4.5e+30	55	
1998/06/04 09:36:49	70	42	355	-1.4	5.8e+14	3.7e+29	61	
1998/06/04 21:00:57	262	57	404	1.9	1.2e+15	9.6e+29	256	
1998/06/04 21:27:05	98	115	643	-7.2	3.8e+15	7.8e+30	95	
1998/06/04 22:28:15	67	41	384	-0.5	—	—	62	

Table C.7: LASCO coronal mass ejection catalog 2.4:

First C2 Date Time (UT)	Central PA (deg)	Angular Width (deg)	Linear Speed (km/s)	Accel (m/s ²)	Mass (gram)	Kinetic Energy (erg)	MPA (deg)	Remarks
1998/06/05 01:30:29	217	57	478	1.1	—	—	212	
1998/06/05 07:02:43	205	132	1017	28.3	—	—	221	Partial Halo
1998/06/05 10:28:42	269	74	342	-0.7* ¹	—	—	270	
1998/06/05 12:01:53	Halo (OA)	360	320	3.5	—	—	222	
1998/06/05 13:31:08	99	41	117	1.4* ¹	—	—	97	
1998/06/06 08:27:14	273	34	479	-13.8	2.8e+14	3.3e+29	269	
1998/06/06 12:27:05	58	77	248	-16.3* ¹	3.9e+14* ²	1.2e+29* ²	50	Poor Event; Only C2
1998/06/06 14:00:59	118	47	288	5.3* ¹	3.7e+14	1.5e+29	108	Poor Event
1998/06/06 16:27:05	56	75	92	1.9* ¹	—	—	67	Not LE
1998/06/07 01:30:36	226	7	315	44.0* ¹	—	—	229	Poor Event; Only 3 points; Only C2
1998/06/07 09:32:08	Halo (BA)	360	749	-19.6* ¹	—	—	113	
1998/06/07 19:27:05	301	47	337	-7.4* ¹	5.9e+14	3.4e+29	294	
1998/06/07 23:56:59	250	20	412	1.2* ¹	1.3e+14	1.1e+29	262	
1998/06/08 08:01:01	114	53	126	10.5* ¹	1.2e+14	9.3e+27	120	Poor Event; Only C2
1998/06/08 10:27:05	110	63	275	3.7* ¹	7.6e+14	2.9e+29	118	
1998/06/08 14:55:20	59	30	463	8.6	—	—	68	
1998/06/08 16:27:05	177	240	433	-9.5	—	—	154	Partial Halo; Associated with C-flare
1998/06/09 05:55:35	253	118	265	1.2	7.8e+15	2.8e+30	240	
1998/06/09 08:27:05	87	87	189	-0.8* ¹	2.3e+14	4.2e+28	90	Poor Event
1998/06/09 09:27:05	201	130	124	2.7* ¹	1.7e+15* ²	1.3e+29* ²	219	Poor Event; Partial Halo
1998/06/09 12:27:05	98	19	209	-37.2* ¹	6.3e+12	1.4e+27	104	Poor Event; Only C2

Table C.8: LASCO coronal mass ejection catalog 3.4:

First C2 Date Time (UT)	Appearance PA (deg)	Central Angular Width (deg)	Linear Speed (km/s)	Accel (m/s ²)	Mass (gram)	Kinetic Energy (erg)	MPA (deg)	Remarks
1998/06/09 15:06:06	277	84	252	7.6	4.8e+15	1.5e+30	291	
1998/06/09 16:06:06	107	18	596	-53.5*1	1.2e+14*2	2.2e+29*2	103	Very Poor Event; Only C2
1998/06/09 20:06:05	229	67	77	2.8*1	—	—	222	Partial Halo
1998/06/10 03:55:22	109	144	562	-2.5	5.2e+14*2	8.2e+29*2	98	Poor Event; Only 2 points
1998/06/10 04:26:05	233	4	438	—	—	—	236	Only C2
1998/06/10 08:27:05	152	21	378	7.1*1	—	—	142	
1998/06/10 11:27:05	241	30	444	9.3	1.4e+14	1.4e+29	243	
1998/06/10 16:06:07	297	60	458	5.2	1.9e+15	2.0e+30	302	
1998/06/10 22:06:05	233	6	493	—	—	—	240	Only 2 points
1998/06/11 00:05:06	79	58	500	2.8	3.6e+15	4.5e+30	76	
1998/06/11 08:27:05	261	15	172	2.2*1	—	—	265	Only C2
1998/06/11 10:28:38	123	177	1223	-35.7	—	—	97	Partial Halo; Associated with M-flare
1998/06/11 20:06:05	229	9	392	13.5*1	—	—	233	Only 3 points
1998/06/12 01:55:23	107	7	823	—	—	—	106	Only 2 points; Only C2
1998/06/12 03:55:22	89	43	419	19.0	1.6e+15	1.4e+30	82	
1998/06/12 05:12:11	231	22	584	6.0*1	1.3e+14	2.2e+29	237	
1998/06/12 11:55:22	294	59	173	2.3*1	7.0e+14	1.1e+29	291	
1998/06/12 20:06:05	313	29	579	14.4	1.3e+15	2.1e+30	305	
1998/06/12 22:06:05	71	99	674	0.9	2.9e+15	6.6e+30	102	
1998/06/13 01:55:19	99	30	648	9.7*1	—	—	98	Poor Event
1998/06/13 02:27:07	270	109	462	12.0	1.2e+16	1.3e+31	256	

Table C.9: LASCO coronal mass ejection catalog 4.4:

First C2 Appearance Date Time (UT)	Central PA (deg)	Angular Width (deg)	Linear Speed (km/s)	Accel (m/s ²)	Mass (gram)	Kinetic Energy (erg)	MPA (deg)	Remarks
1998/06/13 05:26:08	67	100	463	3.7	9.8e+14	1.1e+30	82	Associated with M-flare
1998/06/13 08:55:05	92	34	218	1.2* ¹	---	---	87	
1998/06/13 12:55:19	87	37	372	-79.4* ¹	---	---	87	
1998/06/13 13:27:05	294	23	260	14.1	---	---	297	
1998/06/13 17:06:05	188	63	179	2.6* ¹	---	---	188	Only 3 points
1998/06/13 18:06:05	80	23	358	-0.0	---	---	75	
1998/06/13 20:06:05	230	27	645	-14.5	5.1e+14	1.1e+30	246	
1998/06/14 01:55:21	80	33	261	10.8* ¹	9.8e+13* ²	3.3e+28* ²	83	Only C2
1998/06/14 05:55:36	235	36	94	-3.8* ¹	2.5e+14	1.1e+28	223	Very Poor Event; Only C2
1998/06/14 09:27:05	263	32	85	-3.9* ¹	1.8e+14	6.7e+27	269	Very Poor Event; Only C2
1998/06/14 10:28:39	204	72	130	4.3* ¹	3.8e+14	3.3e+28	209	Very Poor Event; Only C2
1998/06/15 02:27:06	218	53	163	4.1* ¹	8.2e+14	1.1e+29	215	Poor Event
1998/06/15 05:27:09	94	44	420	0.3* ¹	1.4e+15	1.3e+30	93	
1998/06/15 06:55:20	291	93	535	0.6	8.2e+15	1.2e+31	285	
1998/06/15 14:55:19	195	80	285	7.7	2.9e+15	1.2e+30	195	
1998/06/15 17:27:25	106	69	535	11.9	2.6e+15	3.8e+30	113	

Bibliography

- [1] M.S. Longair. *High Energy Astrophysics*, volume I and II. Cambridge University Press, 1992. and references therein.
- [2] Peter K.F. Grieder. *Cosmic Rays at Earth*. Elsevier, Amsterdam, 2001. and references therein.
- [3] T.K. Gaisser. *Cosmic Rays and Particle Physics*. Cambridge University Press, 1990.
- [4] W.-M. Yao *et al.*. Review of Particle Physics. *Journal of Physics G*, 33:1+, 2006.
- [5] M. J. Aschwanden. *Physics of the Solar Corona. An Introduction with Problems and Solutions (2nd edition)*. Praxis Publishing Ltd., Chichester, UK; Springer, New York, Berlin, December 2005.
- [6] R. Schwenn. Space Weather: The Solar Perspective. *Living Reviews in Solar Physics*, 3(2), 2006.
- [7] T. Pulkkinen. Space Weather: Terrestrial Perspective. *Living Reviews in Solar Physics*, 4(1), 2007.
- [8] <http://www-istp.gsfc.nasa.gov/istp/wind/>.
- [9] <http://www.srl.caltech.edu/ACE/>.
- [10] <http://nssdc.gsfc.nasa.gov/space/imp-8.html>.
- [11] <http://goespoes.gsfc.nasa.gov/goes/project/index.html>.
- [12] <http://pwg.gsfc.nasa.gov/polar/>.
- [13] <http://www.stp.isas.ac.jp/geotail/>.
- [14] <http://pluto.space.swri.edu/IMAGE/>.
- [15] <http://swdcwww.kugi.kyoto-u.ac.jp/wdc/obslink.html>.

- [16] J.M. Clem H. Moraal, A. Belov. Design and co-Ordination of Multi-Station International Neutron Monitor Networks. *Space Science Reviews*, 93:285–303, 2000.
- [17] <http://astrophysics.gsfc.nasa.gov/astroparticles/programs/bess/BESS.html>.
- [18] <http://marge.phys.washington.edu/jacee/>.
- [19] E. S. Seo *et al.*. Cosmic-ray energetics and mass (CREAM) balloon project. *Advances in Space Research*, 33:1777–178, 2004.
- [20] D. Muller *et al.*. The TRACER Project : Instrument Concept, Balloon Flights and Analysis Procedures. In *Proceedings of the 30th International Cosmic Ray Conference, Merida, Yucatan, Mexico, July 3 - 11, 2007*.
- [21] M. Aguilar *et al.* [AMS Collaboration]. The Alpha Magnetic Spectrometer (AMS) on the International Space Station: Part I - results from the test flight on the Space Shuttle. *Physics Reports*, 366:331–405, 2002.
- [22] P. Picozza *et al.* [The PAMELA Collaboration]. PAMELA - A payload for antimatter matter exploration and light-nuclei astrophysics. *Astropart. Phys.*, 27:296–315., April 2007.
- [23] J.A. Simpson. Evolution of our knowledge of the heliosphere. *Advances in Space Research*, 9:5–20, 1989.
- [24] J. Clem and P. Evenson. Observations of cosmic ray electrons and positrons during the early stages of the A- magnetic polarity epoch. *J. Geophys. Res.*, 109, 2004.
- [25] J. Alcaraz *et al.* [AMS Collaboration]. Leptons in Near Earth Orbit. *Phys. Lett. B*, 484:10–22, 2000.
- [26] J. Olzem, H. Gast and S. Schael. Cosmic-Ray Positron Identification through Bremsstrahlung Conversion. *Nucl. Phys. B Proc. Suppl.*, 173:51–55, 2007.
- [27] M. Boezio *et al.*. The Cosmic Ray Electron and Positron Spectra Measured at 1 AU during Solar Minimum Activity. *The Astrophysical Journal*, 532(1):653–669, 2000.
- [28] M.A. DuVernois *et al.*. Cosmic Ray Electrons and Positrons from 1 to 100 GeV: Measurements with HEAT and Their Interpretation. *The Astrophysical Journal*, 559(1):296–303, 2001.
- [29] A. S. Beach *et al.*. Measurement of the Cosmic-Ray Antiproton-to-Proton Abundance Ratio between 4 and 50 GeV. *Phys. Rev. Lett.*, 87(27):271101, Dec 2001.

- [30] A. Yamamoto *et al.*. Search for primordial antiparticles with BESS. *Adv. Space Res.*, in press, 2007.
- [31] M. Sasaki *et al.*. Progress in search for antihelium with BESS. *Nuclear Physics B*, 113, 2002.
- [32] H. Fuke *et al.*. Search for Cosmic-Ray Antideuterons. *Phys. Rev. Lett.*, 95, 2005.
- [33] M. Nagano [The AGASA Collaboration]. A new 100-km**2 air shower array at Akeno (AGASA). In *Proceedings of the 10th ICCR International Symposium on the Astrophysical Aspects of the Most Energetic Cosmic Rays, Kofu, Japan, Nov. 26-29, 1990*.
- [34] S. Westerhoff. HiRes: Searching for the origins of ultra high energy cosmic rays. *AIP Conf. Proc.*, 698:370–373, 2004.
- [35] E. Parizot. The Pierre Auger Observatory: status, results and perspective. 2007.
- [36] K. Greisen. End to the Cosmic-Ray Spectrum? . *Phys. Rev. Lett.*, 16(17):748–750, Apr 1966.
- [37] G. T. Zatsepin and V. A. Kuzmin. Upper limit of the spectrum of cosmic rays. *JETP Lett.*, 4:78–80, 1966.
- [38] M. Takeda *et al.* [The AGASA Collaboration]. Energy determination in the Akeno Giant Air Shower Array experiment. *Astroparticle Physics*, 19:447–462., 2003.
- [39] R. Abbasi *et al.* [The HiRes Collaboration]. Observation of the ankle and evidence for a high-energy break in the cosmic ray spectrum. *Physics Letters B*, 619:271–280., 2005.
- [40] R. Abbasi *et al.* [The HiRes Collaboration]. Observation of the GZK cutoff by the HiRes experiment. *astro-ph/0703099*, 2007.
- [41] L. Perrone [The Pierre Auger Collaboration]. Measurement of the UHECR energy spectrum from hybrid data of the Pierre Auger Observatory. In *Proceedings of the 30th International Cosmic Ray Conference, Merida, Yucatan, Mexico, July 3 - 11, 2007*.
- [42] The Pierre Auger Collaboration. Correlation of the highest-energy cosmic rays with the positions of nearby active galactic nuclei. *Astropart. Phys.*, 29:188–204, 2008.
- [43] <http://heasarc.nasa.gov/docs/rosat/rosat.html>.
- [44] <http://heasarc.nasa.gov/docs/rosat/gallery/display/saa.html>.

- [45] S. L. Snowden *et al.*. The Particle Background of the ROSAT PSPC. *The Astrophysical Journal*, 393:819–828, 1992.
- [46] <http://svs.gsfc.nasa.gov/vis/a000000/a003300/a003356/index.html>.
- [47] http://www.nasa.gov/mission_pages/themis/mission/index.html.
- [48] M.A. Shea and D.F. Smart. Fifty years of cosmic radiation data. *Space Science Reviews*, 93:229–262, 2000.
- [49] <http://cosray.unibe.ch/>.
- [50] Y. Shikaze *et al.*. Measurements of 0.2-GeV/n to 20-GeV/n cosmic-ray proton and helium spectra from 1997 through 2002 with the BESS spectrometer. *Astropart. Phys.*, 28:154–167, 2007.
- [51] H. S. Ahluwalia. Eleven year variation of cosmic ray intensity and solar polar field reversals. In *Proceedings of the 16th International Cosmic Ray Conference, Kyoto, Japan, August 6-18, 1979*.
- [52] S. E. Forbush. Worldwide cosmic ray variations, 1937-1952. *J. Geophys. Res.*, 59:525–542, 1954.
- [53] H. S. Ahluwalia. Solar polar field reversals and secular variations of cosmic ray intensity. In M. Dryer and D. Reidel E. Tanderg-Hanssen, editors, *Solar and Interplanetary Dynamics*, pages 79–89, 1980.
- [54] C.T. Russell and R.L. McPherron. Semiannual variation of geomagnetic activity. *J. Geophys. Res.*, 78:92, 1973.
- [55] M. V. Alania *et al.*. 27-Day variations of galactic cosmic rays and changes of solar and geomagnetic activities. *Advances in Space Research*, 27:619–624, 2001.
- [56] S. E. Forbush. Solar influences on cosmic rays. *Proc. Natl. Acad. Sci.*, 43:28–41, 1957.
- [57] S. E. Forbush. Cosmic-ray intensity variations during two solar cycles. *J. Geophys. Res.*, 63:651–669, 1958.
- [58] E. O. Flueckiger *et al.*. The Cosmic Ray Ground Level Enhancement during the Forbush Decrease in January 2005. In *Proceedings of 29th International Cosmic Ray Conference (ICRC 2005), Pune, India, 3-11 Aug 2005*, volume 1, pages 225–+.
- [59] S. N. Karpov, L. I. Miroshnichenko, and E. V. Vashenyuk. In *Proceedings of the 25th International Cosmic Ray Conference, Durban, South Africa, 30 July - 6 Aug. 1997*, volume 1, page 205.

- [60] R. C. Carrington. Description of a singular appearance seen on the Sun on September 1, 1859. *Mon. Not. Roy. Astron. Soc.*, 20, 1860.
- [61] J.T. Gosling. The solar flare myth. *J. Geophys. Res.*, 98:18937–18950, 1993.
- [62] D.V. Reames. Solar Energetic Particles: A paradigm shift. *Rev. Geophys.*, 33, 1995.
- [63] R. Schwenn. Direct correlations between coronal transients and interplanetary disturbances. *Space Sci. Rev.*, 34:85–99, 1983.
- [64] N.R. Sheeley Jr, R.A. Howard, M.J. Koomen, D.J. Michels, R. Schwenn, K.H. Mühlhäuser, and H. Rosenbauer. Associations between coronal mass ejections and interplanetary shocks. In M. Neugebauer, editor, *Solar Wind Five*, volume 2280 of *NASA Conference Publication*, pages 693–702, Washington, U.S.A., 1983. NASA.
- [65] N.R. Sheeley Jr, R.A. Howard, D.J. Michels, M.J. Koomen, R. Schwenn, K.H. Mühlhäuser, and H. Rosenbauer. Coronal mass ejections and interplanetary shocks. *J. Geophys. Res.*, 90:163–175, 1985.
- [66] Z. Švestka. Varieties of coronal mass ejections and their relation to flares. *Space Sci. Rev.*, 95:135–146, 2001.
- [67] R.A. Harrison. Soho observations relating to the association between flares and coronal mass ejections. *Adv. Space Res.*, 32:2425–2437, 2003.
- [68] D.V. Reames. Particle acceleration at the sun and in the heliosphere. *Space Sci. Rev.*, 90:413–491, 1999.
- [69] H. Kunow, G. Wibberenz, G. Green, and R. Müller-Mellin. Energetic particles in the inner solar system. In R. Schwenn and E. Marsch, editors, *Physics of the Inner Heliosphere, Vol. II: Particles, Waves and Turbulence*, volume 20 of *Physics and Chemistry in Space*, page 243. Springer, Berlin, Germany; New York, U.S.A., 1991.
- [70] D.V. Reames and C.K. Ng. Heavy-element abundances in solar energetic particle events. *Astrophys. J.*, 610:510–522, 2004.
- [71] M. Pearce *et al.* [The PAMELA Collaboration]. PAMELA: a Payload for Antimatter Matter Exploration and Light-nuclei Astrophysics status and first results. In *Proceedings of the IEEE Nuclear Science Symposium, Medical Imaging Conference, Honolulu, Hawaii, USA 27 Oct.-3 Nov. 2007*.
- [72] E.L. Chupp, D.J. Forrest, J.M. Ryan, J. Heslin, C. Reppin, K. Pinkau, G. Kanbach, E. Rieger, and G.H. Share. A direct observation of solar neutrons following the 0118 ut flare on 1980 June 21. *Astrophys. J. Lett.*, 263:L95–L99, 1982.

- [73] E.L. Chupp, H. Debrunner, E. Flueckiger, D.J. Forrest, F. Golliez, G. Kanbach, W.T. Vestrand, J. Cooper, and G. Share. Solar neutron emissivity during the large flare on 1982 June 3. *Astrophys. J.*, 318:913–925, 1987.
- [74] <http://neutronm.bartol.udel.edu/stations/mcmurdo.html>.
- [75] J. Alcaraz *et al.* [AMS Collaboration]. Erratum to: Leptons in Near Earth Orbit (Phys.Lett. B 484 (2000) 10-22). *Phys. Lett. B*, 495:440, 2000.
- [76] J. Alcaraz *et al.* [AMS Collaboration]. Protons in Near Earth Orbit. *Phys. Lett. B*, 472:215–226, 2000.
- [77] J. Alcaraz *et al.* [AMS Collaboration]. Cosmic Protons. *Phys. Lett. B*, 490:27–35, 2000.
- [78] J. Alcaraz *et al.* [AMS Collaboration]. Helium in Near Earth Orbit. *Phys. Lett. B*, 494:193–202, 2000.
- [79] J. Alcaraz *et al.* [AMS Collaboration]. Search for Antihelium in Cosmic Rays. *Phys. Lett. B*, 461:387–396, 1999.
- [80] S. Ahlen *et al.*. An AntiMatter Spectrometer in space. *Nucl. Instr. and Meth. A*, 350:351, 1994.
- [81] V. Choutko. Under Cutoff Proton Flux Measurement with AMS detector at STS91. *AMS Internal Note*, 2000-05-02b, 2000.
- [82] M. Cristinziani. Search for Heavy Antimatter and Energetic Photons in Cosmic Rays with the AMS-01 Detector in Space. *AMS Internal note 2002-03-02*, Ph.D. Thesis, Université de Genève 2002.
- [83] V. Choutko. AMS Trigger During Shuttle Flight. *AMS note 98_01a*, 1998.
- [84] U. Becker [AMS Collaboration]. AMS Report on the First Flight in Space June 2-12. In *Proceedings of the 29th International Conference on High Energy Physics (ICHEP '98), Vancouver, Canada, 23-29 July 1998*, volume 2, page 1458.
- [85] V. Innocente, M. Maire, and E. Nagy. GEANE: Average tracking and error propagation package. In **Amsterdam 1991, Proceedings, MC91: Detector and event simulation in high energy physics** 58-78. (see HIGH ENERGY PHYSICS INDEX 30 (1992) No. 3237).
- [86] R. Brun, F. Bruyant, M. Maire, A. C. McPherson, and P. Zancarini. GEANT3. CERN-DD/EE/84-1.
- [87] R. Fruhwirth. Application of Kalman filtering to track and vertex fitting. Wien Inst. Hochenergiephys. - HEPHY-PUB-87-503 (87,REC.JUN.) 19p.

- [88] V. Choutko [AMS Collaboration]. In *Proceedings of the 31st International Conference on High Energy Physics (ICHEP 2000), Osaka, Japan, 27 Jul - 2 Aug 2000*, volume 2, pages 1024–1027.
- [89] B. Bertucci [AMS Collaboration]. *Nucl. Phys. B (Proc. Suppl.)*, 100:124–126, 2001.
- [90] J. Berdugo and J. Casaus. Measurement of the Helium Cosmic Ray. Prepared for AMS Analysis Meeting, December 3, 1999.
- [91] V. Choutko. Over Cutoff Proton Flux Measurement with AMS detector at STS91. *AMS Internal Note*, 2000-05-02c, 2000.
- [92] G. D’Agostini. A Multidimensional unfolding method based on Bayes’ theorem. *Nucl. Instrum. Meth.*, A362:487–498, 1995.
- [93] J. Alcaraz. AMS Root User Guide. *AMS Internal Note*, 2005-07-01, 2005.
- [94] V. Choutko. AMS Proton Trigger Acceptance Study. *AMS Internal note*, 1999.
- [95] V. Choutko. Private communication.
- [96] V. Choutko and B. Bertucci. e^+ / e^- measurements with AMS at STS91. *AMS Internal note*, 2000.
- [97] H. Suter [AMS Collaboration]. AMS01 Experiment Online Monitoring. <http://ams.cern.ch/AMS/online.shtml>.
- [98] H. Suter [AMS Collaboration]. STS-91 Flight Parameters Histograms For AMS-01. <http://ams.cern.ch/AMS/Online/STS091/ShuttleHistos.shtml>.
- [99] H. Suter [AMS Collaboration]. Space Shuttle flight parameters for mission STS-91. *AMS Internal Note*, 1999.
- [100] E. Fiandrini *et al.*. Protons with kinetic energy $E > 70$ MeV trapped in the Earth’s radiation belts. *J. Geophys. Res.*, 109, 2004.
- [101] <http://spidr.ngdc.noaa.gov/spidr/index.jsp>.
- [102] E. L. Lehmann and H. J. M. D’Abrera. Nonparametrics: Statistical Methods Based on Ranks. *rev. ed. Englewood Cliffs, NJ: Prentice-Hall*, pages 292, 300, and 323, 1998.
- [103] S. A.; W. H.; Flannery, B. P.; Teukolsky and W. T. Vetterling. Numerical Recipes in FORTRAN: The Art of Scientific Computing. *2nd ed. Cambridge, England: Cambridge University Press*, pages 634–637, 1992.
- [104] R. Battiston A. Monfardini, P. Trampus and C. Gargiulo. AMICA, an astro-mapper for AMS. *Astroparticle Physics*, pages 355–360, 2006.

- [105] S. M. Harrison *et al.*. The cryogenic system of the superconducting magnet for the Alpha Magnetic Spectrometer. *AIP Conf. Proc.*, 823:1315–1322, 2006.
- [106] R. Battiston. A Silicon tracker for the antimatter spectrometer on the international space station Alpha. *Nucl. Phys. Proc. Suppl.*, 44:274–281, 1995.
- [107] W. Wallraff. 3-dimensional position control for the AMS-02 tracker with infrared laser beams. In *Proceedings of the 9th ICATPP Conference on Astroparticle, Particle, Space Physics, Detectors and Medical Physics Applications, Villa Erba, Como, Italy, 17-21 Oct 2005*.
- [108] Ph. Azzarello. Tests and production of the AMS-02 Silicon Tracker detectors. Ph.D. Thesis, Université de Genève 2004.
- [109] E. Cortina. The AMS-02 tracker performance. In *Proceedings of the 28th International Cosmic Ray Conferences (ICRC 2003), Tsukuba, Japan, 31 Jul - 7 Aug 2003*.
- [110] C.H. Lin, *et al.* [The AMS-02 Tracker Collaboration]. Charge determination of nuclei with the AMS-02 silicon tracker. *Nucl. Instrum. Meth.*, A540:121–130, 2005.
- [111] S. Natale. Performance of the AMS-02 experiment for High Energy Gamma Ray Astronomy. Ph.D. Thesis, Université de Genève 2007.
- [112] C. Sbarra. The scintillator counters of the TOF of the AMS-02 experiment. In *Proceedings of the International Workshop on Frontier Science: Physics and Astrophysics in Space, Frascati and Rome, Italy, 14-19 Jun 2004*.
- [113] T. Bruch and W. Wallraff. The Anti-Coincidence Counter shield of the AMS tracker. *Nuclear Instruments and Methods in Physics Research Section A: Accelerators, Spectrometers, Detectors and Associated Equipment*, 572:505–507, 2007.
- [114] T. Siedenburg. The AMS TRD: A gas detector designed for operation in space. *Nucl. Phys. Proc. Suppl.*, 150:30–33, 2006.
- [115] C. Adloff *et al.*. Performance of a 3D imaging electromagnetic calorimeter for the AMS02 space experiment. In *Proceedings of the 11th International Conference on Calorimetry in High-Energy Physics (Calor 2004), Perugia, Italy, 28 Mar - 2 Apr 2004*.
- [116] L. Arruda, F. Barao, P. Goncalves and R. Pereira. The Ring Imaging Cherenkov detector of the AMS experiment: Test beam results with a prototype. *Nucl. Phys. Proc. Suppl.*, 172:32–35, 2007.
- [117] P. Aguayo *et al.* Prototype study of the Cherenkov imager of the AMS experiment. *Nucl. Instrum. Meth.*, A560:291–302, 2006.

[118] <http://www.mssl.ucl.ac.uk/grid/egso/>.

[119] <http://lasco-www.nrl.navy.mil/>.

[120] <http://sohowww.nascom.nasa.gov/>.

[121] http://www.antarctica.ac.uk/bas_research/instruments/lpm.php.